

https://dspace.org/

A numerical study of thermoelectric properties of layered platinum chalcogenides and oxide

Mohammed, Hamza Adam Haroun

2020

https://hdl.handle.net/10539/31998

Downloaded from a DSpace repository. https://dspace.org/



A Numerical Study of Thermoelectric Properties of Layered Platinum Chalcogenides and Oxide

Hamza Adam Haroun Mohammed
1695895@students.wits.ac.za

Supervisor Professor Daniel P. Joubert
daniel.joubert2@wits.ac.za
Co-Supervisor Doctor G.M. Dongho-Nguimdo
moise@aims.ac.za

A thesis submitted to the Faculty of Science, in fulfilment of the requirements for the degree of Doctor of Philosophy.

Johannesburg, 2020

Declaration

I declare that the thesis hereby submitted to the University of Witwatersrand for the degree of Doctor of Philosophy has not previously been submitted by me for a degree at this or any other university, that is my own investigations, and that all material contained herein has been duly acknowledged.



Hamza Adam Haroun Mphammed, 16 March 2020

Abstract

The research reported in this thesis was motivated by the pressing need for novel materials for thermoelectric and photovoltaic applications. We numerically explored properties of Platinum dichalcogenides dioxide to examine if these compounds have potential as active components in thermoelectric and photovoltaic devices. Transition metal dichalcogenides (TMDs), in layered structures, have diverse properties that complement and potentially extend beyond promising properties of graphene, the prototypical layered material. Structural, stabilities (mechanical and dynamical), electronic, optical and thermoelectric properties of the bulk, bilayer and monolayer trigonal platinum dioxide and dichalcogenides PtX_2, (X = O, S, Se and Te) were investigated based on density functional theory (DFT) and many-body perturbation theory (MBPT) as implemented in the Vienna *ab-initio* simulation package. The structural properties of the bulk, bilayer and monolayer PtX_2 (such as optimized lattice parameters, cohesive and formation energies) were extracted from relaxed structures. Elastic coefficients and phonon dispersion studies showed that the relaxed structures are mechanically and dynamically stable. Investigation of the electronic band structure and densities of states of the bulk, bilayer and monolayer PtX_2 show that, at the DFT level of approximation, all the compounds are indirect band gap semiconductors apart from bulk PtO_2, PtS_2, $PtSe_2$ and $PtTe_2$ which are semi-metals.

To calculate optical properties, we implemented the Bethe-Salpeter equation (BSE) calculations on top of non-self-consistent G_0W_0 calculations to determine the dielectric matrix. The obtained results for absorbance in the visible light range for single layers in bulk, bilayer and a monolayer PtX_2, are from $0.9 - 35.27\%$ for in-plane absorbance. which is higher than 2.3% for graphene and $5-10\%$ for layered MoS_2, $MoSe_2$ and WS_2 of

similar thickness. The BSE optical gaps are in the range 0.37 to 2.75 eV for monolayer and bilayer PtX_2, while there is no gap bulk PtO_2, PtS_2, $PtSe_2$ and $PtTe_2$. Monolayer and bilayer PtX_2 may have potential for application in tandem solar cell applications.

Lattice and electronic transport coefficients were obtained within the relaxation-time approximation to the Boltzmann transport equations as implemented in PHONO3PY package and BoltzTraP2 packages. We calculated the lattice thermal conductivity for PtX_2 structures per layer, for ease of comparison between few layer and bulk systems. The obtained results are in range from 24.61×10^{-8} to 0.07×10^{-8} $Wm^{-1}K^{-1}$ at 300 K for bulk PtO_2 to monolayer $PtTe_2$, respectively. The out-of-plane coefficients of bilayer and monolayer are zero. The obtained values of the figure of merit (ZT) were in a range from 0.04 to 0.74, with the highest ZT values achieved by bilayer and monolayer PtO_2 (0.62 and 0.74), while the lowest ZT value was obtained by bulk PtS_2 of 0.04. Also, we observed the increase of figure of merit from bulk to monolayer which was expected due to their low lattice thermal conductivity. Most, the highest values of the calculated ZT were dominated by the electron charge carriers. The investigation suggests that of the compounds explored, n-type monolayer PtO_2 has the most promise for thermoelectric applications.

Publications

1. Hamza AH Mohammed, GM Dongho-Nguimdo and Daniel P Joubert. Structural stability, electronic, optical and lattice thermal conductivity properties of bulk and monolayer PtS_2. *Materials Today Communications*, 21:100661, 2019. Ref. [1].

2. Hamza AH Mohammed, GM Dongho-Nguimdo and Daniel P Joubert. Lattice thermal conductivity of bulk $PtTe_2$ and $PtSe_2$. In South African Institute of Physics 62nd Annual Conference (SAIP 2018), edited by Prof. Japie Engelbrecht (SU/2018), pp. 50 - 55. ISBN: 978-0-620-85406-1, Dec 2018. Available online at http://events.saip.org.za/getFile.py/access?resId=53&materialId=3&confId=100.

3. Hamza AH Mohammed, GM Dongho-Nguimdo and Daniel P Joubert. Structural stability and electronic properties of bulk, bilayer and monolayer PtX_2 (X = Se and Te). *Accepted for publication*

4. Comprehensive first-principles study of bulk and monolayer α-PtO_2 properties. *In preparation*

Presentations

1. Lattice thermal conductivity of bulk $PtTe_2$ and $PtSe_2$ poster presentation. 63^{rd} Annual Conference of the South African Institute of physics (SAIP2018), University of Free state, Bloemfontein, South Africa.

2. Structural stability and electronic properties of bulk, bilayer and monolayer PtX_2 (X = Se and Te) poster presentation. 64^{th} Annual Conference of the South African Institute of physics (SAIP2019), University of Venda, polokwane , South Africa.

DEDICATION

This thesis is dedicated to my beloved parents.

ACKNOWLEDGEMENTS

I would like to express my sincere gratitude specifically to my supervisors Prof. Daniel P. Joubert and G.M. Dongho-Nguimdo, for their support, guidance and close follow up throughout the course of this project. Their dedication, time and knowledge have been of great importance to the progress of the project. This acknowledgement will not be complete without acknowledging my fellow research group and postgraduate students at the School of Physics for their stimulating discussions during coffee breaks. I thanks my parents for their wholeheartedly support given to me through out the course of this study. I am eternally grateful for their unconditional love and support. This thesis was fully funded by Shendi University (ShU). Their support is gratefully acknowledged. The Centre for High Performance Computing (CHPC), Cape Town (South Africa) is acknowledged for providing computational resources.

Contents

Declaration i

Abstract ii

Publications iv

Presentations v

Dedication vi

Acknowledgements vii

List of Figures xvi

List of Tables xviii

1 Introduction 1

1.1 Motivation and Overview 1
1.2 Photovoltaic 2
1.3 Thermoelectric Phenomena 2
1.3.1 Thermoelectric effects 3
1.3.2 Thermoelectric figure of merit 4
1.3.3 Optimization of thermoelectric materials 4
1.4 Transition-metal dichalcogenides (TMDS) 5
1.5 Aims 8
1.6 Structure of this Thesis 8

2 Theoretical background **10**
2.1 Many-body Schrödinger equation . . . 10
2.2 Density Functional Theory . . . 11
2.2.1 The Hohenberg-Kohn Theorems . . . 11
2.2.2 Kohn-Sham equation . . . 12
2.2.3 The local density approximation . . . 12
2.2.4 Generalised gradient approximation . . . 13
2.2.5 Van der Waal's . . . 13
2.2.6 Periodic Boundary Conditions and Bloch's Theorem . . . 13
2.3 Many-body perturbation theory . . . 15
2.3.1 Green's function . . . 15
2.3.2 GW Approximation . . . 15
2.3.3 Bethe-Salpeter equation . . . 15
2.4 Boltzmann equation . . . 16
2.5 Transport theory . . . 16
2.5.1 Transport equation . . . 17
2.5.2 Seebeck coefficient and electrical conductivity . . . 17
2.5.3 Thermal conductivity (κ) . . . 18

3 Computational details **20**
3.1 DFT Calculations . . . 20
3.2 Structural Properties . . . 21
3.2.1 Lattice parameter . . . 21
3.2.2 Cohesive energy . . . 21
3.2.3 Formation energy . . . 21
3.3 Stabilities . . . 22
3.3.1 Mechanical stability . . . 22
3.3.2 Dynamical stability . . . 23
3.4 Electronic properties . . . 23
3.5 Optical coefficient . . . 24
3.6 Lattice thermal conductivity . . . 25
3.7 Transport phenomena . . . 26

4 Results and Discussions **27**
4.1 **Platinum dioxide (α-PtO_2)** . . . 28

4.1.1 Structural Properties . . . 28
4.1.2 Mechanical stability . . . 29
4.1.3 Dynamical Stability . . . 29
4.1.4 Electronic structure properties . . . 31
4.1.5 Optical properties . . . 33
4.1.6 Lattice thermal conductivity . . . 33
4.1.7 Transport properties of α-PtO_2 . . . 37
4.2 **Platinum disulfide (PtS_2)** . . . 40
4.2.1 Structural Properties . . . 40
4.2.2 Mechanical Stability . . . 41
4.2.3 Dynamical Stability . . . 42
4.2.4 Electronic structure properties . . . 42
4.2.5 Optical properties . . . 45
4.2.6 Lattice thermal conductivity . . . 47
4.2.7 Transport properties of PtS_2 . . . 51
4.3 **Platinum diselenide ($PtSe_2$)** . . . 54
4.3.1 Structural Properties . . . 54
4.3.2 Mechanical stability . . . 55
4.3.3 Dynamical stability . . . 55
4.3.4 Electronic structure properties . . . 57
4.3.5 Optical properties . . . 59
4.3.6 Lattice thermal conductivity . . . 59
4.3.7 Transport properties of $PtSe_2$ . . . 62
4.4 **Platinum ditelluride ($PtTe_2$)** . . . 66
4.4.1 Structural Properties . . . 66
4.4.2 Mechanical stability . . . 67
4.4.3 Dynamical stability . . . 67
4.4.4 Electronic structure properties . . . 69
4.4.5 Optical properties . . . 71
4.4.6 Lattice thermal conductivity . . . 71
4.4.7 Transport properties of $PtTe_2$ . . . 75

5 Summary and Conclusion **78**
5.1 Summary . . . 78
5.2 Conclusion . . . 80

References 81

List of Figures

1.1 Seebeck and Peltier effects. 4

1.2 Figure of the general form of layered TMDs (MX_2). The M and X are represented by brown and yellow colours. (a) top of MX_2 2D and (b) side of MX_2 2D 6

4.1 Crystal structure of bulk, bilayer and monolayer PtX_2. (a) the bulk structure unit cell, (b) the monolayer structure unit cell, (c) top view of monolayer and (d) side view of bilayer. The Pt atoms and X atoms are represented by grey and red ball, respectively. 27

4.2 The band structure of phonon dispersion for α-PtO_2. (a) Bulk (b) Bilayer (c) Monolayer. 30

4.3 Phonon total and partial density of states for α-PtO_2. (a) Bulk (b) Bilayer (c) Monolayer. 31

4.4 Calculated electronic structure of α-PtO_2. (a) Bulk (b) Bilayer (c) Monolayer. 32

4.5 Calculated total and partial DOS. (a) Bulk (b) Bilayer (c) Monolayer. . 32

4.6 (a) Imaginary part $\varepsilon_2(\omega)$, (b) real part $\varepsilon_1(\omega)$ of dielectric function and (c) absorbance for bulk, bilayer and monolayer of α-PtO_2. 34

4.7 Lattice thermal conductivity and heat capacity for bulk and monolayer α-PtO_2. (a) Lattice thermal conductivity against temperature, (b) cumulative lattice thermal conductivity against frequency. 35

4.8 Directional projected density of states, left is in-plane and right is out-of-plane for bulk, bilayer and monolayer α-PtO_2 as function of frequency. 36

4.9 Contribution ratio of phonon to lattice thermal conductivity, left is in-plane and right is out-of-plane for bulk and monolayer α-PtO_2 as function of frequency. (Recall there is no contribution in out-of-plane for monolayer). 36
4.10 Phonon lifetime at 300 K, (a) Bulk, (b) bilayer and (c) monolayer of α-PtO_2 as function of frequency. 36
4.11 Phonon average of directional group velocity, (a) Bulk, (b) bilayer and (c) monolayer of α-PtO_2 as function of frequency. 37
4.12 Seebeck coefficients of bulk, bilayer and monolayer α-PtO_2. 38
4.13 Electrical conductivity for a single layer in bulk, bilayer and monolayer α-PtO_2. 38
4.14 Electronic contribution to thermal conductivity for a single layer in bulk, bilayer and monolayer α-PtO_2. 39
4.15 Power factor for a single layer in bulk, bilayer and monolayer α-PtO_2. . 39
4.16 Figure of merit for bulk, bilayer and monolayer α-PtO_2. 40
4.17 The band structure of phonon dispersion for PtS_2. (a) Bulk (b) Bilayer (c) Monolayer. 43
4.18 TDOS and atomic contributions to acoustic and optical modes of phonon dispersion for PtS_2. (a) Bulk (b) Bilayer (c) Monolayer. 43
4.19 Bulk, bilayer and monolayer PtS_2 calculated electronic structure using optB86b-vdW for bulk and PBE for bilayer and monolayer. (a) Bulk, (b) bilayer and (c) monolayer. Along high symmetry directions. 46
4.20 Bulk, bilayer and monolayer PtS_2 calculated TDOS and PDOS for each atom and orbital using optB86-vdW for bulk and PBE for bilayer and monolayer. (a) Bulk, (b) bilayer and (c) monolayer. 46
4.21 GW_0 BSE results (a) imaginary part $\varepsilon_2(\omega)$, (b) real part $\varepsilon_1(\omega)$ of dielectric function and (c) absorbance for bulk, bilayer and monolayer of PtS_2. 47
4.22 Lattice thermal conductivity per layer, (a) lattice thermal conductivity against temperature, (b) cumulative lattice thermal conductivity against frequency. 48
4.23 Directional projected density of states, left is in-plane and right is out-of-plane for bulk, bilayer and monolayer PtS_2 as function of frequency. . 49

4.24 Contribution ratio of phonon to lattice thermal conductivity, left is in-plane and right is out-of-plane for bulk and monolayer PtS_2 as function of frequency. (Recall there is no contribution in out-of-plane for monolayer). 49
4.25 Phonon lifetime against frequency at 300 K. (a) Bulk, (b) bilayer and (c) monolayer. 50
4.26 Average directional phonon group velocities against frequency. (a) Bulk, (b) bilayer and (c) monolayer. 51
4.27 Seebeck coefficients of bulk, bilayer and monolayer PtS_2. 51
4.28 Electrical conductivity for a single layer in bulk, bilayer and monolayer PtS_2. 52
4.29 Electronic contribution to thermal conductivity coefficients for a single layer in bulk, bilayer and monolayer PtS_2. 52
4.30 Power factor for a single layer in bulk, bilayer and monolayer PtS_2. . . . 53
4.31 Figure of merit for bulk, bilayer and monolayer PtS_2. 53
4.32 The band structure of phonon dispersion for $PtSe_2$. (a) Bulk (b) Bilayer (c) Monolayer. 56
4.33 TDOS and atomic contributions to acoustic and optical modes of phonon dispersion for $PtSe_2$. (a) Bulk (b) Bilayer (c) Monolayer. 56
4.34 Bulk, bilayer and monolayer $PtSe_2$ calculated electronic structure using optB86b-vdW for bulk and PBE for bilayer and monolayer. (a) Bulk, (b) Bilayer (c) Monolayer. Along high symmetry directions. 57
4.35 Bulk, bilayer and monolayer $PtSe_2$ calculated TDOS and PDOS for each atom and orbital using optB86-vdW for bulk and PBE for bilayer and monolayer. (a) Bulk (b) Bilayer (c) Monolayer. 58
4.36 GW_0 BSE results (a) imaginary part $\varepsilon_2(\omega)$, (b) real part $\varepsilon_1(\omega)$ of dielectric function and (c) absorbance for bulk, bilayer and monolayer of $PtSe_2$. 58
4.37 Lattice thermal conductivity per layer for $PtSe_2$, (a) lattice thermal conductivity vs temperature, (b) cumulative lattice thermal conductivity vs frequency. 60
4.38 Directional projected density of states, left is in-plane and right is out-of-plane for bulk, bilayer and monolayer $PtSe_2$ as function of frequency. 61

4.39 Contribution ratio of phonon to lattice thermal conductivity, left is in-plane and right is out-of-plane for bulk and monolayer $PtSe_2$ as function of frequency. (Recall there is no contribution in out-of-plane for monolayer). 61
4.40 Phonon lifetime against frequency at 300 K for $PtSe_2$. (a) Bulk, (b) bilayer and (c) monolayer. 62
4.41 Average directional phonon group velocities against frequency for $PtSe_2$. (a) Bulk, (b) bilayer and (c) monolayer. 63
4.42 Seebeck coefficients of bulk, bilayer and monolayer $PtSe_2$. 63
4.43 Electrical conductivity for a single layer in bulk, bilayer and monolayer $PtSe_2$. 64
4.44 Electronic contribution to thermal conductivity for a single layer in bulk, bilayer and monolayer $PtSe_2$. 64
4.45 Power factor for a single layer in bulk, bilayer and monolayer $PtSe_2$. . . 65
4.46 Figure of merit for bulk, bilayer and monolayer $PtSe_2$. 65
4.47 The band structure of phonon dispersion for $PtTe_2$. (a) Bulk (b) Bilayer (c) Monolayer. 68
4.48 TDOS and atomic contributions to acoustic and optical modes of phonon dispersion for $PtTe_2$. (a) Bulk (b) Bilayer (c) Monolayer. 68
4.49 Calculated band structure of $PtTe_2$. (a) Bulk (b) Bilayer (c) Monolayer. 69
4.50 Calculated total and partial DOS of $PtTe_2$. (a) Bulk (b) Bilayer (c) Monolayer. 70
4.51 GW_0 BSE results (a) imaginary part $\varepsilon_2(\omega)$, (b) real part $\varepsilon_1(\omega)$ of dielectric function and (c) absorbance for bulk, bilayer and monolayer of $PtTe_2$. 70
4.52 Lattice thermal conductivity per layer for $PtTe_2$, (a) lattice thermal conductivity against temperature, (b) cumulative lattice thermal conductivity against frequency. 72
4.53 Directional projected density of states, left is in-plane and right is out-of-plane for bulk, bilayer and monolayer $PtTe_2$ as function of frequency. 73
4.54 Contribution ratio of phonon to lattice thermal conductivity, left is in-plane and right is out-of-plane for bulk and monolayer $PtTe_2$ as function of frequency. (Recall there is no contribution in out-of-plane for monolayer). 73
4.55 Phonon lifetime against frequency at 300 K for $PtTe_2$. (a) Bulk, (b) bilayer and (c) monolayer. 74

4.56 Average directional phonon group velocities against frequency for $PtTe_2$. (a) Bulk, (b) bilayer and (c) monolayer. 74
4.57 Seebeck coefficients of bulk, bilayer and monolayer $PtTe_2$. 75
4.58 Electrical conductivity for a single layer in bulk, bilayer and monolayer $PtTe_2$. 76
4.59 Electronic contribution to thermal conductivity for a single layer in bulk, bilayer and monolayer $PtTe_2$. 76
4.60 Power factor for a single layer in bulk, bilayer and monolayer $PtTe_2$. . . 77
4.61 Figure of merit for bulk, bilayer and monolayer $PtTe_2$. 77

List of Tables

4.1 Calculated, experimental and theoretical optimized lattice constants of bulk, bilayer and monolayer α-PtO_2, cohesive (E_{coh}) and formation formation energies per atom, and inter-layer distance. 28

4.2 Elastic constants (C_{ij} (GPa)) for bulk, bilayer and monolayer α-PtO_2. . 29

4.3 The obtained Bulk moduli (B) Shear moduli (G),Young's moduli (Y) and Poisson's ratio (ν) in GPa, for bulk, bilayer and monolayer. 29

4.4 The calculated band gaps compared to the experimental and theoretical (in eV) of α-PtO_2. 31

4.5 Calculated, experimental and theoretical optimized lattice constants of bulk bilayer and monolayer PtS_2, cohesive (E_{coh}) and formation formation energies per atom, and inter-layer distance. 41

4.6 Elastic constants (C_{ij} (GPa)), for bulk, bilayer and monolayer PtS_2. . . 41

4.7 The obtained Bulk moduli (B) Shear moduli (G),Young's moduli (Y) and Poisson's ratio (ν) in GPa, for bulk, bilayer and monolayer, and the other theoretical study. 42

4.8 The calculated band gaps values compared to the experimental and theoretical (in eV) of PtS_2. 44

4.9 Calculated, experimental and theoretical, optimized lattice constants of bulk, bilayer and monolayer $PtSe_2$, cohesive (E_{coh}) and formation formation energies per atom, and inter-layer distance. 54

4.10 Elastic constants (C_{ij} (GPa)), for bulk, bilayer and monolayer $PtSe_2$. . . 55

4.11 The obtained Bulk moduli (B) Shear moduli (G),Young's moduli (Y) and Poisson's ratio (ν) in GPa, for bulk, bilayer and monolayer $PtSe_2$, and the other theoretical study. 55

4.12 The calculated band gaps values compared to the experimental and theoretical (in eV) of $PtSe_2$. 58
4.13 Calculated, experimental and theoretical optimized lattice constants of bulk bilayer and monolayer $PtTe_2$, cohesive (E_{coh}) and formation formation energies per atom, and inter-layer distance. 66
4.14 Elastic constants (C_{ij} (GPa)), for bulk, bilayer and monolayer $PtTe_2$. . 67
4.15 The obtained Bulk moduli (B) Shear moduli (G),Young's moduli (Y) and Poisson's ratio (ν) in GPa, for bulk, bilayer and monolayer, and the other theoretical study. 67
4.16 The calculated band gaps values compared to the experimental and theoretical (in eV) of $PtTe_2$. 70

5.1 Our calculated, DFT and BSE-optical gap (in-plane (in) and out-of-plane (out)) band gaps (in eV) for the bulk, bilayer and monolayer of PtX_2. . 78
5.2 The calculated maximum absorbance of in-plane, in the visible photon energy range for bulk, and a single layer of bilayer and monolayer PtX_2. 79
5.3 Lattice thermal conductivity (in $Wm^{-1}K^{-1}$) for a single PtX_2 layer. . . 79
5.4 The in-plane highest figure of merit (ZT) at a various temperature regimes of bulk, bilayer and monolayer PtX_2. 80

1

Introduction

1.1 Motivation and Overview

The necessity for alternative and renewable energy technologies to decrease our dependence on fossil fuels has lead to different directions of research, including high-temperature energy harvesting via the direct recovery of waste heat and its conversion into useful electrical energy using thermoelectric devices. During the past few decades research on thermoelectric materials has been intensified. Such interest has been driven by the need for more efficient use of energy and a need for thermoelectric materials that can be used for converting heat into electricity and electronic refrigeration [2, 3]. The investigation of a different system of potential thermoelectric materials has been studied by various research groups. Dresselhaus M S *et al.*, are investigate the thermoelectric properties of some low-dimensional materials, and they found their figure of merit are in range from ∼0.08 to ∼0.75 at temperature range from 300 to 1400 K [4]. The figure of merit for the some selected materials were in range from ∼0.95 at 400 K for Bi_2Te_3 up to 1.7 at 800 K for ZN_4Sb_3 [5]. Nanostructuring approach are used to study the enhancement of thermoelectric figure of merit of bulk materials, their obtained were in range from 0.25 to 1.4 at temperature range from 0 to 1000 K [6]. The main two research efforts are focused on the materials are maximization of the power factor PF and minimization of the thermal conductivity, (especially lattice thermal conductivity). The proposed application of thermoelectric materials increased the activity in this field by optimizing greater performance and higher temperature thermoelectric materials

compared with the current materials. Recently, the thermoelectric solar hybrid system has been investigated to improve absorption in the infrared zone in the solar spectrum and for thermoelectric solar power generation [7]. Nowadays, of more importance is the higher performance development of thermoelectric materials. Novel applications of thermoelectrics such as enhanced performance of optoelectronics coupled with solid-state thermoelectric cooling, power provision for deep-space probes via radioisotope thermoelectric generators and biothermal batteries to power heart pacemakers. Recently, thermoelectric generators have been installed in automobiles to capture waste heat from the exhaust system and to transform it into useful electrical energy for automotive electrical systems and for increased fuel efficiency for use in the next-generation vehicles [8]. Thermoelectric refrigeration is an environmentally green method of small-scale such as infrared detectors, optoelectronics and localized cooling in computers, and many other applications [9].

1.2 Photovoltaic

Photovoltaic technology is one of the ways to generate electricity from the sun energy [10]. In a semiconductor, the PN-junction is incorporated of practically for all photovoltaic devices to develop the photovoltage. The solar cell system operation is based on photovoltaic effects, reported by Becquerel in 1839 [10, 11]. To produce direct voltage and current, the PV cell should be connected in series, and this direct voltage can be converted to alternative current power, when required. Many publications have described its operating principles [12, 13]. However, the efficiency depends on the energy absorbed which also depends on the band gap, taking into account the nature of transition as a direct and an indirect band gap [14].

1.3 Thermoelectric Phenomena

One of the most right challenges of our time is to find renewable alternative energy sources which are environmentally friendly. The technology of thermoelectric is considered a kind of energy conversion technology. The description of the conversion of thermal energy to electrical energy, or vice-versa is a phenomenon that is called the thermoelectric effect [15]. There are three important transport effects, namely the See-

beck effect, the Peltier effect and the Thomson effect. Details about those effects are summarised in section (1.3.1). Thermoelectric performance of materials determine the energy efficiency of thermoelectric devices. The figure of merit (ZT) is a quantity used as a gauge for novel thermoelectric materials. Bismuth telluride-based alloys have long be considered as the best thermometric materials because of their high ZT, which is slightly above unity. Through the last decade, the search for promising bulk thermoelectric materials has intensified. Nowadays, new material systems are being developed to achieve ZT well above unity. This also forms the aims of our study.

1.3.1 Thermoelectric effects

There are three important thermoelectric effects are namely, Seebeck, Peltier and Thomson effect. The Seebeck effect describes the voltage gradient in a conductor subjected to a gradient of temperature. Which was discovered by Seebeck, when a compass needle deflected when placed in the vicinity of a closed-loop formed of two dissimilar metals with a temperature difference between the junctions. This observation provides direct evidence that a current flows through the closed circuit driven by the temperature difference. On the other hand, the Peltier effect describes the conversion of electrical current into heat transfer, which is a reverse technique of the Seebeck [15]. The Peltier effect is the underlying foundation for thermoelectric refrigeration. When an electric current passes through two dissimilar materials such as metals or semiconductors that are connected at two junctions, heat will be absorbed in one junction and liberated at the other junction. As a result, one junction cools off while the other heats up, depending on the direction of the current [16]. Figure 1.1 show Seebeck and Peltier effects. The Thomson effect is the rate of heat absorbed or emitted when a conductor is subjected to a temperature difference along its length. There is tow type of Thomson effect the positive and negative effect, that depends on the direction of the current movement, from the high to a low potential or vice versa [17]. In this research, we focused on how heat energy is converted to the electricity, which depends on charge carriers moving through a gradient of temperature, which is called the Seebeck effect.

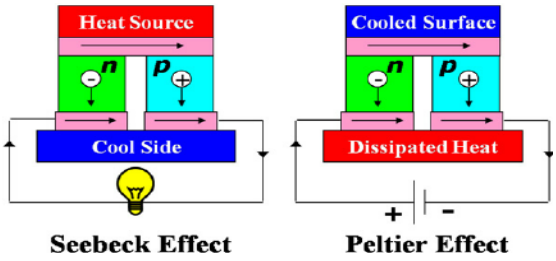


Figure 1.1: Seebeck and Peltier effects.

1.3.2 Thermoelectric figure of merit

The figure of merit concept is used to describe the efficiency of a thermoelectric material. It is expressed as;

$$ZT = \frac{S^2\sigma T}{\kappa} = \frac{S^2\sigma T}{\kappa_e + \kappa_L}, \tag{1.3.1}$$

where S, σ, T and κ are the Seebeck coefficient, electrical conductivity, temperature in Kelvin scale and thermal conductivity, respectively. κ_e and κ_L are electronic and phononic contributions, which is a combination of κ ($\kappa = \kappa_e + \kappa_L$). The stander way to figure out good thermoelectric material is to determine the figure of merit. Thus, the efficiency of energy conversion has a direct relation to the figure of merit [18]. Hence, a good thermometric material should have a large Seebeck coefficient for increasing the conversion of heat to electricity, a high electrical conductivity to reduce the Joule effect and a low thermal conductivity to make a large gradient of temperature [15].

1.3.3 Optimization of thermoelectric materials

Good thermoelectric materials should have a low thermal conductivity and a large power factor. Usually, semiconductors have a large (S) and low (σ), compared to metals. Doping a material might increase its electrical conductivity. But at the same time, the heavy doping can reduce the Seebeck coefficient due to shifting of the Fermi level close to band edge or into the band. Then, it is necessary to find a doping level where the power factor is optimized. There are many ways to reduce the thermal conductivity, for example, adding a short-range disorder into the crystal structure, or substitution by isoelectronic elements, which may affect the electrical conductivity. Unfortunately, to increase the figure of merit through reducing thermal conductivity is considered as a

main challenge [19, 20].

1.4 Transition-metal dichalcogenides (TMDS)

The word chalcogen comes from the Greek word "chalcos" which is means ore or metal and "genes" which means formation, so ore former is considered the general mean of the term chalcogen [21]. The chalcogenide elements belong to group sixteen of the periodic table. This group consists of oxygen, sulphur, selenium, tellurium and polonium, however, oxygen is usually excluded from this group because it has different chemical behavior compare to others. For example, the wide contribution of band gaps to various electrical and optical properties. The chalcogenide compounds were discovered recently compared to oxygen compound, nevertheless, it is not considered from the chalcogenide compounds. The minerals pyrite (FeS_2) and calaverite ($AuTe_2$) are the most common form chalcogenide compounds. Generally, chalcogenides can exist over a wide range of compounds, like glass-forming [22]. Transition metal dichalcogenides and dioxide have a general form of MX_2, where M represents the transition metal and X an atom of the oxygen family (X = O, S, Se and Te). Some TMDs are layered compounds in a sandwiched form (X-M-X), held together by covalent bonds, as shown in Figure 1.2.

The van der Waals forces are stacking the layers together. This phenomenon of bonding is helpful to create the two dimensional structure [23, 24, 25, 26]. However, these compounds have two important differences from the iso-structural group IVb, Vb and VIb TMDs. First, a large number of electrons in d-shell in the group VIIIc metal compounds compared with other groups of metal. The small value of the ratio c/a is considered second difference when it compares to the ideal value of 1.633 [27]. The group VIIIc layered TMDs have electronic structure and related behavior quite different from the other groups of those the TMDs. Previous calculations on the group VIIIc were done on $PdTe_2$ compound, using both the KKR (Korringa-Kohn-Rostoker) and LMTO (linear muffin-tin orbital) methods. Substituting chalcogen atoms, from S to Te shows the variation on the electronic structure [26]. Most works have been focused on group VI TMDs, MoS_2 and WS_2, while other groups remain in uncharted waters [28]. Their electronic structure properties studies have been reported and discussed for group X TMDs [29, 30], which differentiates them from others.

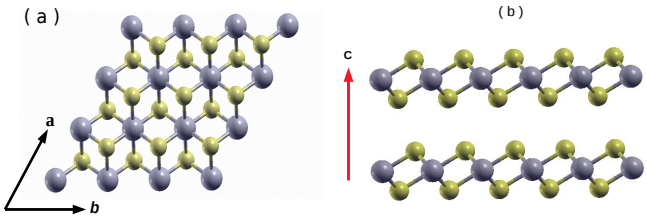


Figure 1.2: Figure of the general form of layered TMDs (MX_2). The M and X are represented by brown and yellow colours. (a) top of MX_2 2D and (b) side of MX_2 2D

Platinum dioxide (PtO_2)

Platinum dioxide is a trigonal phase layered structure with space group $P\bar{3}m1$ (No. 164). Stability of α-PtO_2 phase were examined using surface x-ray diffraction (SXRD), the experiments observed that α-PtO_2 is fully stable [31, 32]. X-ray was used to measure lattice parameters of PtO_2 and other phases, α-PtO_2 has hexagonal structure a CdI_2-like structure with lattice parameters $a_0 = 3.11$ Å, $c_0 \sim 4.34$ Å and $V_0 = 36.44$ Å^3 [33]. The photoelectron spectroscopic shows that its optical gap ranges from 1.30 to 1.47 eV [34], while optical reflectance measurement gives optical gap of ∼1.2 eV [35]. Zhensheng *et al.* investigated the electronic properties of α-PtO_2, and they reported that is a semiconductor with optical gap of 1.84 eV [36]. Metal oxide has a wide range of applications in optical devices, catalysis, photo-sensors and electronics [37].

Platinum disulfide (PtS_2)

Bulk, bilayer and monolayer PtS_2 crystallise in a CdI_2 structure, with space group $P\bar{3}m1$ (No. 164) [26]. The lattice parameters $a_0 = 3.54$ Å, $c_0 = 5.04$ Å and $V_0 = 54.78$ Å^3 for bulk structure were investigated using x-ray diffraction [30, 38, 39]. The structural, electronic and optical properties of monolayer PtS_2 have also been well investigated [40, 41, 42]. They are predicted to have promising photocatalytic properties [25], but their thermoelectric properties are yet to be well understood. Previous spectroscopic studies at 300 K show that bulk PtS_2 is a semiconductor with an indirect band gap of 0.95 and 0.87 eV parallel and perpendicular to the trilayers, respectively [43, 44]. Electronic structure calculations of infinite periodic bulk PtS_2 confirmed that bulk and monolayer PtS_2 are indirect band gap semiconductors [40, 41, 42].

Platinum diselenide ($PtSe_2$)

Platinum diselenide also has a trigonal phase structure, with space group $P\bar{3}m1$ (No. 164). X-ray measurements showed that $PtSe_2$ possess crystallises in a CdI_2 like-structure and the lattice parameters are $a_0 = 3.73$ Å, $c_0 = 5.08$ Å and $V_0 = 61.15$ Å^3 [45]. Experiments showed that bulk $PtSe_2$ has a metallic behaviour at a temperature from 5 to 380 K with a high residual resistance ratio of 184 [46]. It also has a semi-metal character [26], while monolayer and bilayer structures are semiconductors with a band gaps of 1.2 eV and 0.21 eV, respectively [47]. Phonon dispersion and electronic properties of bulk, monolayer, and bilayer $PtSe_2$, were investigated using DFT with the Tkatchenko and Scheffler van der Waal's correction (DFT-TS) [48]. This study confirm that the bulk is semi-metallic while monolayer and bilayer configurations are semiconductors with an indirect band gap of ∼1.6 eV and ∼0.8 eV, respectively. Yim C. *et al* [49] demonstrated that multilayer $PtSe_2$ is easy to synthesise and showed that vertically stacked heterostructures of $PtSe_2$ on Si can be used as photodiodes and in photovoltaic cells. The electronic structure of monolayer and bilayer $PtSe_2$ have been calculated using the Perdew-Burke-Ernzerhof (PBE) exchange-correlation approximation with band gaps of 1.39 and 0.99 eV for $PtSe_2$, respectively [50]. The calculated lattice thermal conductivity of monolayer $PtSe_2$ with a vacuum of 20.12Å, was found to be 16.97 $Wm^{-1}K^{-1}$ at 300 K [51]. The investigation of electronic and transport properties for monolayer $PtSe_2$ reported in reference [52], suggests that this compound has promising properties for thermoelectric applications.

Platinum ditelluride ($PtTe_2$)

Platinum ditelluride is a third compound of the PtX_2 family, with trigonal phase structure and space group $P\bar{3}m1$ (No. 164). The lattice constant of bulk $PtTe_2$ are $a_0 = 4.01$ Å, $c_0 = 5.20$ Å and $V_0 = 72.43$ Å^3 was obtained experimentally using x-ray [39]. As in the case of $PtSe_2$, bulk $PtTe_2$ has a metallic behaviour at a temperature from 5 to 380 K with a high residual resistance ratio of 29 [46]. Recently, the bulk $PtTe_2$ has been reported to be a type-II Dirac semi-metal [53]. Mechanical, electronic and optical properties were calculated for a monolyaer $PtTe_2$ using DFT, and they found a monolyaer $PtTe_2$ is a semiconductor with in direct band gap of 0.70 eV [41]. Zhishuo H *et al.* reported that a monolayer $PtTe_2$ is dynamically stable, and it is a semiconductor with an indirect band gap of 0.61 eV [42]. Biaxial strain effects on electronic

structures and thermoelectric properties in monolayer $PtTe_2$ have been investigated. The lattice thermal conductivity of monolayer $PtTe_2$ was found to be 7.89 $Wm^{-1}K^{-1}$ at 300 K [52]. Also, the electronic and transport properties for monolayer $PtTe_2$ have been studied and reported in reference [52], and the obtained results suggest that it is promising for thermoelectric applications. The spin-orbit coupling has been shown to have an important effect on electronic structures and power factors for semiconducting TMD monolayers [54, 51, 55].

1.5 Aims

The aims and the specific objectives of this thesis are:

- To investigate physical properties of the layered structure of trigonal phase platinum dioxide and dichalcogenides, (PtX_2; (X = O, S, Se and Te)).
- To investigate the structural and electronic properties.
- To examine the mechanical and dynamical stabilities, the elastic constants and phonon band structure through the computational approaches.
- To investigate the optical properties of most stable phases.
- To calculate the lattice thermal conductivities of the structure, the single-mode relaxation-time approximation.
- A comparison between the bulk, bilayer and monolayer, for PtX_2; (X = O, S, Se and Te), in order to know the best one for thermoelectric applications.
- Transport properties will then be evaluated by solving Boltzmann transport equations to obtain the figure of merit, Seebeck coefficient, charge carrier concentration, lifetime, thermal and electrical conductivity as well as power factor. This will help to identify the PtX_2 phases which are potential candidates for thermoelectric applications.

1.6 Structure of this Thesis

This thesis has been arranged in the following manner: In Chapter 1, we introduce a motivation for this research as well as briefly discuss on the platinum oxide and

chalcogenides. The background of density functional theory, many-body perturbation theory and Boltzmann transport theory are presented in Chapter 2. in Chapter 3, we give details of the computational methods. Chapter 4 is dedicated to our calculated results and discussions. In this section, structural, mechanical, dynamical, electronic, optical and thermoelectric properties of each compound in studied in separated section. In section 4.1 we study the the properties for α-PtO_2. Section 4.2 is devoted to the properties for PtS_2. Section 4.3 is devoted to the properties for $PtSe_2$. The properties for $PtTe_2$ are investigated in section 4.4. Finally, Chapter 5 summarises the main results, concludes the study.

2

Theoretical background

2.1 Many-body Schrödinger equation

In this section, we discussed the many-body systems and Born Oppenheimer approximation. The many-body systems are very complex, to study the physical and chemical properties of materials, since this material have a large number of interacting particles, so, we must then consider it as many-body problems. An *ab-initio* method was used to solve the Schrödinger equation for many-body problems. The Schrödinger equation can be expressed in the form:

$$\hat{H}|\psi\rangle = E|\psi\rangle, \tag{2.1.1}$$

where $|\psi\rangle$ is the wave function, E is the eigenvalue of energy and $\hat{H}$ is the Hamiltonian operator, which can be in form:

$$\begin{aligned}\hat{H} = -\frac{\hbar^2}{2m_e}\sum_{i=1}^{N}\nabla_i^2 - \sum_{j\neq j}^{N}\frac{Z_I e^2}{|\mathbf{r}_i - \mathbf{R}_I|} + \sum_{j\neq i}^{N}\frac{e^2}{|\mathbf{r}_i - \mathbf{r}_j|} \\ -\frac{\hbar^2}{2M_I}\sum_{I=1}^{N}\nabla_I^2 - \sum_{J\neq I}^{N}\frac{Z_I Z_J e^2}{|\mathbf{R}_I - \mathbf{R}_J|},\end{aligned} \tag{2.1.2}$$

where m_e, M_I and N represent the electrons mass, nuclei mass, electrons and nuclei number, respectively, while R_I, $r_{i,j}$ and Z represent the nuclei position number i^{th}, electron position number i^{th} or j^{th} and nuclei charge, respectively. $\hbar$ and e are the con-

ventional fundamental constants. We can rewrite the Hamiltonian operator as follows;

$$\hat{H} = \hat{T}_n + \hat{V}_{nn} + \hat{T}_e + \hat{V}_{en} + \hat{V}_{ee}, \tag{2.1.3}$$

whereby, T_n and V_{nn} are the kinetic energy and the potential energy of the nuclei, respectively, T_e and V_{ee} are the kinetic energy and potential energy of the electrons, respectively and V_{ne} stands for the nuclei-electron interaction.

The Born-Oppenheimer approximation suggests that to treat the movement the movement of electrons and nuclei independently because the latter has a heavy mass compared to that of electron [56]. The born-Oppenheimer approximation can be illustrated in the form of an equation as;

$$\psi(\mathbf{R}_j, \mathbf{r}_i) = \psi_e(\mathbf{R}_j, \mathbf{r}_i)\psi_n(\mathbf{R}_j), \tag{2.1.4}$$

where $\psi_e(\mathbf{R}_j, \mathbf{r}_i)$ is the electron wave-function and $\psi_n(\mathbf{R}_j)$ is the nucleus wave-function.

2.2 Density Functional Theory

This section is focused on density functional theory description, (Hohenberg-Kohn Theorems a Kohn-Sham equation) and some approximations which have been used in this thesis. We will also talk of periodic boundary and Bloch's theorem, k-points, Brillouin zone and pseudopotentials. To simplify the original problem of many-body-system, the movement of the electrons and ionic must be treated separately and hence allows us to treat the ions in a classical formalism. Density functional theory, based on two theorems first proved by Hohenberg and Kohn [57, 58] in the 1960s, makes it possible to describe the ground-state properties of a real system in terms of its ground state charge density instead of the far more complicated wave function. This theory allows us to find the ground-state properties of a system in terms of the ground state charge density without explicit recourse to many-particle wave functions.

2.2.1 The Hohenberg-Kohn Theorems

Theorem I: Interacting particles system in an external potential $V(\mathbf{r})$, this external potential is unique, for the ground state electronic charge density.

Theorem II: A universal functional for the energy in terms of the density can be defined, valid for any external potential $V_{ext}(\mathbf{r})$. For any particular $V_{ext}(\mathbf{r})$, the exact ground state energy of the system is the global minimum value of this functional, and the density $\rho(\mathbf{r})$ that minimizes the functional is the exact ground state density $\rho_0(\mathbf{r})$. The first and second theorems have been proved in many articles. [59, 60, 57, 61, 62, 63].

2.2.2 Kohn-Sham equation

Kohn and Sham assumed a practical ansatz based on non-interacting electron system, the interacting electrons system can be represented by the auxiliary ground state density system, the auxiliary Hamiltonian usually has the main term of kinetic energy operator and effective potential V_{eff} [58, 59, 60]. Where the ground state density is given by;

$$\rho[\mathbf{r}] = 2\sum_i |\psi_i(\mathbf{r})|^2, \tag{2.2.1}$$

and the Hamiltonian formula is expressed as;

$$\hat{H} = \Big(-\frac{\hbar^2}{2m_e}\nabla^2 + V_{KS}(\mathbf{r})\Big)\psi_i = \varepsilon_i\psi_i, \tag{2.2.2}$$

where V_{KS} is the Kohn-Sham potential operator which is consist of three components as;

$$V_{KS} = V_{ext} + V_H + V_{xc}, \tag{2.2.3}$$

where V_{ext} is the external, V_H is the Hartree and V_{xc} is the exchange-correlation potentials.

2.2.3 The local density approximation

The basis of all the approximations of the exchange-correlation is the local density approximation (LDA). In the LDA, the inhomogeneous electronic system is treated as a homogeneous electron gas with uniform density. The exchange-correlation potential is dependant on the exchange-correlation energy from the electronic density, this is the

local density approximation (LDA) [61] :

$$E_{xc}[\rho] = \int \rho(\mathbf{r})\varepsilon_{xc}(\rho(\mathbf{r}))d\mathbf{r}, \tag{2.2.4}$$

where $\varepsilon_{xc}(\rho(\mathbf{r}))$ is the exchange-correlation energy density.

2.2.4 Generalised gradient approximation

Hohenberg and Kohn proposed the gradient expansion approximation (GEA) [62, 63, 60, 64] because the LDA does not works for real systems. Notwithstanding, the disappointing results, the GEA provided the basis for the generalised gradient approximation (GGA) which is currently the most popular exchange-correlation functional [61, 65] defined as;

$$E_{xc}^{GGA}[\rho] = \int \rho(\mathbf{r})\varepsilon_{xc}(\rho(\mathbf{r})), \nabla\rho(\mathbf{r})d^3\mathbf{r}. \tag{2.2.5}$$

The GGA is considering inhomogeneity for electron density gradient. However, GGA results in almost underestimation, for example, the lattice constant and band gap results, compared to LDA results. GGA has many different types, but in this research the Perdew-Burke-Ernzerhof (PBE) [66, 67] exchange-correlation functional,

2.2.5 Van der Waal's

The LDA and GGA are among stander exchange correlation functionals in DFT, to describe the structural parameters, electronic structure and other properties. However, fail to account for long-range electron correlations that are the primary cause of van der Waals interactions, resulting from dynamical correlations between fluctuating charge distributions, which play a significant role in layered structures [68]. The optimized Becker 86b van der Waals (optB86b-vdW) [69] is consider a attempt to improve approximate functionals to account for van der Waals effects.

2.2.6 Periodic Boundary Conditions and Bloch's Theorem

Since the crystal solid is periodic in three dimensions (3D) and the calculations problem of that is a large number of electrons; the periodic boundary conditions (PBC) can re-

duce the system size to just one particular unit cell taking the symmetry into account. For a layered crystal (monolayers and surfaces), which have periodicity in two dimensions, it can be represented as slabs, with a vacuum region. To prevent the interaction between the layer, the vacuum region must be enough large to ensure the layers are decoupled.

The periodic boundary conditions in Blochs theorem [70, 71, 72], was described using the wave function in Bloch's theorem can be expressed as:

$$\psi_{\mathbf{k}}(\mathbf{r}) = e^{i\mathbf{k}.\mathbf{r}} u_{\mathbf{k}}(\mathbf{r}), \tag{2.2.6}$$

where $\psi_{\mathbf{k}}(\mathbf{r})$ is the electronic wave function, $\mathbf{r}$ is a position vector, $\mathbf{k}$ is a wave vector, in the right side of the above expression, is the plane wave $e^{ik.\mathbf{r}}$ and the periodic function $u_k(\mathbf{r})$.

K-points and Brillouin zone

Three independent lattice vectors are required to define the reciprocal lattice vectors of the cell. The Wigner-Seitz size cell of the reciprocal lattice is represented as a first Brillouin zone. The volume (Ω_{BZ}) is defined as [73];

$$\Omega_{BZ} = \mathbf{b}_i.\mathbf{b}_j \times \mathbf{b}_k = \frac{(2\pi)^2}{\Omega}, \tag{2.2.7}$$

where Ω is the unit cell volume. Note that the accurate method to sample the Brillouin zone has been devised by Monkhorst-Pack [74] and Chadi and Cohen [75].

Pseudopotentials

The physical properties of the materials depends more on valence than core electrons. The advantage of pseudopotential is substituting the core electrons and strong ionic potential by a weaker pseudopotential [76, 73, 61]. The pseudopotential represents a set of pseudo wave functions in place of the true valence wave function [73, 77]. There are many types of pseudopotentials one can construct from first-principles such as ultrasoft pseudopotentials [78], the potentials based on the projector augmented wave (PAW) method [79] and norm-conserving pseudopotentials [80].

2.3 Many-body perturbation theory

The Green function, GW Approximation and Bethe-Salpeter equation were covered briefly. The many-body perturbation theory (MBPT) is based on quasi-particle and Green function concepts. It is best method to accurately describe the exited states properties than DFT [60, 64].

2.3.1 Green's function

The Green function can be used to extract physical informations in many-body theory [81]. The energy, lifetime and expectation values of single-particle operators are the quasi-particle properties, which are obtained from the Green function [82].

2.3.2 GW Approximation

The solution of many-body system can be used to obtain the self-energy of two particles Green's function [83], but this is not practicable. Hedin [84] proposed GW Approximation to obtain the self-energy which is practicable method given by;

$$\sum_{GW}(\mathbf{r},\mathbf{r}';t) \simeq iG(\mathbf{r},\mathbf{r}';t)W(\mathbf{r},\mathbf{r}';t), \tag{2.3.1}$$

where $G(\mathbf{r},\mathbf{r}';t)$ is the interacting Green function and $W(\mathbf{r},\mathbf{r}';t)$ is the dynamically screened coulomb. $\mathbf{r}$, $\mathbf{r}'$ and t are the conventional fundamental constants.

2.3.3 Bethe-Salpeter equation

The description of excitation state requires propagation of two particles (electron-hole pair) which is beyond the one-particle Green function GW approach. GW approach required the improvement in the response functions to account for two-particle Green function. The electron-hole pairs interaction can now be included by adding the vertex correction in vertex function which is beyond the RPA. This is done by including the vertex function Γ into polarizability function equation P through the second iteration and solve for polarizability ${}^3P$, four-point screened-interaction function ${}^4W$(1,2,3,4) and four-point Kernal function K(1,2,3,4) [85, 86]. In practice to perform BSE calculations requires one first to determine the static screened electron-hole interaction term

W(x,x′;ω=0) and the quasiparticle band structure, typically from a GWA calculation [87, 86]. With this the effective two-particle Hamiltanion H^{2P} is built, H^{2P} is diagonalized to derive the expression of macroscopic dielectric function $\epsilon_M(\omega)$ directly related to measurable quantities. If one considers the positive resonance part of H^{2P} the resultant operator is Hermitian and its eigenstate orthogonal [85, 86]. H^{2P} contributes to the bare Coulomb interaction called the electron-hole exchange and contribution due to the screen electron-hole W is responsible for the appearance of bound states, and it can even lead to hydrogen like spectral features in insulators [85].

2.4 Boltzmann equation

The Boltzmann equation provides description of electrons motion, which changes their position and momentum when subjected to diffusion. The linearised Boltzmann equation is given by [88, 89] ;

$$\sum_{\mathbf{q}'p'} \Big[(n_{\mathbf{q}p} - n^0_{\mathbf{q}p}) - (n_{\mathbf{q}'p'} - n^0_{\mathbf{q}'p'}) \Big] Z^{\mathbf{q}'p'}_{\mathbf{q}p} - \mathbf{v}_p(\mathbf{q}) \cdot \nabla T \frac{\partial n^0_{\mathbf{q}p}}{\partial T} = 0, \tag{2.4.1}$$

where $n_{\mathbf{q}p}$ is the distribution for phonon, ($\mathbf{q}$) is the wave-number, p is the polarization, $n^0_{\mathbf{q}p}$ is the equilibrium distribution, $Z^{\mathbf{q}'p'}_{\mathbf{q}p}$ is the intrinsic probability and $\mathbf{v}_p(\mathbf{q})$ is group velocity of phonon $(\mathbf{q}, p)$ T is temperature. The Phonon-phonon umklapp scattering can be written in the form [90];

$$\tau_U^{-1}(\omega) = B_U \omega^2 T e^{-\theta/3T}, \tag{2.4.2}$$

with

$$B_U \approx \frac{\hbar \gamma^2}{M v^2 \theta}, \tag{2.4.3}$$

where γ is the Grüneisen parameter, ω is the frequency, M is the average mass of an atom and θ is the Debye temperature [**?**].

2.5 Transport theory

It is good to understand the electrical and thermal transport behavior of thermoelectric materials, to help in finding a suitable material [91].

2.5.1 Transport equation

The expression of transport equation was stated by Liouville theorem, for a distribution function of particles;

$$\frac{df}{dt} = \frac{\partial f}{\partial t} + \Big[\frac{\partial f}{\partial t}\Big]_{\text{external}} + \Big[\frac{\partial f}{\partial t}\Big]_{\text{internal}}, \tag{2.5.1}$$

where $f(\mathbf{r}, \mathbf{k}, t)$ is the carrier distribution function, $\mathbf{r}$ and $\mathbf{k}$ are position and wave vectors, respectively, and t is time, and also, the internal and external are denote the changes of f under external forces and internal phenomena, respectively. The carriers equation can be also written as;

$$-\Big[\frac{\partial f(\mathbf{r}, \mathbf{k})}{\partial t}\Big]_{\text{external}} = \mathbf{v}\cdot\nabla_r f + \frac{d\mathbf{k}}{dt}\cdot\nabla_k f = \Big[\frac{\partial f}{\partial t}\Big]_{\text{internal}}, \tag{2.5.2}$$

where $\mathbf{v}$ is the carriers velocity. ∇_r, ∇_k are gradients with respect to position and wave vector, respectively. The relaxation time can be define as $\tau(\mathbf{k})$, which can represent $\Big[\frac{\partial f}{\partial t}\Big]_{\text{internal}} = -\frac{f-f_0}{\tau(\mathbf{k})}$, where f and f_0 are the slightly and the equilibrium perturbed distribution function, respectively [92]. The expression of transport equation including relaxation time becomes;

$$-\frac{f - f_0}{\tau(\mathbf{k})} = \mathbf{v}\cdot\nabla_r f + \frac{d\mathbf{k}}{dt}\cdot\nabla_k f. \tag{2.5.3}$$

2.5.2 Seebeck coefficient and electrical conductivity

The definition of the Seebeck coefficient can be written as;

$$S = \frac{dV}{dT} = \frac{1}{e}\Big(\frac{\partial E_f/\partial \mathbf{r}}{\partial T/\partial \mathbf{r}}\Big), \tag{2.5.4}$$

where S in equation above is given by;

$$S = \pm\frac{1}{eT}\Big[E_f - \int_0^\infty g(E)\tau E^2\frac{\partial f_0(E)}{\partial E}dE \Big/ \int_0^\infty g(E)\tau E\frac{\partial f_0(E)}{\partial E}dE\Big], \tag{2.5.5}$$

where $g(E)$ is the electron density of states. The negative sign of the Seebeck coefficient indicates that carriers are electrons, and the positive sign of the Seebeck coefficient indicates carriers are holes [93]. On the other hand, the expression of electrical conductivity

can be given as;

$$\sigma = \frac{2e^2}{3m^*}\int_0^\infty g(E)\tau E\frac{\partial f_0(E)}{\partial E}dE, \tag{2.5.6}$$

where m^* is the effective mass.

2.5.3 Thermal conductivity (κ)

To understand how the material response to the heat transfer, one should examine its thermal conductivity. The thermal conductivity has two main components, the electronic and lattice contributions to total thermal conductivity.

Electronic thermal conductivity (κ_e)

The electronic thermal conductivity is due to the collision between the electrons during their movement when the temperature is raised. The electronic thermal conductivity component is an important part, especially when we have heavy doped semiconductor. The expression of κ_e can be written as;

$$\kappa_e = \frac{3}{2}\Big(\frac{k_B}{e}\Big)^2\sigma \mathrm{T}, \tag{2.5.7}$$

where k_B is Boltzmanns constant, σ is the electrical conductivity, and T is kinetic energy of carriers.

Lattice thermal conductivity (κ_L)

The lattice thermal conductivity means, heat conduction via vibrations of the lattice ions in a solid [94]. Hence, the lattice thermal conductivity can be determine using the Boltzmann equation [88, 89]. In the single-mode relaxation-time approximation [95], the lattice thermal conductivity can be expressed as;

$$\kappa_L = \frac{1}{Z\Omega}\sum C\mathbf{v}\otimes\mathbf{v}\tau, \tag{2.5.8}$$

where Z, Ω and τ are the unit cell number, unit cell volume and the relaxation time or phonon lifetime respectively. C is the heat capacity that is expressed as;

$$C = k_B\Big(\frac{\hbar\omega}{k_BT}\Big)^2\frac{e^{(\hbar\omega/k_BT)}}{[e^{(\hbar\omega/k_BT)}-1]^2}, \tag{2.5.9}$$

where $\omega = \omega(\mathbf{q})$ is the phonon frequency, T is the temperature whereas k_B and $\hbar$ indicate the reduced Boltzmann constant and Planck constant, respectively. $\mathbf{v}$ is phonon group velocity that given by;

$$\mathbf{v} = \nabla_{\mathbf{q}}\omega(\mathbf{q}, j), \tag{2.5.10}$$

3

Computational details

In this chapter, we address the calculation details of DFT, MBPT and Boltzmann transport equations that have been applied in this thesis.

3.1 DFT Calculations

All ground state calculations were carried out using Density Functional Theory (DFT) with plane wave projector-augmented (PAW) pseudopotential formalism [96], as implemented in the Vienna *ab-initio* simulation package (VASP) [97, 98]. Within the generalised gradient approximation (GGA), the exchange-correlation functional was approximated by the Perdew-Burke-Ernzerhof (PBE) [69] formulation, while the optB86b-vdW [99] functional was used to capture the van der Waal's interactions as a result of the layered nature of the structure. The electron wave function was expanded in a plane wave basis set with an energy cut-off of 520 eV for bulk and 350 eV for bilayer and monolayers, in all calculations. A sampling of the Brillouin zone was performed using Monkhorst-Pack grid, [74] an 8×8×6 the Gamma centred k-point mesh for bulk, and a 12×12×1 the Gamma centred k-point mesh for bilayer and monolayer. Ground-state geometry of bulk, bilayer and monolayer were fully relaxed until the force on each atom was less than 1×10^{-3} eV/ Å. The energy-convergence criterion was 1×10^{-8} eV, for bulk, bilayer and monolayer. For the thermal properties calculations, were created a supercell of 4×4×4 for bulk and 5×5×1 for bilayer and monolayer from their relaxed pristine unit-cell. In order to avoid any artificial interlayer interaction, a vacuum layer

of 15 Å along c direction was added for bilayer and monolayer calculations.

3.2 Structural Properties

3.2.1 Lattice parameter

The equilibrium lattice constant for PtX_2 compounds were optimized by finding the minima of the energy as a function of the lattice constant. The total energy as a function of lattice spacing is obtained by varying the lattice constants, with full relaxations of all the atoms. The fully relaxed structure from PBE and optB86b-vdW are used to perform the EOS static calculation using the Blöchl tetrahedron correction to extract energy. From which the lattice parameter is extracted [100].

3.2.2 Cohesive energy

Cohesive energy was investigated at the equilibrium lattice structures. It is the negative of the energy that must be supplied to the solid to separate its constituents into neutral free atoms at rest and at infinite separation, the cohesive E_{coh} can be written in form;

$$E_{\text{coh}}^{(\text{PtX}_2)} = \frac{E_{\text{comp.}}^{(\text{PtX}_2)} - N \times (xE_{\text{atom}}^{(\text{Pt})} + yE_{\text{atom}}^{(\text{X})})}{N \times (x+y)}, \tag{3.2.1}$$

where N is the number of PtX_2 unit per unit cell, $E_{\text{atom}}^{\text{Pt}}$ and $E_{\text{atom}}^{\text{X}}$ are the atomic energies of Pt and X, while x and y are the number of Pt and X atoms per unit cell, respectively.

3.2.3 Formation energy

Formation energy, E_{form}, is used to verify the relative phase stabilities for any compound. Formation energy is that energy required to decompose a compound into its most stable constituent compounds. which is given by

$$E_{\text{form}}^{(\text{PtX}_2)} = E_{\text{coh}}^{(\text{PtX}_2)} - \Big[\frac{xE_{\text{coh}}^{(\text{Pt})} + yE_{\text{coh}}^{(\text{X})}}{x+y}\Big]. \tag{3.2.2}$$

where $E_{\text{form}}^{(\text{PtX}_2)}$ is the total cohesive energy per PtX_2 unit cell; $E_{\text{coh}}^{(\text{Pt})}$ and $E_{\text{coh}}^{(\text{X})}$ the cohesive energy per atom for Pt and X atoms, respectively. The parameters x and y are defined is section (3.2.2)

3.3 Stabilities

3.3.1 Mechanical stability

Elastic constants are crucial parameters, through their knowledge, one can predict and derive a useful mechanical coefficient of a material. For bulk PtX_2, in crystal structure of a trigonal, has six independent elastic constants, C_{11}, C_{12}, C_{13}, C_{14}, C_{33} and C_{66} which are similar to tetragonal crystal. The elastic matrix satisfy the Born criterion $C_{66} = (C_{11}, C_{12})/2$, $C_{11} > |C_{12}|$ and $2C_{13}^2 < C_{33}(C_{11}, C_{12})$ [101, 102].

In this research, we calculated the elastic constants and investigated the elastic properties by two independents coefficient, Young's modulus Y and Poisson's ratio ν. The Young's moduli describes the hardness of materials, while Poisson's ratio (ν) provides information on bonding nature [103]. The elastic constants (C_{ij}) (i and j are matrix dimensions) were used to define these coefficients. For bulk, we used the Young's modulus in formula

$$Y = \frac{1}{V_0}\Big(\frac{\partial^2 E_s}{\partial \varepsilon^2}\Big), \tag{3.3.1}$$

where E_s, ε and V_0 are the strain energy, the uniaxial strain and volume, respectively, since the bulk is a 3D (three-dimensional) structure which depends on volume V_0. Since the bilayer and monolayer is 2D (two dimensional), so we focus of the in-plane Young's moduli which is depends on the equilibrium in-plane area, A_0, of the supercell and the strain energy. The Young's moduli is defined as

$$Y = \frac{1}{A_0}\Big(\frac{\partial^2 E_s}{\partial \varepsilon^2}\Big),. \tag{3.3.2}$$

To obtain the Young's modulus and Poisson's ratio ν for a bulk we used Hill's approach [104], and for a bilayer and monolayer, we used two independent elastic constants, C_{11} and C_{12} [105]. The two dimensional expression for Y can also be written in terms of

elastic constants as [41, 105, 106, 107, 108]

$$Y = (C_{11}^2 - C_{12}^2)/C_{11}, \tag{3.3.3}$$

and the two dimensional Poisson's ratio can be expressed as

$$\nu = C_{12}/C_{11}. \tag{3.3.4}$$

3.3.2 Dynamical stability

The associated collective excitation for crystal lattice vibrations is called the phonons [95]. Highly converged forces were required for the calculations of the dynamical matrix using the direct force constant approach as implemented in the PHONOPY package [109]. We employed a 4×4×4 supercell for bulk and 5×5×1 supercell for bilayer and monolayer. The phonon dispersion relations were computed along several high symmetry directions using relaxed lattice parameters. The gap usually observes between the acoustic and optical mode, indicates that the difference in mass between Pt atom mass and X atomic mass according to Eq. 3.3.5. It is clear that Pt atoms have more contribution in the low frequency region which is acoustic region, and X atoms have more contribution in the high frequency which is optical mode region.

$$\omega_{\pm}^2 = K\Big(\frac{1}{M_1} + \frac{1}{M_2}\Big) \pm K\sqrt{\Big[\Big(\frac{1}{M_1} + \frac{1}{M_2}\Big)^2 - \frac{4sin^2(\mathbf{q}a/2)}{M_1 M_2}\Big]}, \tag{3.3.5}$$

where ω is frequency M_1, M_2 is the mass of Pt and X atoms, respectively, K is spring constant, $\mathbf{q}$ wave vector and a are the separate distance between two mass [110]. The two solutions of Eq. 3.3.5 are two branches of phonon, the plus sign, for the optical mode, and the minus sign is for the acoustic mode.

3.4 Electronic properties

A diagram of the electronic energy band is the essential quantity that characterises the electronic structure of a solid and determines its ground state and a series of excitations involving electronic states [111]. Electronic structure properties are defined by band structure and density of states (DOS), which clarify the occupied and unoccu-

pied electronic states. The band gap is the forbidden states that located between the valence and conduction bands, the magnitude of band gap is classifying the materials into insulators, semiconductors or metals. Moreover, the band structure diagram is used to distinguish the nature of the band gap (direct or indirect) depending of the position of the maximum valence band (MVB) and minimum conduction band (MCB) with respect to the k-points. The DOS is a simple form describing the condenses of the band structure properties for the occupied state in reciprocal space [112]. Total DOS is combined from the projection DOS that shows the contribution of the orbitals. The band gap can be defined through the DOS by top edge of the valence and bottom edge of the conduction. The calculation of the electronic structure was done in the Brillouin zone along the high symmetry path. We used the optimized lattice parameter for bulk, bilayer and monolayer, and k-point of 8×8×6 for bulk and 12×12×1 for bilayer and monolayer in carrying out the electronic studies.

3.5 Optical coefficient

The optical coefficients were determined as follows, the imaginary part $\varepsilon_1(\omega)$ of the dielectric function is obtained from the momentum matrix elements between the occupied and unoccupied wave-functions. The real part $\varepsilon_1(\omega)$, is defined by the Kramer-Kronig relations [113], whereas the absorption coefficient $\alpha(\omega)$ is derived from the dielectric function as follows: [114].

$$\varepsilon_{2,\alpha\beta}(\omega) = \frac{4\pi^2 e^2}{\Omega} \lim_{q\to 0} \frac{1}{q^2} \sum_{CV\mathbf{k}} 2w_{\mathbf{k}} \delta(\epsilon_{C\mathbf{k}} - \epsilon_{V\mathbf{k}} - \omega) \times \langle u_{C\mathbf{k}+e_\alpha q} | u_{V\mathbf{k}} \rangle \langle u_{C\mathbf{k}+e_\beta q} | u_{V\mathbf{k}} \rangle^*, \tag{3.5.1}$$

$$\varepsilon_{1,\alpha\beta}(\omega) = 1 + \frac{2}{\pi} \mathbf{P} \int_0^\infty \frac{\varepsilon_{2,\alpha\beta}(\omega')\omega' d\omega'}{\omega'^2 - \omega^2}, \tag{3.5.2}$$

$$\alpha(\omega) = \frac{\sqrt{2}\omega}{c} \left[\sqrt{\varepsilon_{1,\alpha\beta}^2(\omega) + \varepsilon_{2,\alpha\beta}^2(\omega)} - \varepsilon_{1,\alpha\beta}(\omega) \right]^{1/2}, \tag{3.5.3}$$

where $w_{\mathbf{k}}$ is the k-points weight, Ω is the volume of the unit cell, e_α are unit vectors, and V and C are induces restricted to the valence and conduction band, respectively. While $\mathbf{P}$ refer to the principal value, α and β are tensor dimensions, ω is frequency and c is the speed of light.

The investigation of the optical properties for the bilayer and monolayer were performed using a supercell, where a single layer was included per supercell. For comparison of the bulk, bilayer and monolayer, we obtained the optical absorbance, and the percentage of the radiation absorbed, in the visible photon energy range of $1 - 3$ eV, by a single layer in the bulk, bilayer and a monolayer. The computed results for a single layer of bulk, bilayer and monolayer were calculated by using the absorbance, $A = 1 - exp(-\alpha(\omega)\Delta z)$, where $\alpha(\omega)$ is the absorption coefficient and Δz is the thickness of a slab of the material. For comparison with a bilayer and a monolayer, we set Δz equal to the thickness of a single layer in the bulk. While for the bilayer and monolayer, the absorption coefficient scales like the inverse of the length of the supercell perpendicular to the layer for a sufficiently large supercell and the correct value of Δz in a periodic supercell calculation is the length of the supercell perpendicular to the layer [115, 116].

We described the absorption edge using the Tauc plot of the optical dispersion, the Tauc method [117] determine absorption edge by linear extrapolation of $(\alpha h\nu)^{\frac{1}{n}}$ to zero from an equation $\alpha h\nu = K(h\nu - E_{\mathrm{g}})^{\mathrm{n}}$. Where E_{g} is the gap, α is absorption, $h\nu$ the photon energy, K the proportionality constant and the exponent n takes values 2, $\frac{1}{2}$, $\frac{3}{2}$ and $\frac{1}{3}$ for direct, indirect, allowed and forbidden transitions, respectively.

3.6 Lattice thermal conductivity

The lattice thermal conductivity calculation was done using the PHONO3PY package [109] that solves the single-mode relaxation-time approximation of the linearised phonon Boltzmann transport equation. A 4×4×4 supercell for bulk and 5×5×1 supercell for bilayer and monolayer were used for solving the linearised lattice Boltzmann transport equation in the single-mode relaxation time approximation PHONO3PY package [95]. In the thermal conductivity calculation, 2753 for bulk, while 3700 and 950 for bilayer and monolayer, respectively. A unique triplet displacements were included in the calculation of the scattering terms [95]. The normal unit for thermal conductivity is $\mathrm{Wm^{-1}K^{-1}}$ per unit cross-sectional area, which gives the thermal conductivity of a volume of material

of a cross-sectional area of 1 m^2 and 1 m thick, with heat conducted perpendicular to the cross-sectional area. For a single layer, the cross-sectional area for out-of-plane thermal conductivity is taken as 1 m^2, but the thickness is that of a single layer. The cross-sectional area for single layer in-plane thermal conductivity is that of the cross-sectional area of a single layer perpendicular to the plane of the layer. The 'thickness' is taken as 1 m. For single layers we use units of $Wm^{-1}K^{-1}$ per cross-sectional area (not per unit cross-sectional area), where the cross-sectional area and thickness depends on the direction in which the heat flow is measured. With this definition, the units for thermal conductivity are consistent for bulk and single layers [1].

3.7 Transport phenomena

We used the deformation potential and elastic constants to calculate a set relaxation times of charge carrier which were dependent on k-point and energy, as proposed by Bardeen and Shockley [118]. To determine the electronic transport coefficients, we used these relaxation time. The BoltzTraP2 package [119] was used to solve the Boltzmann transport equations resulting in the approximate values of various transport coefficients such as S, σ and κ_e as the output. The calculation of transport coefficients as a function of temperatures such as Seebeck, power factor, electrical conductivity, and thermal conductivity, was done for a single layer in bulk, bilayer, and monolayer, to investigate the thermoelectric potential of this binary compounds. The in-plane coefficients were considered for a single layer in bulk, bilayer and monolayer calculations. The concentrations of charge carriers which were used are 10^{19} and 10^{20} cm^{-3} for all PtX_2 except, the bulk of PtO_2 when we used 10^{20} and 10^{21} cm^{-3}. The range of temperature considered varies since it depends on the melting point for each compound.

4

Results and Discussions

The structural, mechanical and dynamical stabilities, electronic, optical and thermoelectric properties of trigonal structure PtX_2 (X = O, S, Se and Te) were investigated in this section, based on the theoretical methods (Chapter 2) and computational details (Chapter 3), the obtained results are presented and discussed. Figure 4.1 illustrated the bulk, bilayer and monolayer (a) bulk unit cell, (b) monolayer unit cell, (c) top view of the monolayer, and (d) side view of the monolayer. The Octahedral coordination 1T shows Platinum atoms sandwiched (X-Pt-X) between two layers of X atoms.

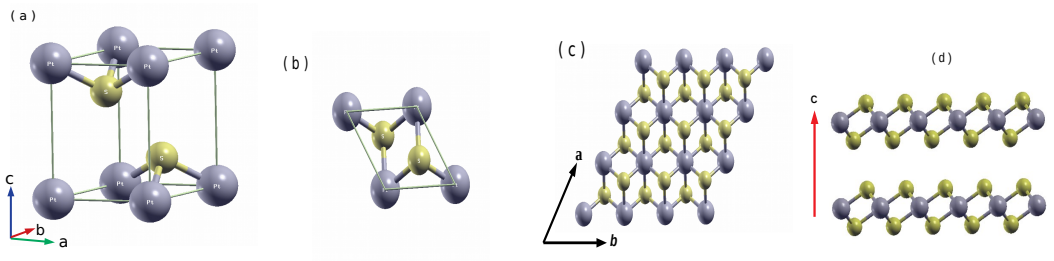


Figure 4.1: Crystal structure of bulk, bilayer and monolayer PtX_2. (a) the bulk structure unit cell, (b) the monolayer structure unit cell, (c) top view of monolayer and (d) side view of bilayer. The Pt atoms and X atoms are represented by grey and red ball, respectively.

4.1 Platinum dioxide (α-PtO_2)

4.1.1 Structural Properties

In Table 4.1, we listed the equilibrium lattice constant (a, c and V_0) of the bulk, bilayer and monolayer α-PtO_2. The lattice parameters of bulk obtained using optB86b-vdW functional are close to the experimental results, while those from the PBE functional are slightly overestimated. The calculated lattice parameters of bilayer and monolayer are similar to the previous study for monolayer. The optB86b-vdW approximation includes an approximation of long-range interaction. This could explain the difference between the results from the two functionals. On the other hand, we set $c = 15\mathring{A}$ as a vacuum layer for bilayer and monolayer which is make the vad der Waal's force between the layers to be weak. The investigation of the phase stability was done using the cohesive and formation energies as defined in Chapter 3, using Equation (3.2.1) and (3.2.2), respectively. In Table 4.1, we listed the cohesive and formation energies per atom for bulk, bilayer and monolayer, and compared with available previous studies. Cohesive and formation energies are used to study phase stability in the solid-state. Our calculations gave a negative of cohesive energy and formation energy, indicative of energetically stable compounds. the values of cohesive energy and formation energy are independent of the approximation used.

Table 4.1: Calculated, experimental and theoretical optimized lattice constants of bulk, bilayer and monolayer α-PtO_2, cohesive (E_{coh}) and formation formation energies per atom, and inter-layer distance.

		a (Å)	c (Å)	V_o (Å^3)	E_{coh} (eV)	E_{form} (eV)
Bulk	PBE	3.15	4.91	42.32	-4.35	-0.49
	optB86b-vdW	3.12	4.36	36.92	-4.54	-0.44
	Exp[120]	3.11	4.34	36.44	–	–
	Exp[121]	3.10	4.16	34.63	–	–
	Exp[122]	3.08	4.19	34.42	–	–
Bilayer	PBE	3.12	15	–	-4.37	-0.51
	optB86b-vdW	3.12	15	–	-3.30	-1.11
Monolayer	PBE	3.12	15	–	-4.37	-0.51
	optB86-vdW	3.12	15	–	-3.27	-0.41
	Previous work[123]	3.14	–	–	–	-0.40

4.1.2 Mechanical stability

In this section we examine the mechanical stability for bulk, bilayer and monolayer α-PtO_2. The elastic constants listed in Table 4.2, fulfil the Born stability criteria [102] see section (3.3.1), which indicate that bulk, bilayer and monolayer α-PtO_2 are mechanically stable. The Young's moduli and Poisson's ratio for α-PtO_2, were obtained for bulk, bilayer and monolayer are represented in Table 4.3. We observe that Young's moduli increases with the increase of the number of layers, indicative of increased resistance to deformation under the application of opposing forces as the number of layers are increased. The results agree with previous study [41], for monolayer. In Table 4.3, we present the calculated Young's moduli (Y) and Poisson's ratio (ν) for bulk, bilayer and monolayer α-PtO_2, and bulk moduli and shear moduli for bulk α-PtO_2. The calculated results for bilayer and monolayer are in accordance with the calculated value of in-plane stiffness for MoS_2, which is 123 GPa, while the Poisson's ratio in accordance with Si and MoS_2 which are 0.30 and 0.25, respectively, reported in ref [124].

Table 4.2: Elastic constants (C_{ij} (GPa)) for bulk, bilayer and monolayer α-PtO_2.

		C_{11}	C_{12}	C_{13}	C_{33}	C_{66}
Bulk	optB86b-vdW	270.42	70.26	20.81	25.89	100.08
Bilayer	PBE	122.22	38.12	–	–	–
Monolayer	PBE	178.87	53.12	–	–	–

Table 4.3: The obtained Bulk moduli (B) Shear moduli (G),Young's moduli (Y) and Poisson's ratio (ν) in GPa, for bulk, bilayer and monolayer.

		B	Y	G	ν
Bulk	optB86b-vdW	56.78	100.45	41.68	0.21
Bilayer	PBE	–	110.33	–	0.31
Monolayer	PBE	–	116.18	–	0.23

4.1.3 Dynamical Stability

The phonon calculations for the bulk α-PtO_2 were done using the optb86B-vdw relaxed structure. Since optB86b-vdW and PBE functions gave the same equilibrium lattice parameters for bilayer and monolayer, so we used PBE for phonon calculations since it is computationally less demanding. The phonon dispersion was calculated along with

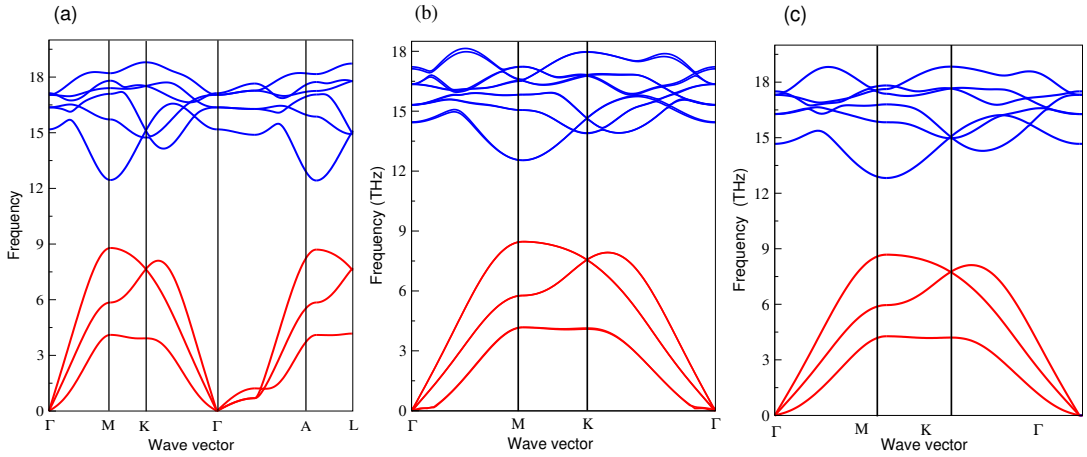


Figure 4.2: The band structure of phonon dispersion for α-PtO_2. (a) Bulk (b) Bilayer (c) Monolayer.

several high symmetry directions. Figure 4.2 shows the phonon dispersion band structure and 4.3 shows the phonon dispersion density of states and atoms contribution, relations of α-PtO_2 bulk, bilayer and monolayer, computed at the equilibrium configuration zero pressure using the PHONOPY package [125, 109]. The phonon frequencies are positive throughout the Brillouin with zone, which indicates that the bulk, bilayer and monolayer compounds are dynamically stable. The phonon frequencies are in the range of $(0 - 18.73)$ THz for bulk, $(0 - 18.12)$ THz for bilayer and $(0 - 18.83)$ THz for the monolayer, respectively. Note, the bilayer phonon band structure appears dense compared to the bulk and monolayer. This is due to the increase in the number of atoms per unit cell, while the frequency range is almost unchanged for all three configurations. The bulk and monolayer of the primitive cell of α-PtO_2 contain three atoms and therefore there are nine phonon modes for each wave vector (three acoustic modes and six optical modes). For the bilayer, the primitive cell of α-PtO_2 contains six atoms and therefore, there are eighteen phonon modes or each wave vector (six acoustic modes and twelve optical modes). The highest frequency of the acoustic modes, defined here as the acoustic cut-off, is approximately 8.8 THz for bulk, 8.42 THz for bilayer and 8.68 THz for monolayer. Figure 4.2(a-c) depicts the phonon band structure for bulk, bilayer and monolayer, respectively, and the total density of states and atoms contribution are shown in Figure 4.3(a-c). The phonon band structure and density of states for bulk, bilayer and monolayer show the same behaviour. It is evident that (O) controlled in the frequency optical region, and (Pt) contributes more in the frequency acoustic region.

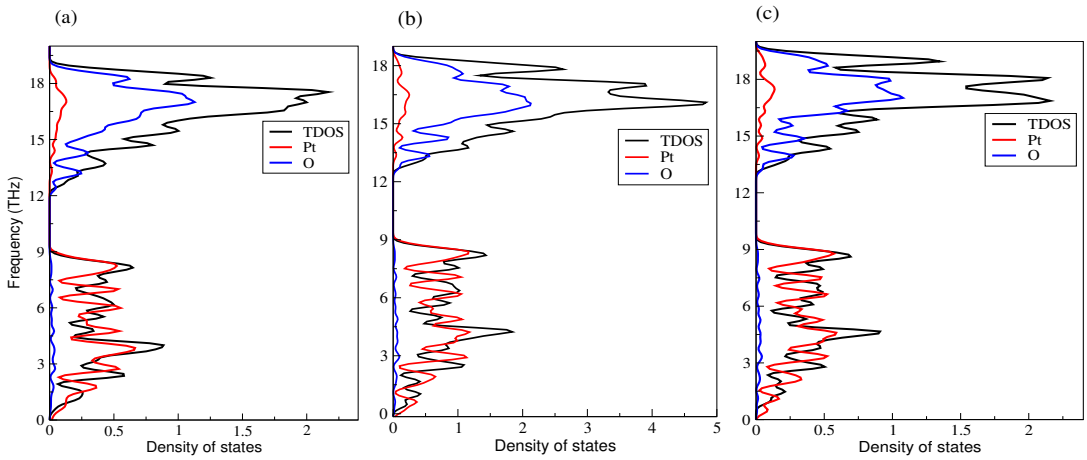


Figure 4.3: Phonon total and partial density of states for α-PtO_2. (a) Bulk (b) Bilayer (c) Monolayer.

Table 4.4: The calculated band gaps compared to the experimental and theoretical (in eV) of α-PtO_2.

	optB86-vdW	PBE	GW_0	Experimental	Previous work
Bulk	1.61	1.63	2.73	1.30 - 1.47[34],1.2[35]1.84[36]	–
Bilayer	1.63	1.74	4.36	—	—
Monolayer	1.72	1.86	4.73, 4.00[123]	—	2.00[123]

4.1.4 Electronic structure properties

The electronic band structure of bulk, bilayer and monolayer α-PtO_2 are presented in Figure 4.4(a-c), respectively. They all exhibited an indirect semiconductor band gap, of values 1.61, 1.73 and 1.86 eV, respectively. MVB and MCB are located between Γ and M points for bulk, and between A and L points for bilayer and monolayer. We also present the total and partial density of states (TDOS and PDOS) in Figure 4.4(a-c) for bulk, bilayer and monolayer α-PtO_2, respectively. The maximum and minimum edge of the band gap in density of states, which is caused by valence and conduction band, respectively, are contributed by Pt(s), Pt(d) in valence band, while the minimum conduction band is mainly due to the Pt(s), Pt(d) and O(p) orbitals for all the three structures. It is important to point out that the band structure of bilayer looks denser than than of the bulk and monolayer while its DOS is also higher. This is due to the difference in the number of atoms in the primitive cell, as we mentioned before. We summarise our calculated fundamental band gap values in Table 4.4 and compared with available experimental values.

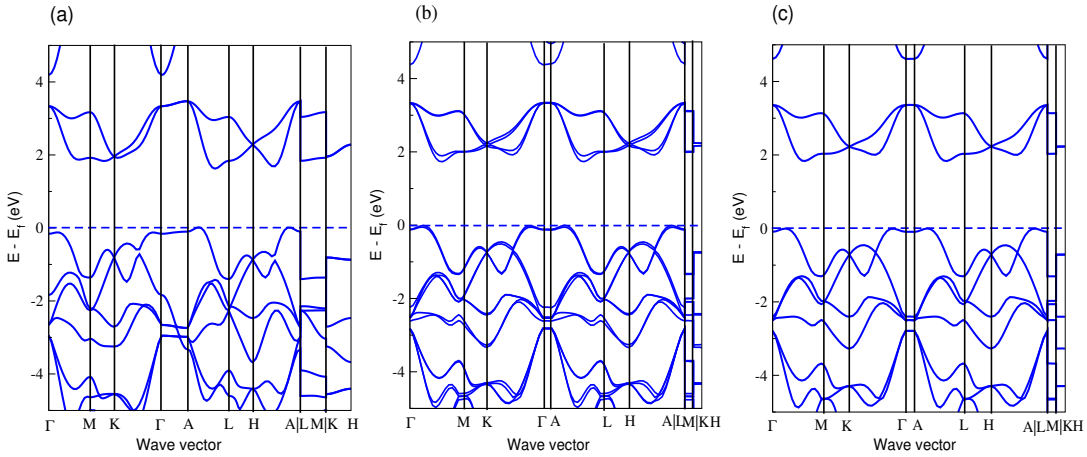


Figure 4.4: Calculated electronic structure of α-PtO_2. (a) Bulk (b) Bilayer (c) Monolayer.

Carolyn R A [34] used x-ray photoelectrons spectroscopy to determine the optical properties of the bulk α-PtO_2. The absorption coefficient and the optical transitions of infrared show that its optical band gap varies between 1.30 and 1.47 eV. An optical band gap of 1.2 eV was obtained for α-PtO_2 by Neff H *et al.* [35], using x-ray diffraction, energy-sensitive microanalyses, optical reflectance measurements and resistivity. Scanning tunnelling spectroscopy measurements by Zhensheng J *et al* [36], give a optical gap of 1.84 eV. Hence, our calculated results are range of experimental values which vary from 1.2 to 1.84 eV. The bilayer and monolayer band gap are represented in Table 4.4, the monolayer value is high than bilayer hence, the value of bilayer also higher than of bulk.

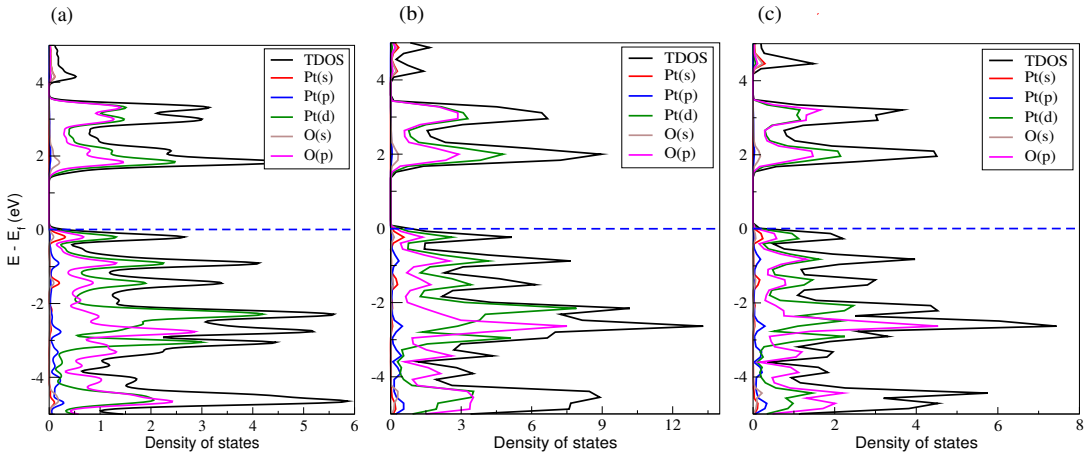


Figure 4.5: Calculated total and partial DOS. (a) Bulk (b) Bilayer (c) Monolayer.

4.1.5 Optical properties

In this section, we use Equation 3.5.1, 3.5.2 and 3.5.3 as defined in Chapter 3 to calculate the imaginary and real parts of the dielectric functions. The absorption and absorbance as well as other related parameters were then derived from the dielectric functions. Figure 4.6(a-c) depict the imaginary and real parts of the dielectric functions and the absorbance respectively, computed with the BSE GW_0 approximation. Figure 4.7(c) illustrate the absorbance of bulk, bilayer and a monolayer. The maximum absorbance in in-plane polarization for monolayer is $\approx 8.06\%$ at 2.92 eV and for bilayer is $\approx 5.64\%$ at 2.51 eV and 0.91% at 2.12 eV for bulk. The absorbance of a monolayer is considerably greater than the absorbance for a bilayer and bulk. This agrees with MoS_2, $MoSe_2$ and WS_2 results (5−10%) [115, 116], where the single layer absorbance is high in monolayer than bilayer and bulk. Moreover, in the out-of-plane polarisation, the maximum absorbance is $\approx 0.09\%$ at 2.99 eV for monolayer and $\approx 0.39\%$ at 2.82 eV for bilayer and 0.14% at 2.15 eV for a single layer of bulk. The optical band gap was obtained by fitting our BSE optical data on the Tauc plot [117]. It is worth mentioning that the BSE is considered up to date as the best of estimation for the optical properties as it included the two particles Green's function. For the bulk α-PtO_2, the in-plane and out-of-plane optical band gap polarizations are 1.66 and 1.77 eV, respectively, which is an average of the experimental measurements range. The difference of two values suggests significant optical anisotropy, and it suits to photovoltaic solar cells applications [126]. The calculated optical band gaps of the in-plane and out-of-plane polarization, for the monolayer, are 2.32 and 2.75 eV, and for bilayer are 1.89 and 2.34 eV, while for bulk are found to be 1.63 and 1.77 eV, respectively. Also suits to photovoltaic solar cells applications.

4.1.6 Lattice thermal conductivity

Figure 4.7(a) and (b) show the lattice thermal conductivity against temperature and frequency, respectively, for a single layer of bulk, bilayer and monolayer α-PtO_2 structure. The average lattice thermal conductivity at 300 K for single layer in bulk, bilayer and monolayer is 8.47×10^{-8}, 4.59×10^{-8} and 1.06×10^{-8} $Wm^{-1}K^{-1}$ in-plane direction for bulk, bilayer and monolayer respectively, in the out-of-of the plane direction, we found it to be 0.05×10^{-8} $Wm^{-1}K^{-1}$ for bulk and zero for the others. The lattice thermal conductivity for a single layer in bulk decreases by about ∼46% of the bilayer and

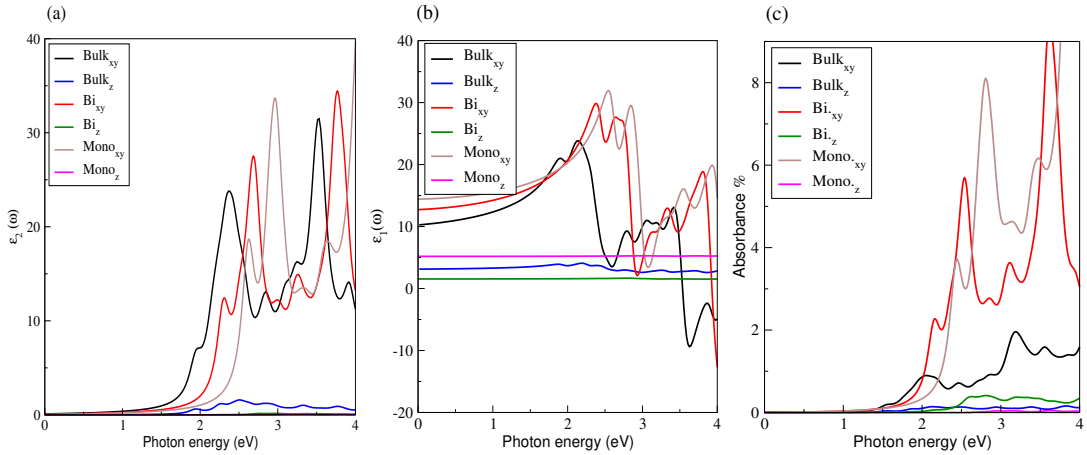


Figure 4.6: (a) Imaginary part $\varepsilon_2(\omega)$, (b) real part $\varepsilon_1(\omega)$ of dielectric function and (c) absorbance for bulk, bilayer and monolayer of α-PtO_2.

$\sim$87% of the monolayer, in the in-plane. Furthermore, a high in-plane lattice thermal conductivity was found to be at the low-temperature. For instance, our calculations predict a value of 24.61×10^{-8} $Wm^{-1}K^{-1}$ at 70 K for bulk, and 18.90×10^{-8} $Wm^{-1}K^{-1}$ at 50 K for bilayer and 2.19×10^{-8} $Wm^{-1}K^{-1}$ at 100 K for monolayer. The high out-of-plane is 0.52×10^{-8} $Wm^{-1}K^{-1}$ at 10 K for bulk. The lattice thermal conductivity against frequency at 300 K is presented in Figure 4.7(b), and its cumulative lattice thermal conductivity as a function of the frequency of single layer for bulk, bilayer and monolayer. We observed that the lattice thermal conductivity is highly anisotropic, with the thermal conductivity in-plane of the layers being much higher than that of the out-of-plane direction for two cases bulk, bilayer and monolayer. Furthermore, we calculated the directional projected density of states for each atom as a function of frequency. Figure 4.8 shows the in-plane and out-of-plane contributions, left and right, respectively, which are along [100] and [001]. The results of directional projected density of states look like phonon density of states, but here we have directional contributions. The Pt atoms contributed more in acoustic mode than O atoms and vice versa for optical mode for all bulk, bilayer and monolayer, in the in-plane direction. In the out-of-plane direction, we only have the contribution for bulk. To know the contribution ratio of phonon to lattice thermal conductivity, we examine the contribution of acoustic and optical phonons branches mode. At 300 K, the in-plane (out-of-plane) acoustic mode total contribution to the thermal conductivity is 94% (77%), 96.65% (0%) and 93% (0%) for bulk, bilayer and monolayer α-PtO_2 respectively. The contributions of phonon to lattice thermal conductivity per atoms are illustrated in Figure 4.9 (left and

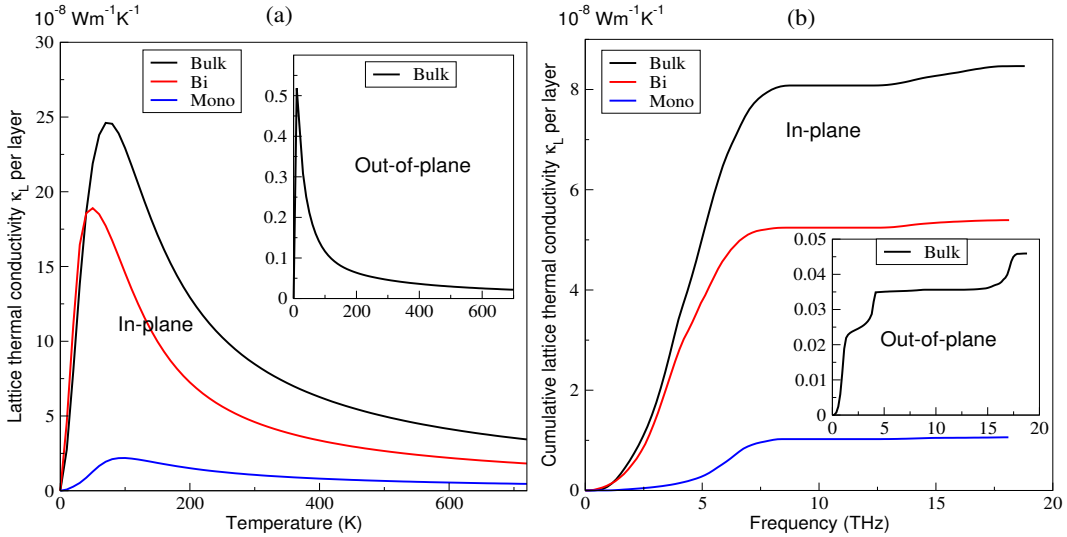


Figure 4.7: Lattice thermal conductivity and heat capacity for bulk and monolayer α-PtO_2. (a) Lattice thermal conductivity against temperature, (b) cumulative lattice thermal conductivity against frequency.

right), for bulk, bilayer and monolayer. Through Figure 4.9, we can note that the ratio of contribution is almost the same in in-plane, for bulk, bilayer and monolayer. The out-of-plane contribution of the bulk is given at the right. This is in clear contrast to the conventional understanding, especially in the out-of-plane direction, where the acoustic modes dominate thermal conductivity [127].

Phonon lifetime

The phonon lifetime is the time between two phonon-phonon scattering events and it is obtained by third-order force constants [90, 95]. Figure 4.10(a-c) shows how the bulk, bilayer and monolayer α-PtO_2 phonon lifetime depends on frequency, at 300 K. The highest peak for phonon lifetime is located in acoustic mode, and while the lowest peak for phonon lifetime is located in optical mode for all structures. This is in accordance with a somewhat powerful scattering in the high frequency optical phonon modes. To differentiate the phonon lifetime contributions to the total lattice thermal conductivity, one can use the phonon lifetime distribution of acoustic and optical phonon mode [128].

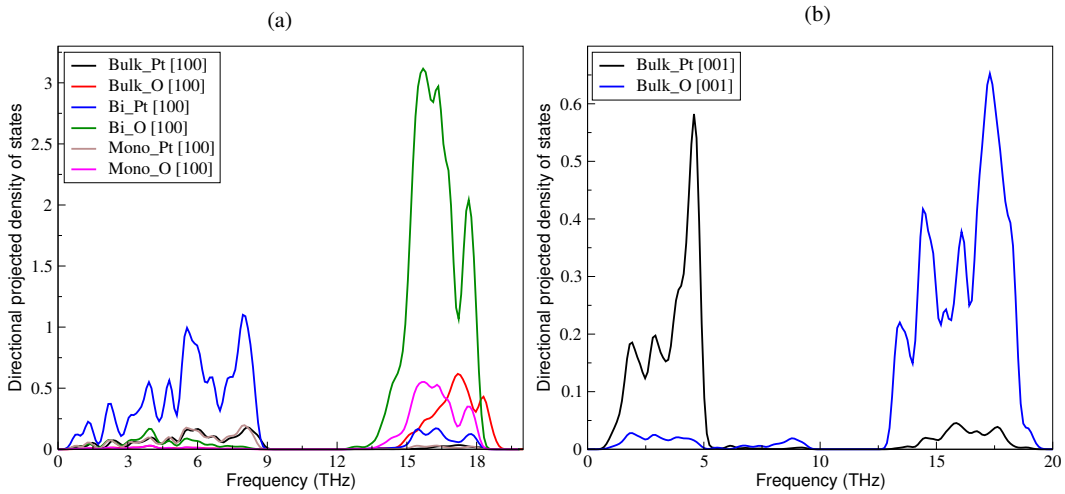


Figure 4.8: Directional projected density of states, left is in-plane and right is out-of-plane for bulk, bilayer and monolayer α-PtO_2 as function of frequency.

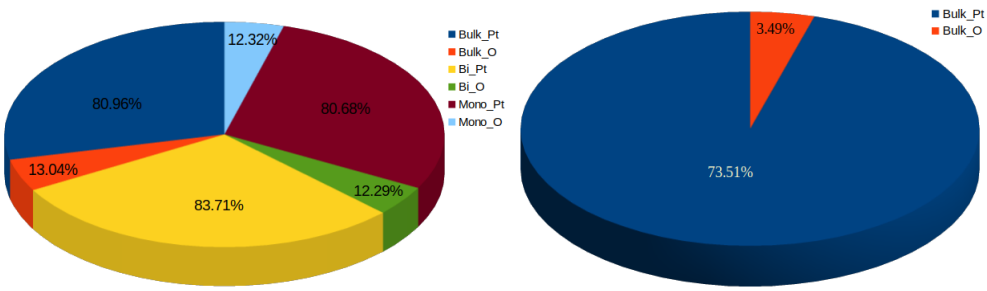


Figure 4.9: Contribution ratio of phonon to lattice thermal conductivity, left is in-plane and right is out-of-plane for bulk and monolayer α-PtO_2 as function of frequency. (Recall there is no contribution in out-of-plane for monolayer).

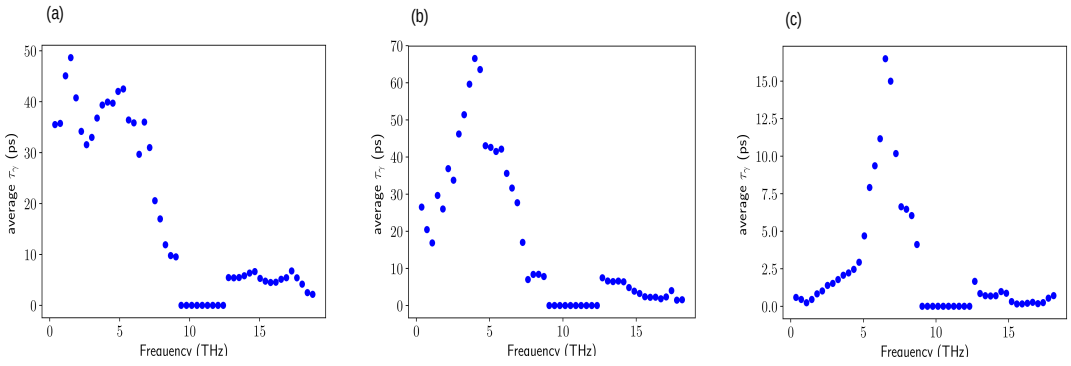


Figure 4.10: Phonon lifetime at 300 K, (a) Bulk, (b) bilayer and (c) monolayer of α-PtO_2 as function of frequency.

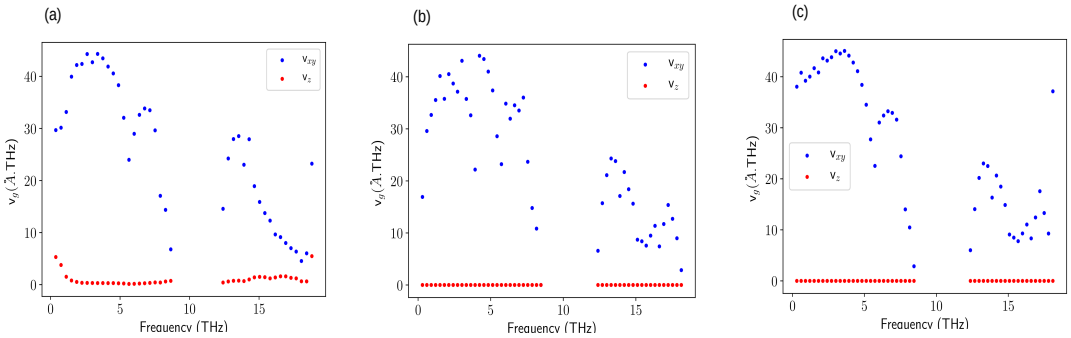


Figure 4.11: Phonon average of directional group velocity, (a) Bulk, (b) bilayer and (c) monolayer of α-PtO$_2$ as function of frequency.

Group velocity

The group velocity depends on the dispersion as shown in Equation (2.5.10). In this work, we calculated the average of directional group velocities for bulk, bilayer and monolayer α-PtO$_2$. The obtained results are shown in Figure 4.11(a-c). In the low frequency range, the in-plane group velocities are higher than out-of-plane, while at high frequency the in-plane and out-of-plane are small compared to the low frequency values. The anisotropy in group velocities has a great impact on the lattice thermal conductivity [129]. The group velocities distributions of the bulk, bilayer and monolayer for in-plane are almost similar, except in out-of-plane which have a value of 6 Å.THz for bulk, while it is 0 Å.THz for bilayer and monolayer. The combined effect of the frequency dependence of the phonon lifetimes and group velocities are consistent with the anisotropy in the thermal conductivity as well as the large contribution to the total thermal conductivity from the low frequency phonons.

4.1.7 Transport properties of α-PtO$_2$

The calculated Seebeck coefficients are presented in Figure 4.12 for bulk, bilayer, and monolayer α-PtO$_2$. We observed that the maximum values of Seebeck coefficient were obtained for holes concentrations, which are 429μV/K at 700 K for bulk and, 573 μV/K at 700 K for bilayer, and 484μV/K at 700 K for the monolayer. From the plot, we can notice that the Seebeck coefficients increase as the temperature increases.
In Figure 4.13, we illustrated the electrical conductivity for the single layer in bulk, bilayer, and monolayer α-PtO$_2$. We found that the highest values at 200 K are 1.23×10^{-4}

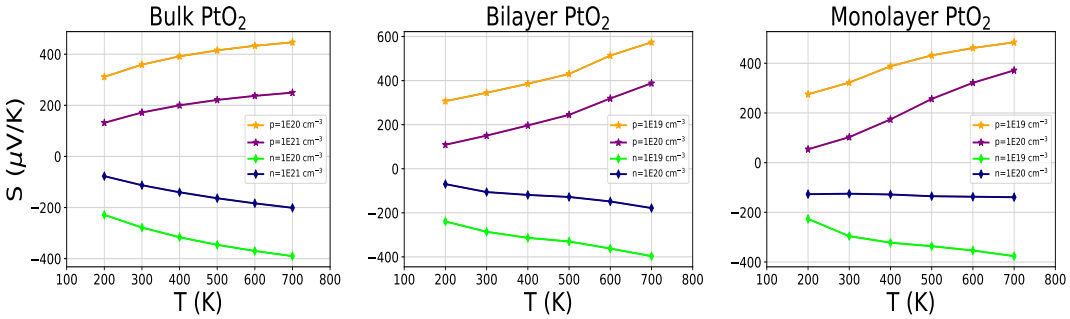


Figure 4.12: Seebeck coefficients of bulk, bilayer and monolayer α-PtO_2.

S/m, 3.9×10^{-4} S/m and 28.2×10^{-4} S/m, respectively, which are attributed to electrons carriers concentration such as 10^{21} cm^{-3} for bulk, and 10^{20} cm^{-3} for bilayer and monolayer.

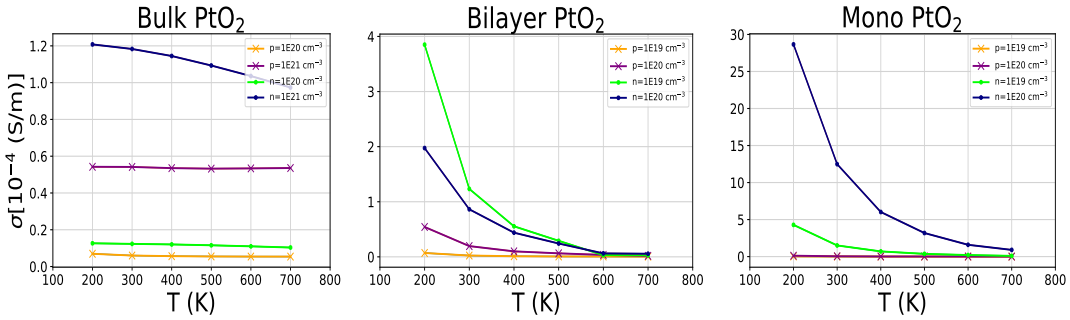


Figure 4.13: Electrical conductivity for a single layer in bulk, bilayer and monolayer α-PtO_2.

On the other hand, we computed the electronic contribution to thermal conductivity for the single layer in bulk, bilayer and monolayer α-PtO_2, to gauge the contribution to the total lattice thermal conductivity from electronic thermal. Figure 4.14 depicts the highest values, at a high temperature of 700 K for bulk while it is at a low temperature of 200 K for bilayer and monolayer. However, the highest values are determined by the majority charge carriers such as electrons. The obtained results show the lowest electronic contribution is obtained the bulk structure followed by the monolayer, and whereas the bilayer α-PtO_2 had the highest values of κ_e which could be attributed to the variation in their band gap size.

The power factor was calculated over a temperature range of from 200 K to 700 K for the single layer in bulk, bilayer, and monolayer. The obtained results are plotted in Figure 4.15, where, we see the difference in the behavior between the bulk, and

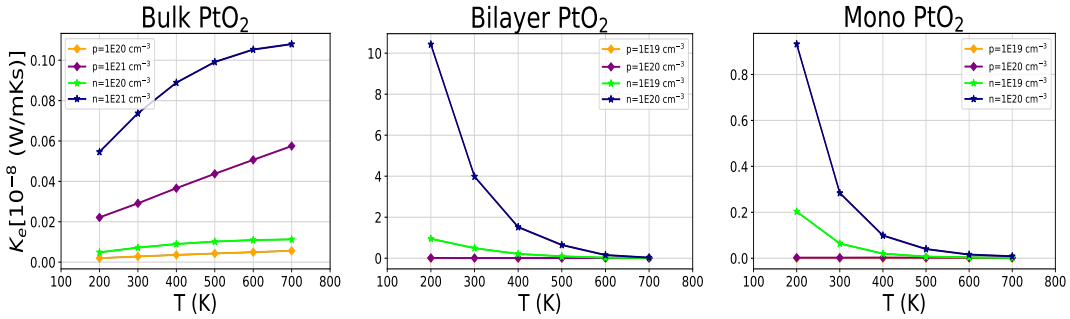


Figure 4.14: Electronic contribution to thermal conductivity for a single layer in bulk, bilayer and monolayer α-PtO_2.

bilayer and monolayer. The highest values of power factor for the all structures are 3.95×10^{-12}WK^{-2}m^{-1} for bulk at 700 K, and 232×10^{-12}WK^{-2}m^{-1} for bilayer at 200 K, while, it is 48×10^{-12}WK^{-2}m^{-1} at 200 K for monolayer.

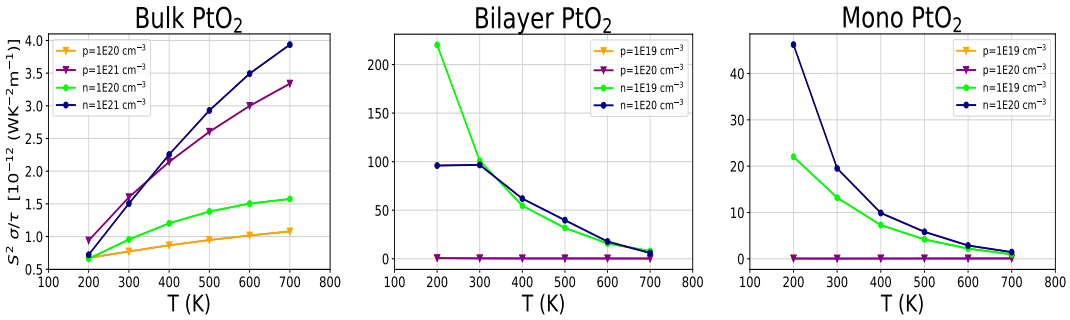


Figure 4.15: Power factor for a single layer in bulk, bilayer and monolayer α-PtO_2.

The dimensionless figure of merit (ZT) was calculated from 200 K to 700 K, and the values for the single layer in bulk, bilayer, and monolayer α-PtO_2 show at 700 K, 400 K, and 300 K, respectively. The obtained ZT values are 0.11 for bulk, 0.62 for bilayer and 0.74 for monolayer, as illustrated in Figure 4.16. The high values of the figure of merit were obtained when the carriers are electrons in all case. As a result, this system provides a broad operational range. These results indicate that at room temperature the monolayer has a high value among the three structures, and is therefore a promising candidates for the thermoelectric power generation applications, with further tuning.

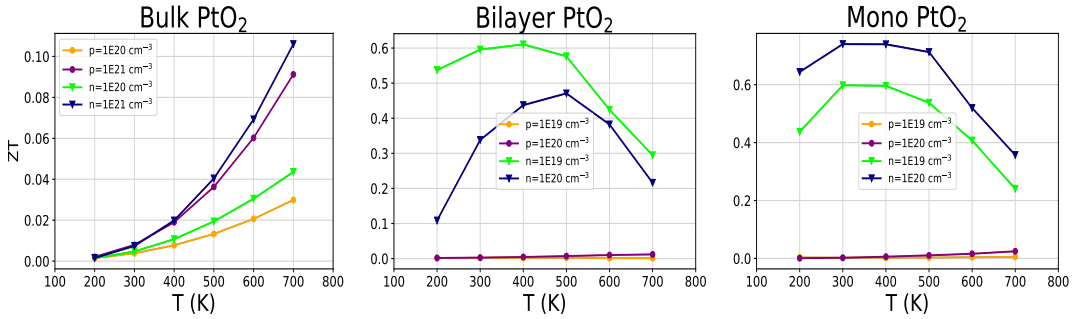


Figure 4.16: Figure of merit for bulk, bilayer and monolayer α-PtO_2.

4.2 Platinum disulfide (PtS_2)

4.2.1 Structural Properties

The fully optimized equilibrium lattice parameters (a, b and V_0) of the bulk, Bilayer and monolayer PtS_2 are listed in Table 4.5. The lattice parameter of bulk PtS_2, $a = 3.55$ Å and $c = 5.03$ Å calculated by using optB86b-vdW are close to $a = 3.54$ Å and $c = 5.04$ Å from the experimental measurements [30, 38, 39]. The obtained lattice parameters for the bilayer are similar to the bulk and monolayer. The monolayer lattice parameter is in agreement with the ones from previous studies. Note that for the PBE bulk results, the lattice parameter c of the bulk, perpendicular to the layers, is relatively larger compared to the experimental values, while the optB86b-vdW value is in good agreement. On the other hand, we set $c = 15\mathring{A}$ as a vacuum layer for bilayer and monolayer which is make the vad der Waal's force between the layers to be weak. We believe that it is due to the fact that The optB86b-vdW takes into consideration the long-range interactions which are not captured by the PBE. The investigation of the phase stabilities for bulk, bilayer and monolayer, were done using the cohesive and formation energies as defined in Chapter 3, using Equation (3.2.1) and (3.2.2), respectively. In Table 4.9, we listed the cohesive and formation energies per atom for bulk, bilayer and monolayer, and compared with available previous studies. Our calculated cohesive and formation energies are negative, which suggest that the bulk, bilayer and monolayer PtS_2 are energetically stable. The bulk, bilayer and monolayer cohesive and formation energies per atom, respectively, are similar for each approximation, which is consistent with the understanding that the inter-layer bonding is weak and its contribution to the total energy is relatively small.

Table 4.5: Calculated, experimental and theoretical optimized lattice constants of bulk bilayer and monolayer PtS_2, cohesive (E_{coh}) and formation formation energies per atom, and inter-layer distance.

		a (Å)	c (Å)	V_o (Å^3)	E_{coh} (eV)	E_{form} (eV)
Bulk	PBE	3.51	5.35	56.92	-4.21	-0.34
	optB86b-vdW	3.55	5.03	54.87	-3.60	-0.45
	Exp[30]	3.54	5.04	54.79	–	–
	Exp[38]	3.54	5.04	54.78	–	–
	Exp[39]	3.54	5.04	54.76	–	–
Bilayer	PBE	3.55	15	–	-4.22	-0.35
	optB86b-vdW	3.54	15	–	-3.43	-2.04
Monolayer	PBE	3.58	15	–	-4.23	-0.36
	optB86b-vdW	3.58	15	–	-3.48	-2.09
	Previous work[130]	3.57	–	–	–	–
	Previous work[41]	3.58	–	–	–	–
	Previous work[42]	3.52	–	–	–	–
	Previous work[123]	3.57	–	–	–	-0.33

4.2.2 Mechanical Stability

In this section, we investigated the mechanical stability for bulk, bilayer and monolayer PtS_2. The elastic constants presented in Table 4.6, fulfil the Born stability criteria [102] see section (3.3.1), which indicate that bulk, bilayer and monolayer PtS_2 are mechanically stable. The Young's moduli and Poisson's ratio for PtS_2 were obtained for bulk, bilayer and monolayer are represented in Table 4.7. We observed that Young's moduli increase with the increase of the number of layers, indicative of increased resistance to deformation under the application of opposing forces as the number of layers are increased. The results agree with previous study for monolayer [41]. In Table 4.7, we presented the obtained Young's moduli (Y) and Poisson's ratio (ν) for bulk, bilayer and monolayer PtS_2 which consistent with available previous study [41]. The values of the Young's moduli in Table 4.7 show that the bilayer can withstand deformation more than the monolayer and the bulk.

Table 4.6: Elastic constants (C_{ij} (GPa)), for bulk, bilayer and monolayer PtS_2.

		C_{11}	C_{12}	C_{13}	C_{14}	C_{33}	C_{66}
Bulk	optB86b-vdW	130.43	62.52	23.41	16.99	11.46	33.96
Bilayer	PBE	122.22	38.12	–	–	–	–
Monolayer	PBE	81.86	24.25	–	–	–	–
Monolayer	Other work[41]	91.82	32.10	–	–	–	–

Table 4.7: The obtained Bulk moduli (B) Shear moduli (G),Young's moduli (Y) and Poisson's ratio (ν) in GPa, for bulk, bilayer and monolayer, and the other theoretical study.

		B	Y	G	ν
Bulk	optB86b-vdW	31.84	55.85	23.12	0.21
Bilayer	PBE	–	110.33	–	0.31
Monolayer	PBE	–	74.67	–	0.29
Monolayer	Other work[41]	–	80.59	–	0.27

4.2.3 Dynamical Stability

For phonon dispersion calculations, we used optB86-vdW approximation for bulk while PBE approximation for bilayer and monolayer, since they have a best lattice parameters compare to experimental and previous study. The phonon dispersion relations were calculated along with several high symmetry directions. Figure 4.17(a-c) show the phonon dispersion band structure and Figure 4.18(a-c) show the phonon dispersion density of states, relations of PtS_2 bulk, bilayer and monolayer, respectively, calculated at the equilibrium configuration with the PHONOPY package [109]. The phonon frequencies are positive throughout the Brillouin zone, which suggests that the bulk, bilayer and monolayer PtS_2 are dynamically stable. The phonon frequencies are in the range of $0 - 11.7$ THz for bulk and $0 - 10.57$ THz for bilayer and $0 - 10.47$ THz for the monolayer, respectively. The reducing in the frequency range for the monolayer is possibly due to the reducing in a number of atomic bonds in the bilayer and monolayer compared to the bulk. The highest frequency of the acoustic modes, defined here as the acoustic cut-off, are approximately 6 THz for both bulk, bilayer and monolayer. Note, the bilayer phonon band structure is dense compared to the bulk and monolayer, which is the same as bilayer PtO_2. In Figure 4.11(a-c), we plot the total and partial density of states for bulk, bilayer and monolayer, respectively. It is proved, that the Pt atom dominates in the low frequency acoustic region, and the S atom contributes more to the high frequency optical mode region.

4.2.4 Electronic structure properties

The electronic structure investigation is presented in this section for the bulk, bilayer and monolayer PtS_2. In Figure 4.19(a-c), we plotted the band structure of the bulk, bilayer and the monolayer PtS_2, respectively. Bulk PtS_2 is an indirect band gap of

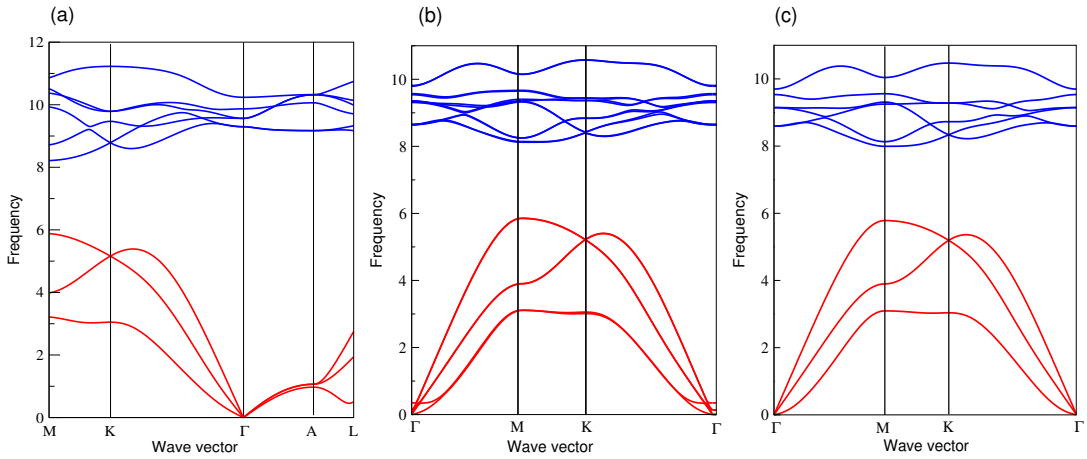


Figure 4.17: The band structure of phonon dispersion for PtS_2. (a) Bulk (b) Bilayer (c) Monolayer.

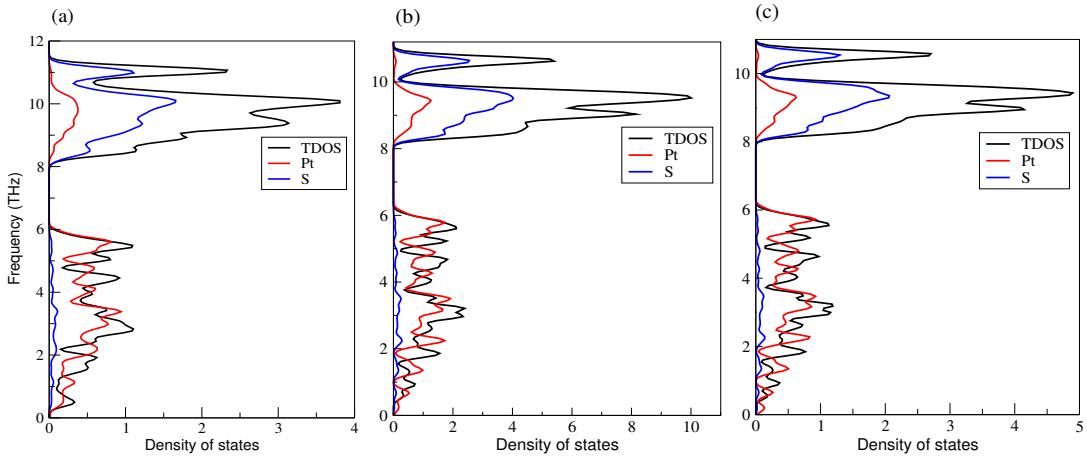


Figure 4.18: TDOS and atomic contributions to acoustic and optical modes of phonon dispersion for PtS_2. (a) Bulk (b) Bilayer (c) Monolayer.

value 0.81 eV, with a maximum of the valence band at Γ point and the minimum of the conduction band at K point. For bilayer and monolayer PtS_2, the maximum of the valence is between the K and Γ points, while the minimum of the conduction band lies between Γ and M points, indicating an indirect band gap for bulk, bilayer and monolayer. In Figures 4.20(a-c), we also plotted the total and partial density of states (TDOS and PDOS) for each atom of bulk, bilayer and monolayer PtS_2, respectively. S(p) has the largest contribution at the top of the valence band followed by Pt(d), for bulk, bilayer and monolayer. In the conduction band, orbital hybridization between the Pt(d) and the S(p) states occurs for bulk, bilayer and monolayer. The dense of bilayer band structure is similar to the bilayer of PtO_2. To investigate the intrinsic

Table 4.8: The calculated band gaps values compared to the experimental and theoretical (in eV) of PtS_2.

	optB86-vdW	PBE	GW_0	Exp.	Other calculations
Bulk	0.81	1.06	1.10	0.87[44], 0.95[131], 0.7[132]	0.48[133],1.2[26],0.73[130]
Bilayer	1.13	1.26	3.78	—	—
Monolayer	1.67	1.80	3.90, 3.14[123]	1.6[133]	1.81[130],1.76 [41],1.94[40], 1.78[134],1.69[42, 123],1.80[135]

band gap we used many approximations namely the optB86b-vdW, PBE and GW_0. In the calculations involving post DFT approximations, we used the optimized lattice parameters from the optB86b-vdW geometric optimisation in the case of bulk PtS_2 and the values for the PBE calculation for the bilayer and monolayer. In Table 4.8, we summarise the computed values with previous studies and experimental results included for comparison. The measured band gaps of this material vary from 0.7 to 0.95 eV, a relatively wide range of values. We observed that the optB86b-vdW approximation gives value within the range of the reported experimental results, while PBE, surprisingly, gives a value above the experimental range. Such unusual behaviour, where GGA DFT overestimates the band gap of transition metal dichalcogenides has also been reported in previous studies [136]. Note that all the DFT gap energies are approximate fundamental gap energies [137], while the experimental values are optical gap values. Direct comparisons are strictly not justified, but it is a common practice in the literature to compare these values. Experimental band gap values for the bulk PtS_2 have been reported by a number of groups: F. Parsapour et al. reported a band gap of 0.87 eV using optical spectroscopy [44]; H. Tributsch and O. Gorochov measured a band gap of 0.95 eV, by means of photoelectrochemical mechanisms [131]; and diffuse-reflectance measurements by F. Hulliger give a band gap of 0.7 eV [132]. The band gap of the

bulk PtS_2 has also been obtained by many authors: Y. Zhao et al. used the optB86b-vdW to predict a band gap of 0.48 eV [133]; a band gap of 1.2 eV was obtained by G. Guo and W. Liang [26] using the linear muffin-tin orbital method combined with the atomic sphere approximation method [138], and the PBE calculations by H.L. Zhuang and R.G. Hennig give a 0.73 eV band gap [130]. The only experimental band gap of the monolayer PtS_2 was reported by Y. Zhao et al [133]. They obtained, using the Fourier-transform infra red spectrometry, a band gap of 1.6 eV. Theoretical monolayer gap values have also been reported. Band gaps of 1.76 and 1.94 eV were predicted by J. Du et al. [41] using the PBE, with the spin-orbit coupling included; and S. Ahmed [40] using the PBE, respectively. P. Miró et al. [134] used the dispersion corrected PBE exchange-correlation functional (PBE-BJ-D3) [69, 139] to obtain a band gap of 1.78 eV, whereas the local density approximation calculations by Z. Huang give an estimation of 1.69 eV [42]. The band gap value of bilayer is found to be 1.13 and 1.26 eV, by using optB86b-vdW and PBE approximations, respectively. The difference between our band gap results which we computed with the optB86b-vdW and PBE approximations and the results of other calculations of 0.48 eV using optB86b-vdW approximation [133] and 0.73 eV using PBE approximation [130] for bulk PtS_2, for monolayer the other calculations are 1.76 using PBE [41] and 1.78 eV using PBE [69, 139], which were performed with the same approximations. Our calculated values are more much close to experimental values. May the reason is can come from differences between DFT implementations and input variables including lattice parameters, k-points and energy cut-offs, after convergence test for all. The calculated band gap values for bulk, bilayer and monolayer were found to be suitable for photovoltaic

4.2.5 Optical properties

For the optical properties, the imaginary and real parts of the dielectric functions were calculate by solving the BSE approximation in conjunction with the GW since the later usually gives a good approximation of the fundamental band gap. Figure 4.21(a) and (b) illustrate the imaginary part and real part of dielectric functions for bulk, and a single layer of bilayer and a monolayer. The absorbance of a single layer in bulk, a single layer of a bilayer and a monolayer PtS_2 was plotted in Figure 4.21(c). The maximum absorbance for in-plane polarisation for a monolayer is $\approx$ 13.15% at 2.51 eV, for bilayer $\approx$7.64% at 1.83 eV and $\approx$ 2.00% at 2.90 eV for bulk. For out-of-plane

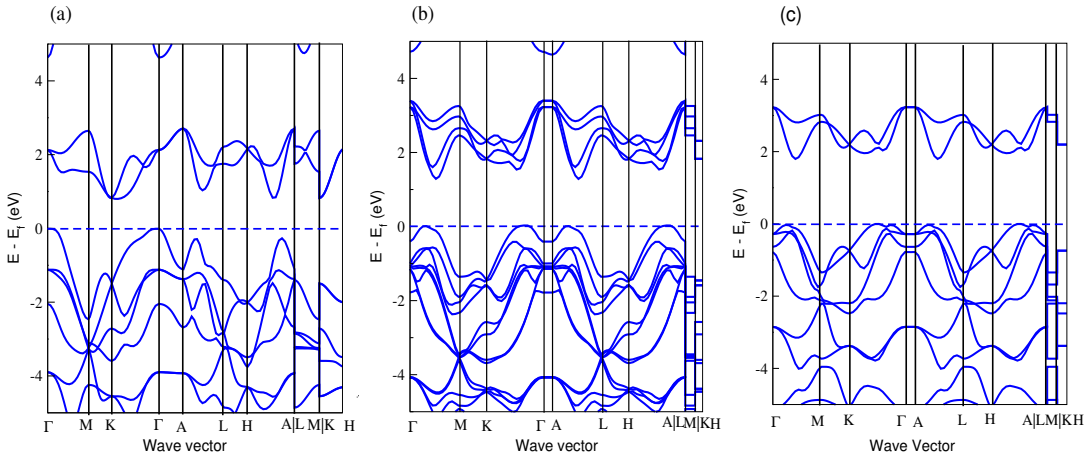


Figure 4.19: Bulk, bilayer and monolayer PtS_2 calculated electronic structure using optB86b-vdW for bulk and PBE for bilayer and monolayer. (a) Bulk, (b) bilayer and (c) monolayer. Along high symmetry directions.

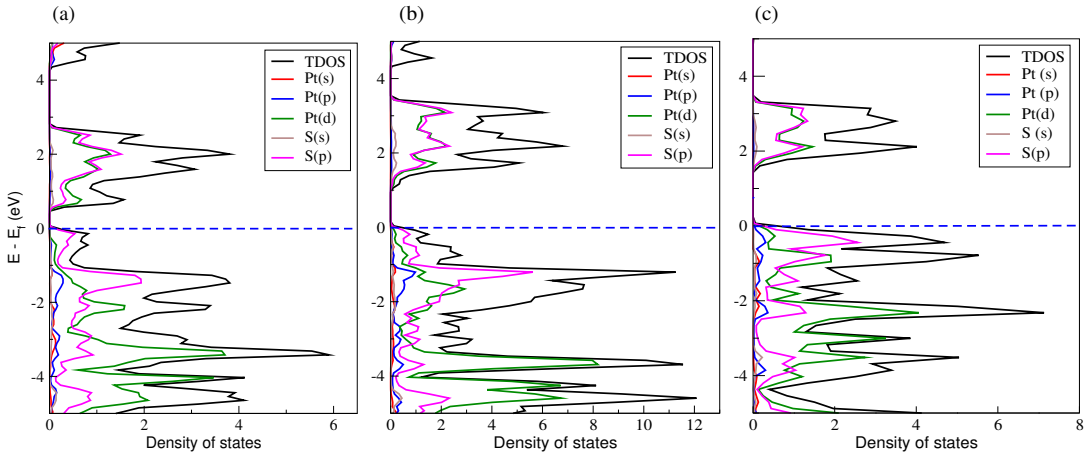


Figure 4.20: Bulk, bilayer and monolayer PtS_2 calculated TDOS and PDOS for each atom and orbital using optB86-vdW for bulk and PBE for bilayer and monolayer. (a) Bulk, (b) bilayer and (c) monolayer.

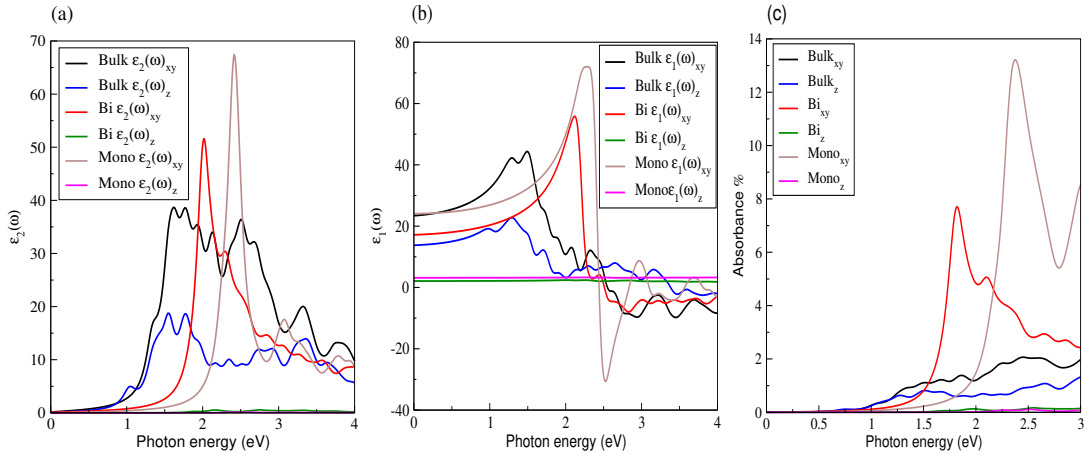


Figure 4.21: GW_0 BSE results (a) imaginary part $\varepsilon_2(\omega)$, (b) real part $\varepsilon_1(\omega)$ of dielectric function and (c) absorbance for bulk, bilayer and monolayer of PtS_2.

polarisation, the maximum absorbance is $\approx 0.09\%$ at 2.6 eV for monolayer, $\approx 0.15\%$ at 2.54 eV and 0.9% at 3 eV for bulk. The absorbance of a monolayer is substantially higher than the absorbance of bulk. This is consistent with results for graphene and MoS_2 [115, 116], where the monolayer absorbance is higher than the absorbance of bulk. The optical band gap was estimated by fitting the BSE optical absorption with the Tauc plot [117]. The BSE approximations are expected to give a good estimation of the optical properties. For the bulk PtS_2, the optical band gap for the in-plane and out-of-plane polarisations are 1.09 and 1.36 eV, respectively. The difference between the two values shows significant optical anisotropy. The value for in-plane polarisation band gap is in accordance with the experimental value. The in-plane and out-of-plane polarisation values of the bilayer are 1.61 and 1.73 eV, respectively. For the monolayer, optical band gaps of 1.95 and 2.30 eV were predicted for the in-plane and out-plane polarisation, respectively. The in-plane optical band gap is once again consistent with the experimental values as given in Table 4.9. The obtained results for bulk and bilayer make them candidates for photovoltaic applications [126].

4.2.6 Lattice thermal conductivity

Figure 4.22 (a) and (b) plots the lattice thermal conductivity dependence of the temperature and frequency for a single layer in bulk, bilayer and a monolayer. As demonstrated in Figure 4.22(a), the average in-plane lattice thermal conductivity for a single layer at 300 K is 2.30×10^{-8}, 1.16×10^{-8} and 0.15×10^{-8} $Wm^{-1}K^{-1}$ for bulk, bilayer and mono-

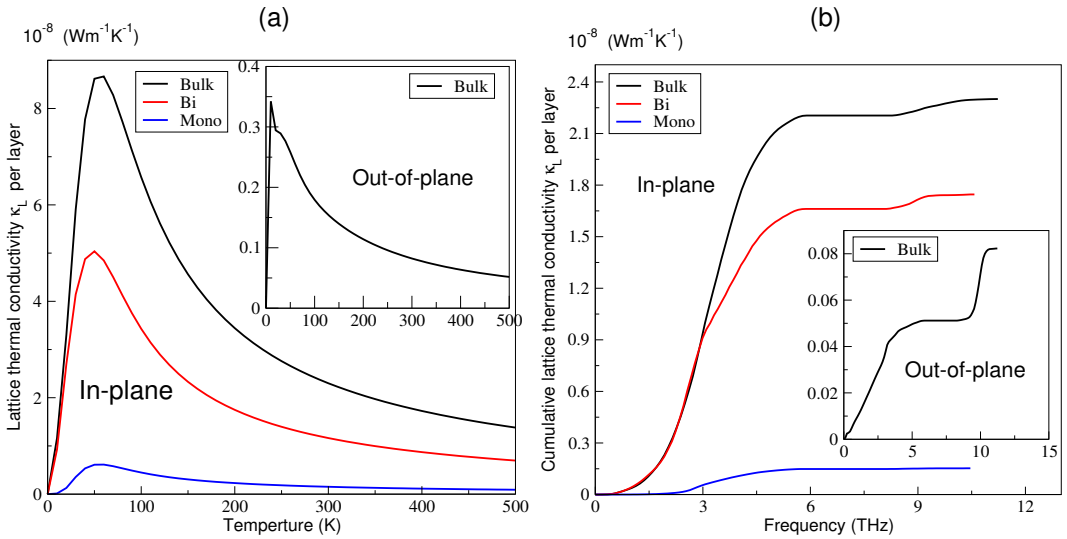


Figure 4.22: Lattice thermal conductivity per layer, (a) lattice thermal conductivity against temperature, (b) cumulative lattice thermal conductivity against frequency.

layer, respectively. The out-of-plane thermal conductivity is 0.08×10^{-8} $Wm^{-1}K^{-1}$ for a single layer of the bulk, whereas it is zero for the monolayer and bilayer. The in-plane lattice thermal conductivity for a monolayer is ∼7% and ∼49.6% of that of a single layer in bulk and bilayer, respectively. This is a significant decrease and points to a possible technique for decreasing lattice thermal conductivity by decreasing the thickness to a few layers. Further, the highest in-plane value of lattice thermal conductivity found to be in the low-temperature range with 8.66×10^{-8} $Wm^{-1}K^{-1}$ at 60 K, 5.04×10^{-8} $Wm^{-1}K^{-1}$ at 50 K and 0.61×10^{-8} $Wm^{-1}K^{-1}$ at 60 K for a single layer in bulk and bilayer, and a monolayer, respectively. The highest out-of-plane thermal conductivity for a single layer in bulk is 0.34×10^{-8} $Wm^{-1}K^{-1}$ at 10 K. We observe that the lattice thermal conductivity is highly anisotropic, with the in-plane thermal conductivity much higher than the out-of-plane thermal conductivity for all bulk, bilayer and monolayer.

Furthermore, we calculated the directional projected density of states for each atom as a function of frequency. Figure 4.23 shows the in-plane and out-of-plane contributions, left and right, respectively, which are along [100] and [001]. The results of directional projected density of states look like phonon density of states, but here we have directional contributions. The same behavior of the directional projected for PtO_2. To perceive the contribution ratio of phonon to lattice thermal conductivity for bulk, bilayer and monolayer PtS_2, we examine the contribution of acoustic and optical phonons branches mode. We obtained that the in-plane acoustic mode total contribution is

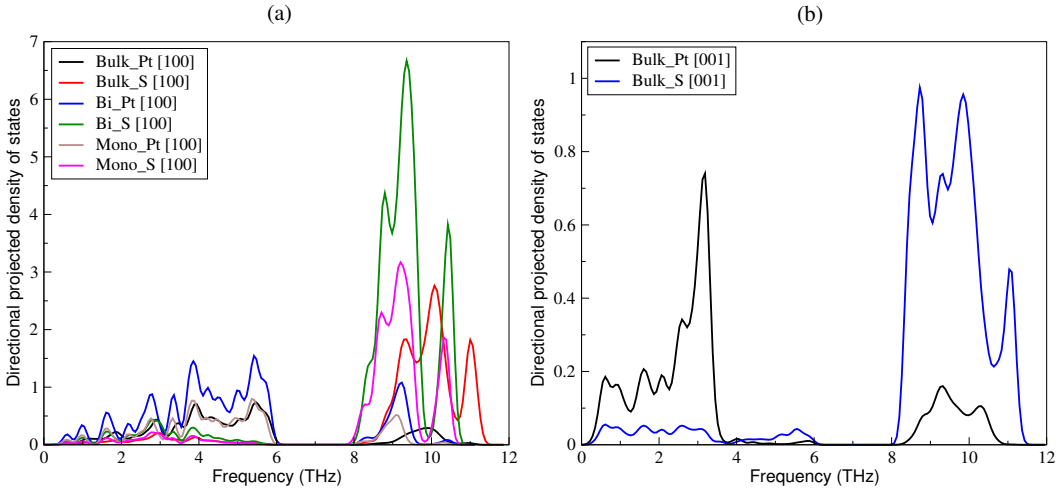


Figure 4.23: Directional projected density of states, left is in-plane and right is out-of-plane for bulk, bilayer and monolayer PtS_2 as function of frequency.

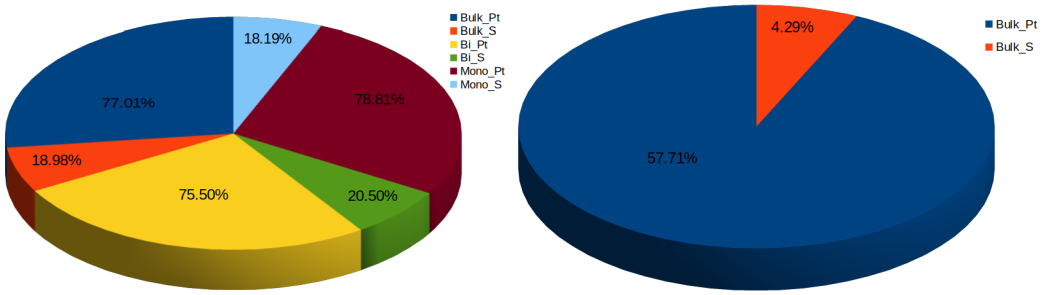


Figure 4.24: Contribution ratio of phonon to lattice thermal conductivity, left is in-plane and right is out-of-plane for bulk and monolayer PtS_2 as function of frequency. (Recall there is no contribution in out-of-plane for monolayer).

96.23%, 96.42% and 97.12% for bulk, bilayer and monolayer PtS_2 respectively. While the out-of-plane 77.01% for bulk, and 0% for bilayer and monolayer. The contributions of phonon to lattice thermal conductivity per atoms are illustrated in Figure 4.24 (left and right), for bulk, bilayer and monolayer. Through Figure 4.24, we can note that the ratio of contribution is almost the same in in-plane, for bulk, bilayer and monolayer. This is in clear contrast to the conventional understanding, especially in the out-of-plane direction, that the acoustic modes dominate thermal conductivity [127].

Phonon lifetime

In this section, we define the phonon lifetime, which is the time between events phonon-phonon scattering, which is calculated by third-order force constants [90, 95]. Figure

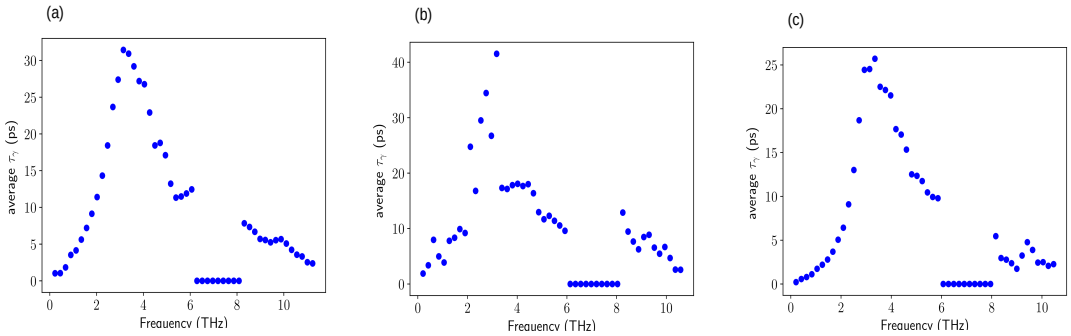


Figure 4.25: Phonon lifetime against frequency at 300 K. (a) Bulk, (b) bilayer and (c) monolayer.

4.25(a-c) shows how the bulk, bilayer and monolayer PtS_2 phonon lifetime depends on frequency, at 300 K. The highest peak for phonon lifetime is located in acoustic mode, and while the lowest peak for phonon lifetime is located in optical mode for all structures. This is in accordance with a slightly strong scattering in the high frequency optical phonon modes. The phonon lifetime distribution of acoustic and optical phonon mode can be used to differentiate the phonon lifetime contributions to the total lattice thermal conductivity [128].

Group velocity

The group velocity depends on the dispersion as plotted in Equation (2.5.10). In this study, we computed the average of directional group velocities for bulk, bilayer and monolayer PtS_2. The calculated results are depicted in Figure 4.26(a-c). In the low frequency range, the in-plane group velocities are higher than out-of-plane, while at high frequency the in-plane and out-of-plane are small compared to the low frequency values. The anisotropy in group velocities have a great impact on the lattice thermal conductivity [129]. The group velocities distributions are almost identical for the three structures in the in-plane direction, but in the out-of-plane direction, the bulk has a value of 10 Å.THZ while the other remain at 0 Å.THz. The combined effect of the frequency dependence of the phonon lifetimes and group velocities are consistent with the anisotropy in the thermal conductivity as well as the large contribution to the total thermal conductivity form the low frequency phonons.

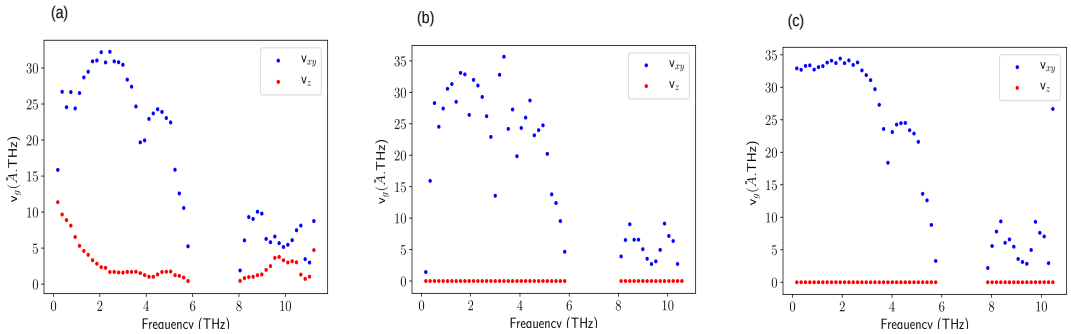


Figure 4.26: Average directional phonon group velocities against frequency. (a) Bulk, (b) bilayer and (c) monolayer.

4.2.7 Transport properties of PtS_2

The Seebeck coefficients were calculated and presented in Figure 4.27 for bulk, bilayer and monolayer PtS_2, at a range of temperature between 200 to 500 K. The results predict the highest values of Seebeck coefficient for holes carriers concentrations of 10^{19}cm^{-3}. At 500 K we obtained 294μV/K for bulk, 334 μV/K for bilayer and 410μV/K for monolayer. From the plots, we can observe that the Seebeck coefficients are increasing with the increasing of the temperature.

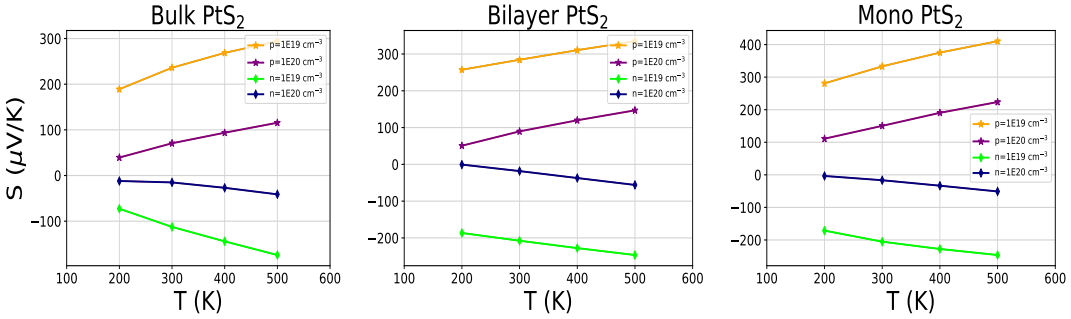


Figure 4.27: Seebeck coefficients of bulk, bilayer and monolayer PtS_2.

The electrical conductivity for the bulk, bilayer and monolayer PtS_2 are depicted in Figure 4.28. We found the maximum values for a single layer at 200 K, are 1.75×10^{-4} S/m for bulk, 7.97×10^{-4} S/m for bilayer and 3.6×10^{-4} S/m for monolayer, which are caused by electrons carriers whose concentration is 10^{20} cm^{-3}. For all concentration of charge carriers, the electrical conductivity decreases with an increase in temperature. This indicates that the electrical conductivity decreases when the temperature is increase due to their inverse relationship, which it is converse to what was noted in

Figure 4.27 for Seebeck coefficient case.

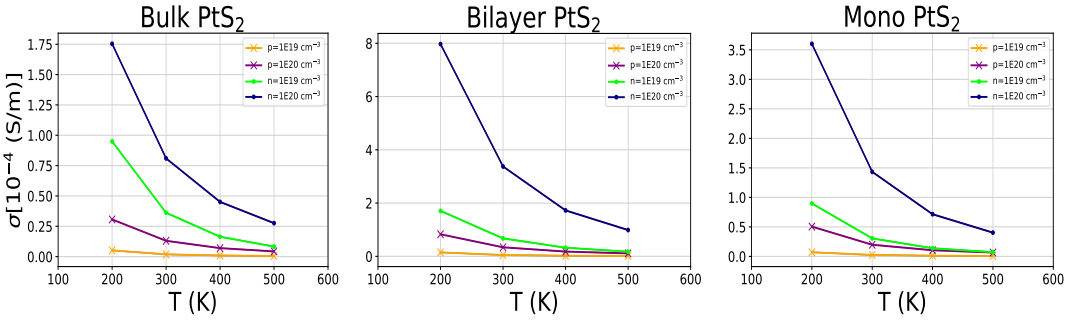


Figure 4.28: Electrical conductivity for a single layer in bulk, bilayer and monolayer PtS_2.

In order to know the contribution to the total thermal conductivity arising from the electronic component, we examined the electronic contribution to the total thermal conductivity. Figure 4.29 depicts the maximum values, at a low temperature of 200 K for a single layer in bulk, bilayer and monolayer, achieve by the majority of electrons carriers concentration of 10^{20}cm^{-3}. The obtained results show the same behaviour occur, from bulk to bilayer and to monolayer structure, with different highest values. Generally, for semiconductors the lattice thermal contribution often dominates the total thermal conductivity, since $\kappa_L \geqslant \kappa_e$.

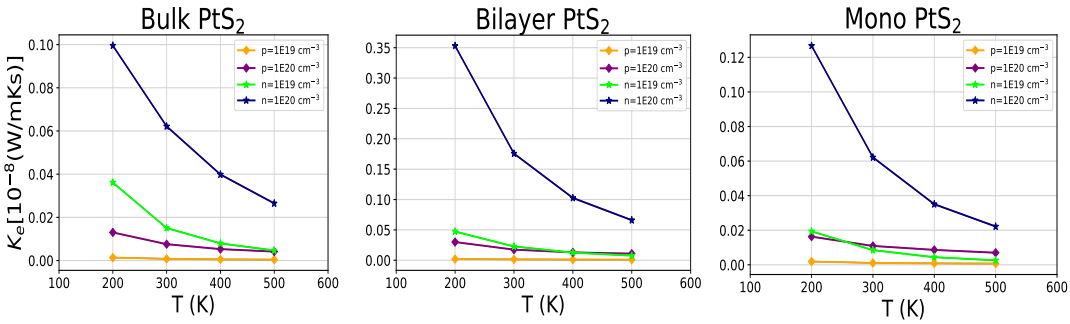


Figure 4.29: Electronic contribution to thermal conductivity coefficients for a single layer in bulk, bilayer and monolayer PtS_2.

Power factor is a parameter used to measure the ability of electric power generation of a material. The power factor was calculated over a temperature range of from 200 to 500 K for a single layer in bulk, bilayer and monolayer. The obtained results are plotted in Figure 4.30. Similarity on the power factor gradient can be observed among the structures. The highest and lowest values of power factor for all structures are obtained from

the electrons carrier concentration of $10^{19}cm^{-3}$ and $10^{20}cm^{-3}$, respectively, around 200 K. The highest charge carriers concentration decreases gradually when the temperature increases, which is opposite to the lowest charge carriers concentration.

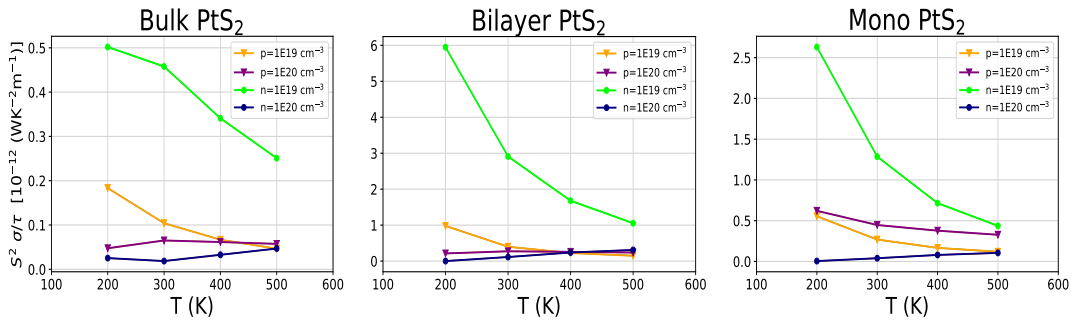


Figure 4.30: Power factor for a single layer in bulk, bilayer and monolayer PtS_2.

The ZT was obtained within the range of from 200 to 500 K. The high value of figure of merit for each of a single layer in bulk, bilayer and monolayer PtS_2 were attained at 200 K, 500 K and 500 K, respectively. Their ZT values are 0.04 for bulk, 0.12 for bilayer and 0.18 for monolayer, as illustrated in Figure 4.31. The maximum values of figure of merit were dominated by electrons carriers concentration of $10^{19}cm^{-3}$, while the lowest values are dominated by electrons carriers concentration of $10^{20}cm^{-3}$, in all cases. The small values of the figure of merit are possibly due to the high values of lattice thermal as provided in the previous section. ZT values are increasing in opposite to increasing the number of layers.

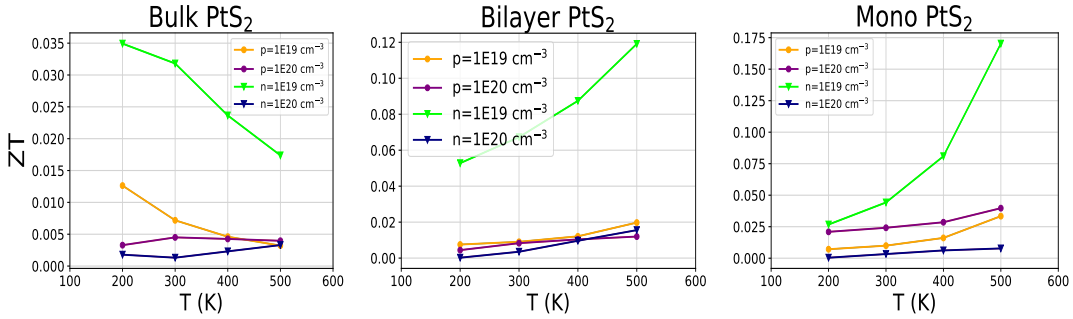


Figure 4.31: Figure of merit for bulk, bilayer and monolayer PtS_2.

4.3 Platinum diselenide ($PtSe_2$)

4.3.1 Structural Properties

The fully optimized equilibrium lattice parameters of bulk, bilayer and monolayer $PtSe_2$, using optB86-vdW and PBE approximations and compared with available experimental and previous study data are listed in Table 4.9. We observed that the calculated results of the lattice parameters using optB86-vdW function agreed to the experimental for bulk and monolayer to the previous study. On the other hand, the obtained lattice parameters for the bilayer are close to the bulk and monolayer. On the other hand, we set $c = 15\mathring{A}$ as a vacuum layer for bilayer and monolayer which is make the vad der Waal's force between the layers to be weak. The investigation of the phase stability done using the cohesive and formation energies as defined in Chapter 3, using Equation (3.2.1) and (3.2.2), respectively. In Table 4.9, we listed the energy and formation energies per atom for bulk, bilayer and monolayer, and compared with available previous studies. The computed cohesive energy and formation energies are negative. Hence, the bulk, bilayer and monolayer $PtSe_2$ are energetically stable. The a and c lattice parameters, the inter-layer structural parameters, show the least variation across the different approximations. The inter-layer spacing, defined by the c lattice parameter, show the most variation. We note that optB86-vdW gives the best equilibrium structural parameters for bulk $PtSe_2$ when compared to the experimental.

Table 4.9: Calculated, experimental and theoretical, optimized lattice constants of bulk, bilayer and monolayer $PtSe_2$, cohesive (E_{coh}) and formation formation energies per atom, and inter-layer distance.

		a (Å)	c (Å)	V_o (Å^3)	E_{coh} (eV)	E_{form} (eV)
Bulk	PBE	3.81	4.87	61.24	-4.20	-0.38
	optB86b-vdW	3.76	4.97	61.11	-4.55	-0.43
	Exp[45, 30]	3.72	5.08	61.15	–	–
	Exp[121]	3.74	5.14	62.54	–	–
Bilayer	PBE	3.76	15	–	-3.95	-0.39
	optB86b-vdW	3.76	15	–	-3.22	-0.31
Monolayer	PBE	3.81	15	–	-3.96	-0.38
	optB86-vdW	3.81	15	–	-3.03	-0.71
	Previous work[130]	3.75	–	–	–	0.11
	Previous work[123]	3.75	–	–	–	-0.36

4.3.2 Mechanical stability

In this section, we examined the mechanical stability of the three $PtSe_2$ structures. The elastic constants listed in Table 4.10, fulfil the Born stability criteria [102] see section (3.3.1), which indicate that bulk, bilayer and monolayer $PtSe_2$ are mechanically stable. The Young's moduli and Poisson's ratio for $PtSe_2$ were obtained for bulk, bilayer and monolayer are represented in Table 4.11. We observed that Young's moduli increases with the increase of the number of layers, indicating the increase of the resistance to deformation under the application of opposing forces as the number of layers are increased. The results agree with previous study [41], for monolayer. We also present the calculated Young's moduli (Y) and Poisson's ratio (ν) for bulk, bilayer and monolayer $PtSe_2$, and bulk moduli and shear moduli for bulk $PtSe_2$, which consistent to an available previous study [41]. The values of the Young's moduli in Table 4.11 shows that the bulk is more resistant to deformation than monolayer and bilayer, also the bilayer more resist than monolayer.

Table 4.10: Elastic constants (C_{ij} (GPa)), for bulk, bilayer and monolayer $PtSe_2$.

		C_{11}	C_{12}	C_{13}	C_{33}	C_{66}
Bulk	optB86b-vdW	197.7	67.89	41.32	40.73	64.91
Bilayer	PBE	76.52	18.19	–	–	–
Monolayer	PBE	65.38	19.37	–	–	–
Monolayer	Other work[41]	73.73.40	26.30	–	–	–

Table 4.11: The obtained Bulk moduli (B) Shear moduli (G),Young's moduli (Y) and Poisson's ratio (ν) in GPa, for bulk, bilayer and monolayer $PtSe_2$, and the other theoretical study.

		B	Y	G	ν
Bulk	optB86b-vdW	66.75	102.97	41.42	0.24
Bilayer	PBE	–	72.19	–	0.24
Monolayer	PBE	–	59.64	–	0.29
Monolayer	Other work[41]	–	64.35	–	0.25

4.3.3 Dynamical stability

The harmonic phonon dispersion relations were computed along with the high symmetry directions. The phonon band structure, total density of states and partial density of

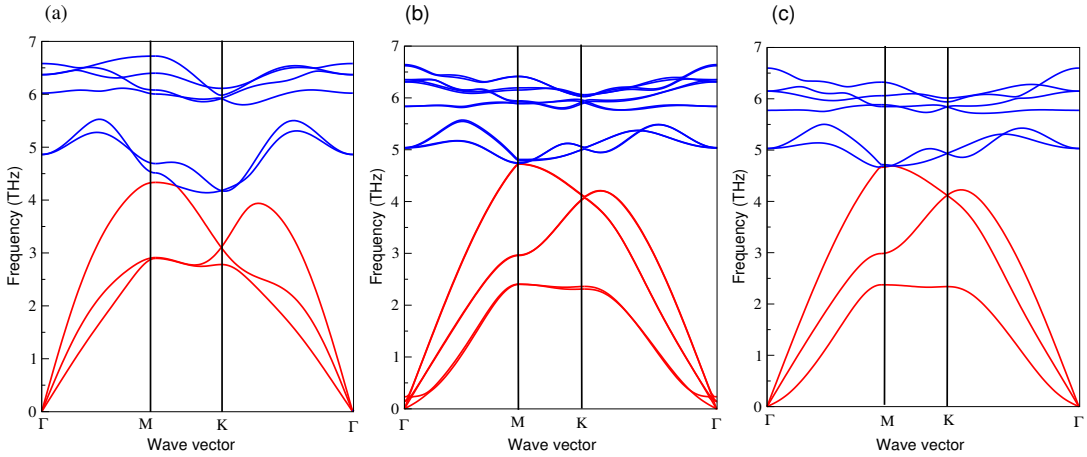


Figure 4.32: The band structure of phonon dispersion for $PtSe_2$. (a) Bulk (b) Bilayer (c) Monolayer.

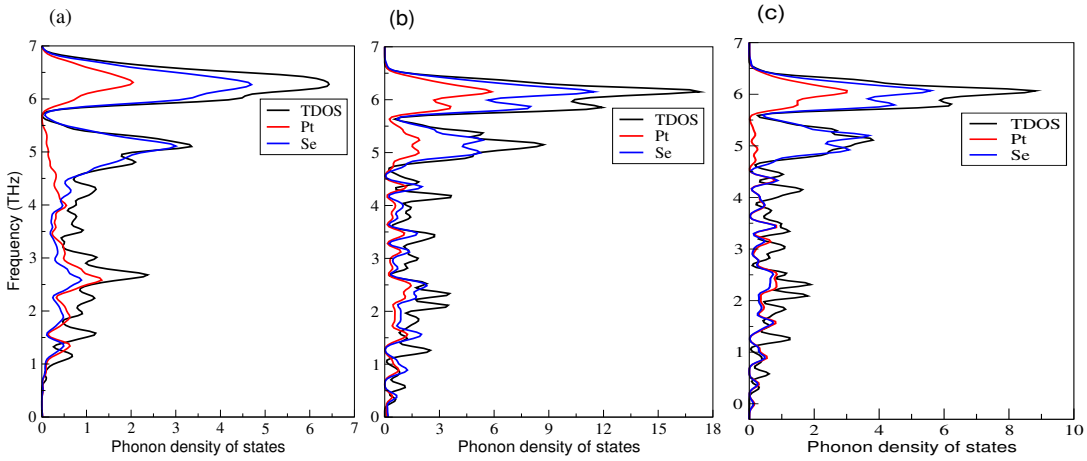


Figure 4.33: TDOS and atomic contributions to acoustic and optical modes of phonon dispersion for $PtSe_2$. (a) Bulk (b) Bilayer (c) Monolayer.

states, for bulk, bilayer and monolayer $PtSe_2$ are presented in Figure 4.32(a-c) and Figure 4.33(a-c), respectively. The phonon partial density of states shows the atomic contribution to the total phonon density. The range of phonon frequencies is between $0 - 6.6$ THz for bulk and monolayer, while for bilayer is $0 - 6.7$ THz. All the phonon frequencies are positive, which indicates that the bulk, bilayer and monolayer of $PtSe_2$ are dynamically stable. The similarity behavior of bilayer $PtSe_2$, was noted for PtO_2 and PtS_2 in the phonon band structure. The total and partial density of states respectively for bulk, bilayer and monolayer are presented in Figure 4.11(a-c). It is evident that the Pt atom controls in the low frequency acoustic region and the Se atom contributes more to the high frequency optical mode region.

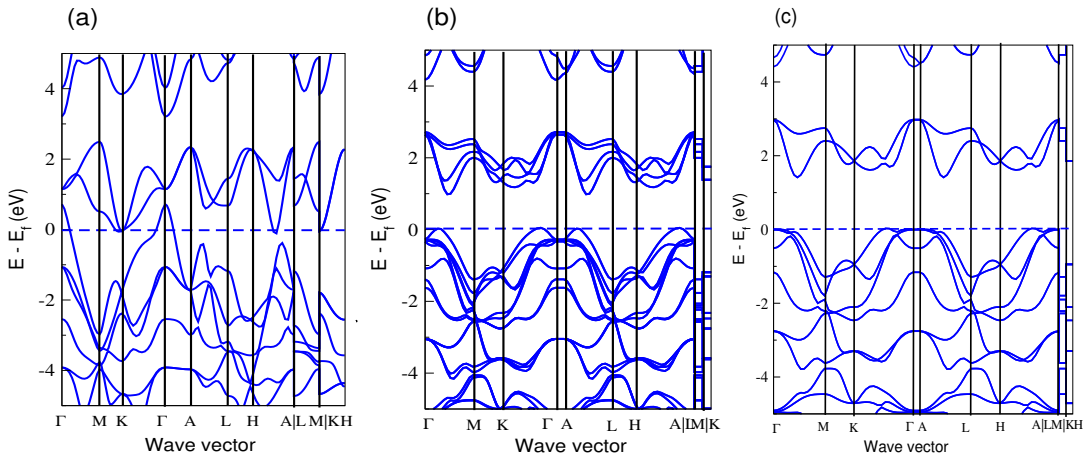


Figure 4.34: Bulk, bilayer and monolayer $PtSe_2$ calculated electronic structure using optB86b-vdW for bulk and PBE for bilayer and monolayer. (a) Bulk, (b) Bilayer (c) Monolayer. Along high symmetry directions.

4.3.4 Electronic structure properties

The electronic band structure, total and partial density of states of the bulk, bilayer and monolayer $PtSe_2$ are shown in Figure 4.34(a-c) and Figure 4.35(a-c), respectively. The electronic structure calculations proved that the bulk phase of both compounds shows is a semi-metal, while the bilayer and monolayer are semiconductor with an indirect band gap. The minima of the conduction are located between Γ and M, while the maxima of the valance are at the A and L points, of the Brillouin zone. Furthermore, we calculated the density of states (total and partial), Figure 4.35(a-c) illustrated the contributions of atoms to the gap edge. The density of states in Figure 4.35(a) confirmed the band structure plot for bulk a semi-metal behaviour. But, the density of states for bilayer and monolayer show that the maximum valence band is mostly do to the Se(p) orbital while the minimum conduction band comes from the hybridisation between the Pt(d) and Se(p) states. Note, the bilayer band structure appears dense as it is in PtO_2 and PtS_2 bilayer. In Table 4.12, we summarised the band gap values for bulk, bilayer and monolayer for $PtSe_2$. Our calculated results agree with the experimental and previous studies in Table 4.12. We find that the band gaps decrease with the increasing number of layers as it was previously reported by Xu M *et al.* [140]. The values of the band gap explain that the bilayer and monolayer suitable to photovoltaic applications.

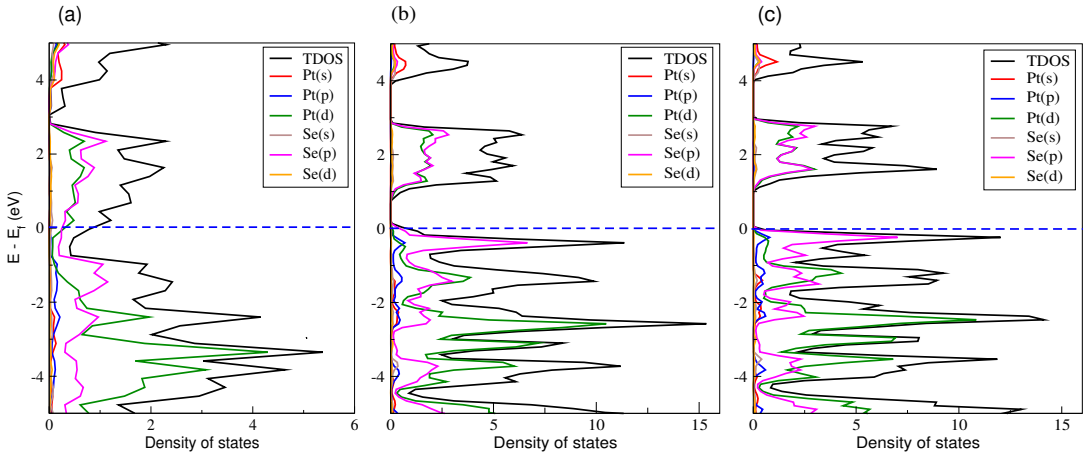


Figure 4.35: Bulk, bilayer and monolayer $PtSe_2$ calculated TDOS and PDOS for each atom and orbital using optB86-vdW for bulk and PBE for bilayer and monolayer. (a) Bulk (b) Bilayer (c) Monolayer.

Table 4.12: The calculated band gaps values compared to the experimental and theoretical (in eV) of $PtSe_2$.

	optB86-vdW	PBE	GW_0	Exp.	Other calculations
Bulk	semimetal	semimetal	–	semimetal[29, 47]	–
Bilayer	0.76	0.93	1.24	∼0.80[48]	0.21[47],0.99[50]
Monolayer	1.25	1.38	3.90, 2.10[130],2.67[123]	1.6[48]	1.20[47],1.22[141] ,1.41[130],1.39[50], 1.29[123],1.25[42],1.40[135],1.18[51]

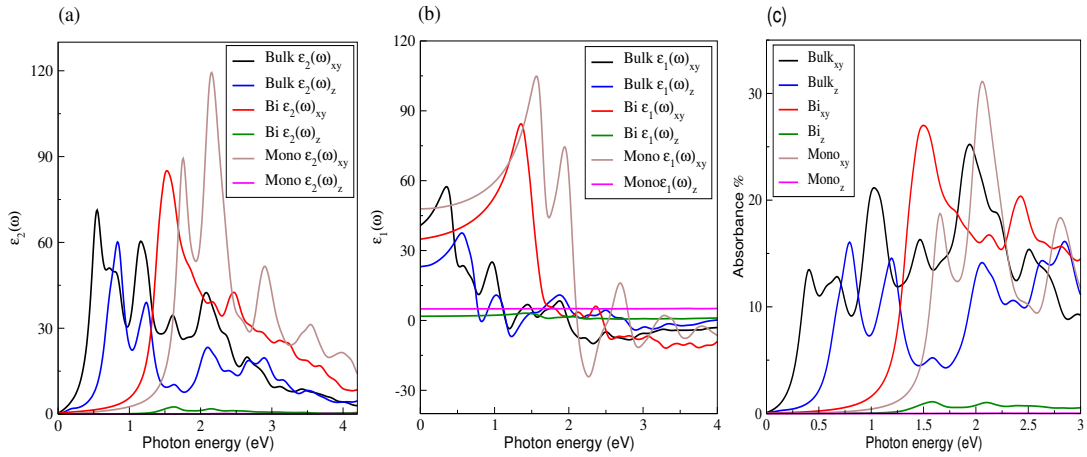


Figure 4.36: GW_0 BSE results (a) imaginary part $\varepsilon_2(\omega)$, (b) real part $\varepsilon_1(\omega)$ of dielectric function and (c) absorbance for bulk, bilayer and monolayer of $PtSe_2$.

4.3.5 Optical properties

Figure 4.36(a-c) presents the calculated imaginary and real parts of the dielectric functions, and the absorbance of bulk, a single layer of the bilayer and a monolayer $PtSe_2$. As we mentioned it in the case of other compounds, these properties are obtained by solving the BSE. The maximum absorbance in in-plane polarization for monolayer is $\approx$ 31.05% at 2.06 eV and for bilayer is $\approx$ 26.89% at 1.51 eV and 25.04% at 1.95 eV for bulk. The absorbance of a monolayer is considerably greater than the absorbance for a bilayer and bulk. This is higher than that of MoS_2, $MoSe_2$ and WS_2 (5−10%) [115, 116], where the single layer absorbance is high in monolayer than bilayer and bulk. Moreover, in the out-of-plane polarisation, the maximum absorbance is $\approx$ 0.09% at 2.60 eV for monolayer and $\approx$ 0.96% at 1.58 eV for bilayer and 16.00% at 0.80 eV for bulk. We used the Tauc plot [117] to calculate the optical band gap. For the bulk $PtSe_2$, the in-plane and out-of-plane optical band gap polarizations are 0.1 and 0.3 eV, respectively. The value for in-plane polarisation gap is higher than a predicted experimental gap. For the monolayer, the optical band gap of 1.43 and 1.64 eV was predicted for the in-plane polarisation and out-of-plane, respectively. The calculated optical band gaps of the in-plane and out-of-plane polarization, for the bilayer are 1.10 and 1.25 eV, respectively. Therefore, the obtained values of the bilayer could also be used for photovoltaic solar cells applications, [142, 143, 144].

4.3.6 Lattice thermal conductivity

The lattice thermal conductivity against temperature and frequency were shown in Figure 4.37(a) and (b) respectively, for a single layer of bulk, bilayer and monolayer $PtSe_2$ structure. The average lattice thermal conductivity at300 K for a single layer in bulk, bilayer and monolayer is 0.47×10^{-8}, 0.24×10^{-8} and 0.11×10^{-8} $Wm^{-1}K^{-1}$ in-plane direction for a single layer in bulk, bilayer and monolayer respectively, and 0.10×10^{-8} $Wm^{-1}K^{-1}$ out-of-plane for bulk while the out-of-plane for bilayer and monolayer are zero. The lattice thermal conductivity value for a single layer in bulk decreases by about ∼49% of the bilayer and ∼77% of the monolayer, in the in-plane. Further, the high in-plane value of lattice thermal conductivity per single layer was found to be in the low-temperature range is 7.27×10^{-8} $Wm^{-1}K^{-1}$ at 20 K for bulk, and 2.39×10^{-8} $Wm^{-1}K^{-1}$ at 20 K for bilayer and 2.27×10^{-8} $Wm^{-1}K^{-1}$ at 30 K for monolayer. The high out-of-plane is 1.28×10^{-8} $Wm^{-1}K^{-1}$ at 10 K for single layer bulk. The lattice

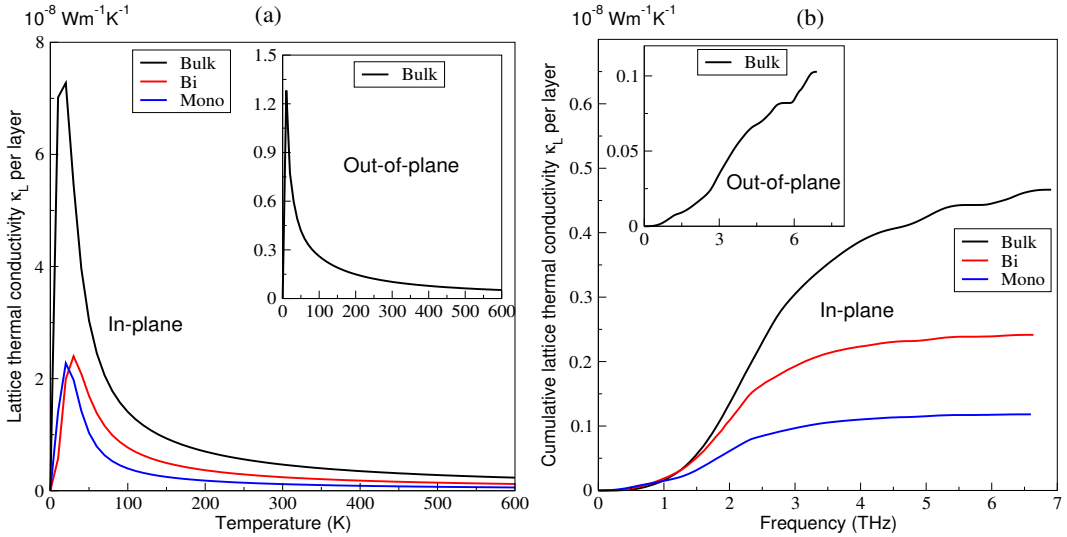


Figure 4.37: Lattice thermal conductivity per layer for $PtSe_2$, (a) lattice thermal conductivity vs temperature, (b) cumulative lattice thermal conductivity vs frequency.

thermal conductivity against frequency at 300 K is plotted in Figure 4.7(b), and its cumulative lattice thermal conductivity as a function of the frequency of single layer for bulk, bilayer and monolayer. We observed that the lattice thermal conductivity is highly anisotropic, with the thermal conductivity in-plane of the layers being much higher than in the out-of-plane direction for two cases bulk, bilayer and monolayer. The all lattice thermal conductivity values for a single layer in bulk, bilayer and monolayer $PtSe_2$, are suits for thermoelectric application

Furthermore, we calculated the directional projected density of states for each atom as a function of frequency. Figure 4.38 shows the in-plane and out-of-plane contributions, left and right, respectively, which are along [100] and [001]. The results of directional projected density of states look like phonon density of states, but here we have directional contributions. The Pt and Se atoms contribution to the directional projected density of states look like PtO_2 and PtS_2 compounds. While in out-of-plane just we only have the contribution for bulk. To understand the contribution ratio of phonon to lattice thermal conductivity for bulk, bilayer and monolayer $PtSe_2$, we compute the contribution of acoustic and optical phonons branches mode. The contribution estimated to the thermal conductivity from the acoustic modes at 300 K. We obtained that the in-plane acoustic mode total contribution is 95.12%, 95.39% and 96.58% for bulk, bilayer and monolayer $PtSe_2$ respectively. While the out-of-plane 86.02% for bulk, and 0% for bilayer and monolayer. The contributions of phonon to lattice thermal conductivity per

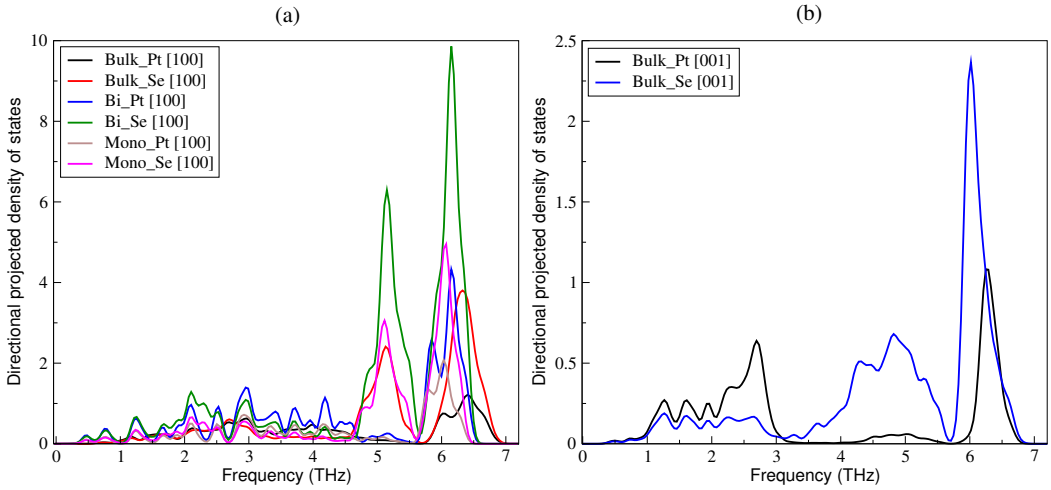


Figure 4.38: Directional projected density of states, left is in-plane and right is out-of-plane for bulk, bilayer and monolayer $PtSe_2$ as function of frequency.

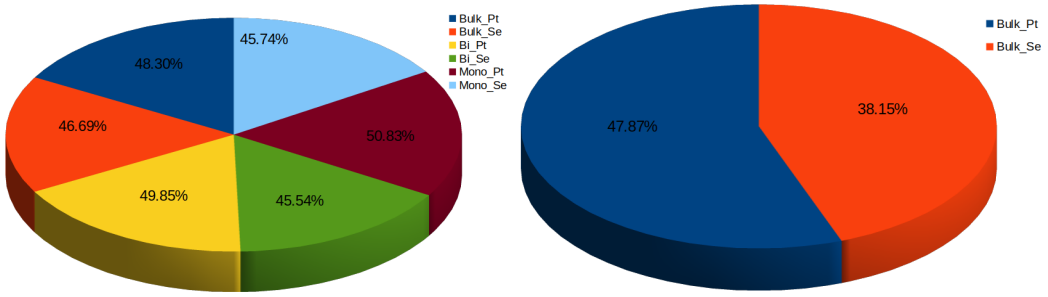


Figure 4.39: Contribution ratio of phonon to lattice thermal conductivity, left is in-plane and right is out-of-plane for bulk and monolayer $PtSe_2$ as function of frequency. (Recall there is no contribution in out-of-plane for monolayer).

atoms are illustrated in Figure 4.39 (left and right), for bulk, bilayer and monolayer. Through Figure 4.39, we can note that the ratio of contribution is almost the same in in-plane, for bulk, bilayer and monolayer. Also in the right, we have out-of-plane, which is for bulk. This is in clear contrast to the conventional understanding, especially in the out-of-plane direction, that the acoustic modes control thermal conductivity [127].

Phonon lifetime

Figure 4.40(a-c) shows how the bulk, bilayer and monolayer $PtSe_2$ phonon lifetime depends on frequency, at 300 K. The highest peak for phonon lifetime is located in acoustic mode, and while the lowest peak for phonon lifetime is located in optical mode for all structures. This is in accordance with a somewhat potent scattering in the high

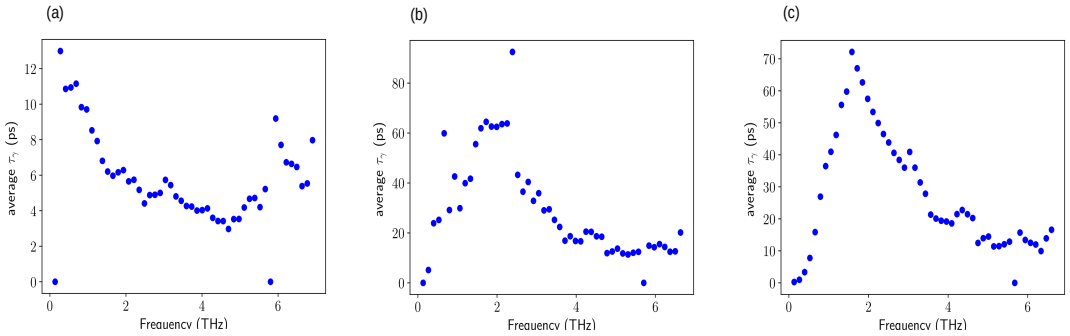


Figure 4.40: Phonon lifetime against frequency at 300 K for $PtSe_2$. (a) Bulk, (b) bilayer and (c) monolayer.

frequency optical phonon modes. To differentiate the phonon lifetime contributions to the total lattice thermal conductivity, one can use the phonon lifetime distribution of acoustic and optical phonon mode [128].

Group velocity

The calculated results are plotted in Figure 4.41(a-c). The in-plane group velocity is higher than out-of-plane in the low frequency range, while at high frequency the in-plane and out-of-plane are small compared to the low frequency values. The anisotropy in group velocity has a big impact on the lattice thermal conductivity [129]. The similarity of the distribution for in-plane group velocities of bulk and monolayer. In contrast, the out-of-plane group velocities is 11 Å.THz for bulk and zero for others. The combined effect of the frequency dependence of the phonon lifetimes and group velocities are consistent with the anisotropy in the thermal conductivity as well as the large contribution to the total thermal conductivity form the low frequency phonons.

4.3.7 Transport properties of $PtSe_2$

In Figure 4.42, we present the calculated Seebeck coefficients for bulk, bilayer and monolayer $PtSe_2$ at range of temperature between 200 K to 600 K. The highest values of Seebeck coefficient were obtained when majority carriers are holes with concentrations of 10^{19}cm^{-3} to be 1013μV/K at 200 K for bulk, and 343μV/K at 600 K for bilayer, while for monolayer it was 376 μV/K at 600 K.

In Figure 4.43, the highest values of the electrical conductivity are found at 200 K for

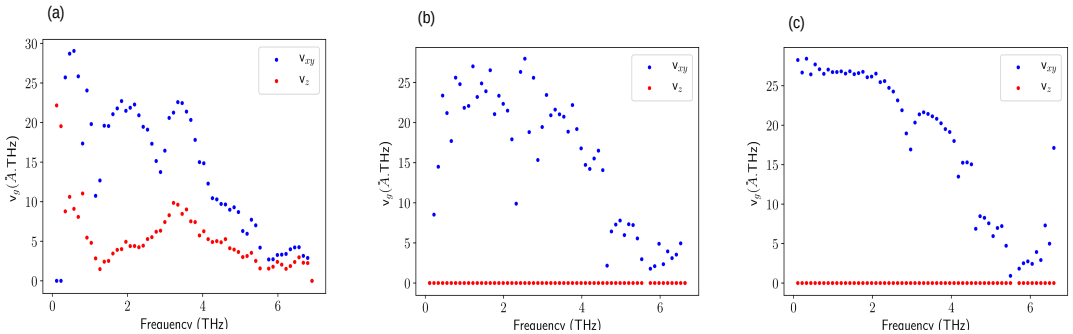


Figure 4.41: Average directional phonon group velocities against frequency for $PtSe_2$. (a) Bulk, (b) bilayer and (c) monolayer.

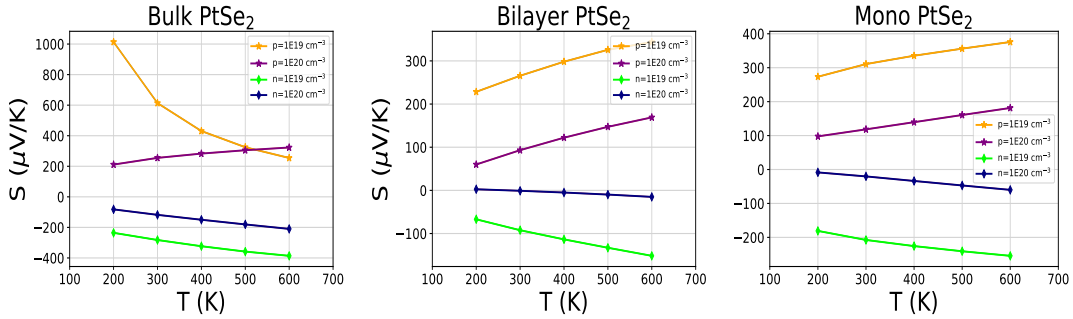


Figure 4.42: Seebeck coefficients of bulk, bilayer and monolayer $PtSe_2$.

all structures. For the bulk, it is 0.53×10^{-4}, 18.07×10^{-4} and 3.42×10^{-4} S/m for the bilayer and monolayer, respectively. These values are achieved when the electrons carriers concentration is 10^{20} cm^{-3}. For all concentration of carriers, the electrical conductivity decreases with an increase in temperature. This explains that the electrical conductivity, whereby an increase in temperature results in a decrease in electrical conductivity due to their inverse relationship, and it is converse to what was noted in Figure 4.42 for the case of Seebeck coefficient.

Figure 4.44 illustrate the computed electronic contribution to thermal conductivity for a single layer in the bulk, bilayer and monolayer $PtSe_2$. The highest κ_e values are achieved at a high temperature of 600 K for bulk, while it is at low temperature (200 K) for both bilayer and monolayer. At 200 K for bulk, bilayer and monolayer are dominated by the majority of electrons carriers concentration of $10^{20}cm^{-3}$, while minimum temperature values, were dominated by the majority hole carriers whose concentration is $10^{19}cm^{-3}$. The calculated results show the same behaviour of electrical contribution Figure 4.43 for bilayer and monolayer structures. Oftenly, in reality, the lattice thermal

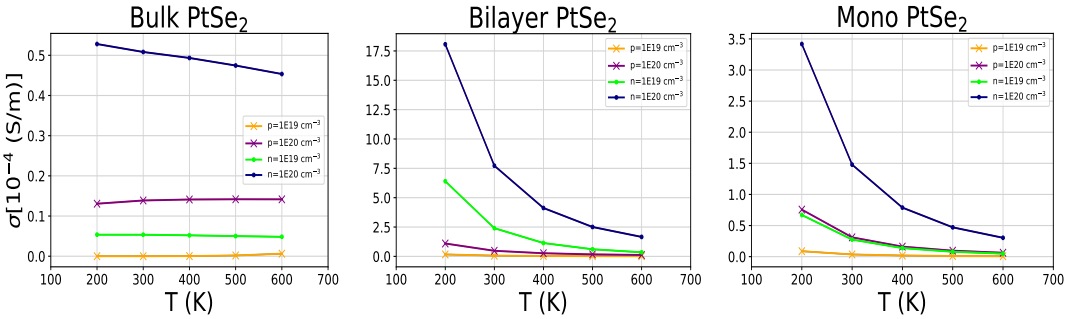


Figure 4.43: Electrical conductivity for a single layer in bulk, bilayer and monolayer $PtSe_2$.

contributions dominate the total thermal conductivity since $\kappa_L \geqslant \kappa_e$.

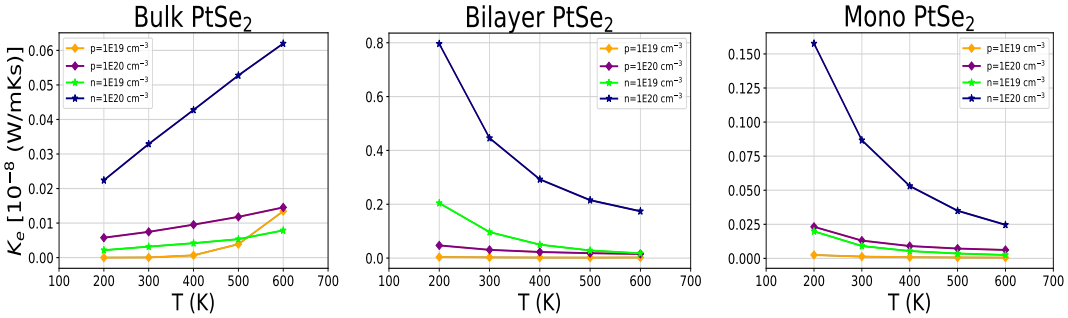


Figure 4.44: Electronic contribution to thermal conductivity for a single layer in bulk, bilayer and monolayer $PtSe_2$.

The power factor was calculated over a temperature range of temperature, from 200 K to 600 K for a single layer bulk, bilayer and monolayer $PtSe_2$, the obtained results plotted in Figure 4.45. The similarity between the bulk and the bilayer and a monolayer is visible in the plot. The highest and lowest values of power factor for the bulk structure is detected at 600 K which 06 obtained by the electrons carriers concentration of 10^{20}cm^{-3}, and for bilayer and monolayer are at 200 K which detected by the electrons carriers concentration of 10^{20}cm^{-3}, respectively, close to 200 K. The charge carriers concentration decreases gradually when the temperature increase, which is reverse to the lowest charge carriers concentration.

The dimensionless figure of merit (ZT) was determined within 500K and 600 K for $PtSe_2$. The figure of merit magnitudes of 0.16 at 500 K for bulk, and 0.35 at 600 K for bilayer, and 0.46 at 300 K for monolayer were extracted, as illustrated in Figure 4.46. The high values of the figure of merit were achieved by holes carriers in bulk case, and

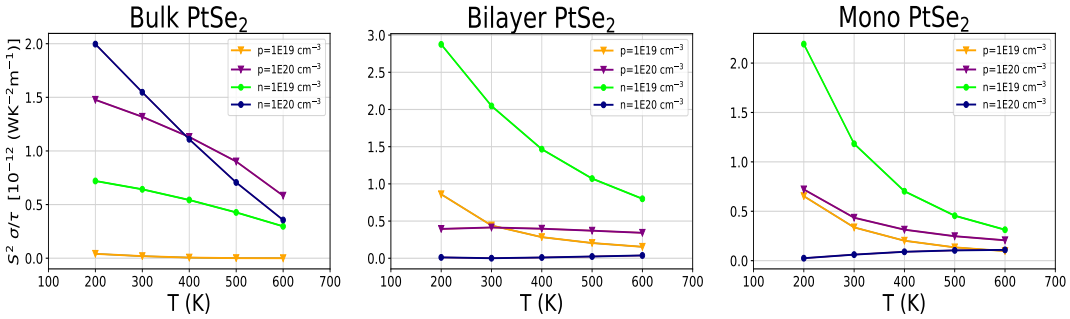


Figure 4.45: Power factor for a single layer in bulk, bilayer and monolayer $PtSe_2$.

by electrons carriers in bilayer and monolayer cases. The monolayer structure possess a higher value than bulk and bilayer.

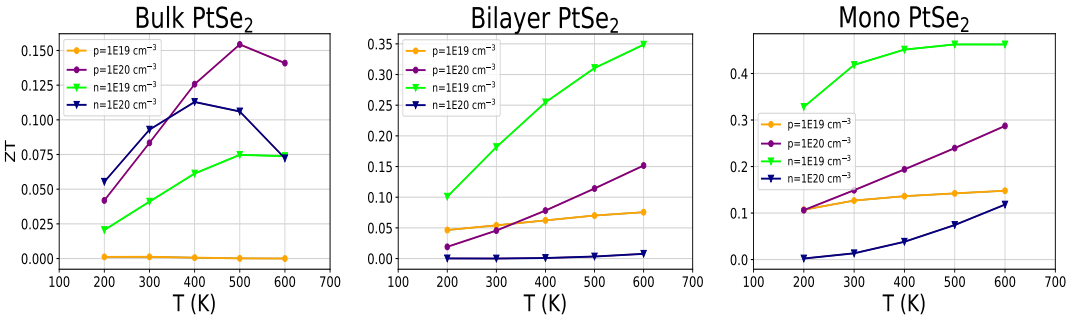


Figure 4.46: Figure of merit for bulk, bilayer and monolayer $PtSe_2$.

4.4 Platinum ditelluride ($PtTe_2$)

4.4.1 Structural Properties

The fully optimized equilibrium lattice constants of $PtTe_2$ for two approximations compared with experimental data are listed in Table 4.13. We observe that the calculated results by optB86-vdW are $a_0 = 4.05$ Å, $c_0 = 5.11$ Å and $V_0 = 72.04$ Å^3, which are agree with the experimental $a_0 = 4.01$ Å, $c_0 = 5.20$ Å and $V_0 = 72.43$ Å^3 [145]. Also the calculated lattice parameters for a bilayer are same to the results by previous study. On the other hand, we set $c = 15\mathring{A}$ as a vacuum layer for bilayer and monolayer which is make the vad der Waal's force between the layers to be weak. The investigation of the phase stabilities for bulk, bilayer and monolayer, were done using the cohesive and formation energies as defined in Chapter 3, using Equation (3.2.1) and (3.2.2) respectively. Our calculated cohesive and formation energies are listed in Table 4.13 per atom for bulk, bilayer and monolayer, and compared with the available previous study. Formation and cohesive energies are negative, indicating these structures are energetically stable. the $PtTe_2$ structures are exothermic, suggesting that structures can be formed from their constituent atoms [146]. The a and c lattice parameters, the in-layer structural parameters, show the least variation across the different approximations. The inter-layer spacing, defined by the c lattice parameter, show the most variation. We note that optB86-vdW gives the best equilibrium structural parameters for $PtTe_2$ when compared to experiment.

Table 4.13: Calculated, experimental and theoretical optimized lattice constants of bulk bilayer and monolayer $PtTe_2$, cohesive (E_{coh}) and formation formation energies per atom, and inter-layer distance.

		a (Å)	c (Å)	V_o (Å^3)	E_{coh} (eV)	E_{form} (eV)
Bulk	PBE	4.00	4.89	66.9	-4.43	-0.40
	optB86b-vdW	4.05	5.11	72.04	-3.24	-0.37
	Exp[45, 38, 39]	4.02	5.22	73.29	–	–
	Exp.[145]	4.01	5.20	72.43	–	–
Bilayer	PBE	4.08	15	–	-3.80	-0.37
	optB86b-vdW	4.09	15	–	-2.93	-0.84
Monolayer	PBE	4.05	15	–	-3.80	-0.36
	optB86-vdW	4.04	15	–	-2.74	-0.66
	Previous work[123]	4.02	–	–	–	-0.32

4.4.2 Mechanical stability

The calculations mechanical properties are exam for the elastic stability of materials. The obtained elastic constants are listed in Table 4.14, accordance with the Born stability criteria [102] see section (3.3.1), which confirm that the bulk, bilayer and a monolayer $PtTe_2$ are mechanically stable. Further, we investigated Young's moduli (Y) and Poisson's ratio (ν) to test the stiffness and bonding nature of the materials. In Table 4.15, we present the computed Young's moduli (Y) and Poisson's ratio (ν) for bulk, bilayer and monolayer $PtTe_2$ compared to an available previous study [41], and bulk moduli and shear moduli for bulk $PtTe_2$. As we mentioned previously of Young's moduli decreasing with when the number of layer decrease, indicative of increased resistance to deformation under the application of opposing forces as the number of layers is increased. While, the Poisson's ratio values looks the same for all bulk, bilayer and monolayer. The values of the Young's moduli in Table 4.7 shows that the bulk is more resist to deformation than monolayer and bilayer, also the bilayer more resist than monolayer.

Table 4.14: Elastic constants (C_{ij} (GPa)), for bulk, bilayer and monolayer $PtTe_2$.

		C_{11}	C_{12}	C_{13}	C_{33}	C_{66}
Bulk	optB86b-vdW	169.33	52.83	42.16	69.22	58.25
Bilayer	PBE	85.36	21.74	–	–	–
Monolayer	PBE	64.61	22.89	–	–	–
Monolayer	Other work[41]	58.62	32.90	–	–	–

Table 4.15: The obtained Bulk moduli (B) Shear moduli (G),Young's moduli (Y) and Poisson's ratio (ν) in GPa, for bulk, bilayer and monolayer, and the other theoretical study.

		B	Y	G	ν
Bulk	optB86b-vdW	68.69	103.84	41.60	0.25
Bilayer	PBE	–	79.82	–	0.25
Monolayer	PBE	–	59.64	–	0.29
Monolayer	Other work[41]	–	40.15	–	0.35

4.4.3 Dynamical stability

The phonon dispersion relations were calculated along with the high symmetry directions. Figure 4.47(a-c) depicted the phonon band structure, for bulk, bilayer and

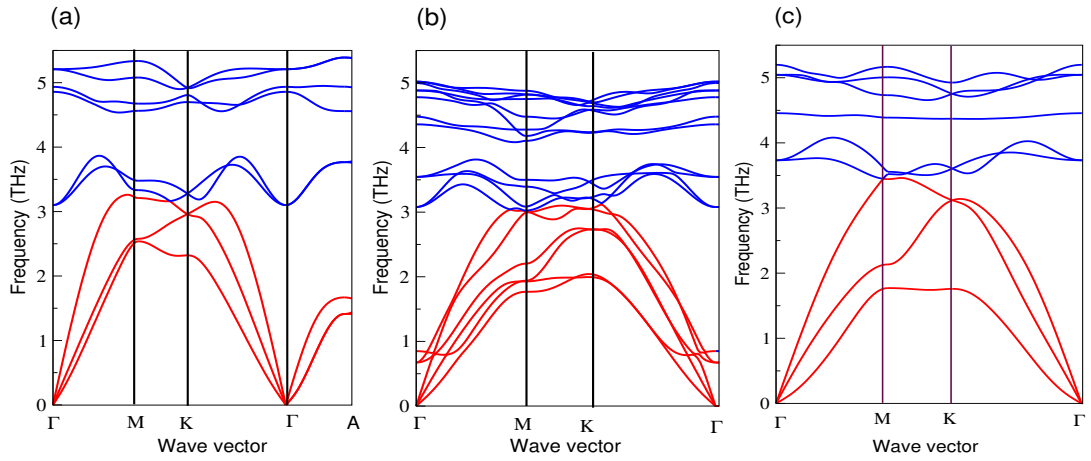


Figure 4.47: The band structure of phonon dispersion for $PtTe_2$. (a) Bulk (b) Bilayer (c) Monolayer.

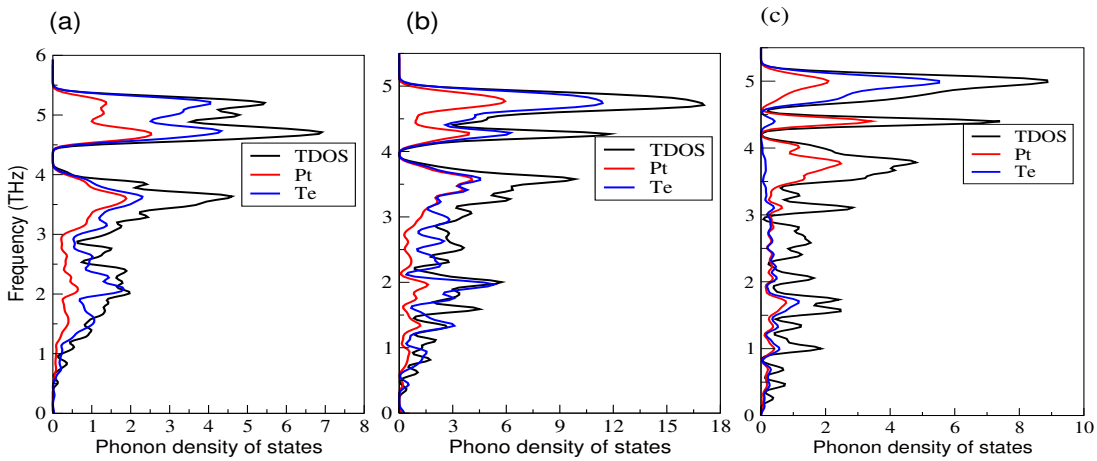


Figure 4.48: TDOS and atomic contributions to acoustic and optical modes of phonon dispersion for $PtTe_2$. (a) Bulk (b) Bilayer (c) Monolayer.

monolayer $PtTe_2$. The phonon frequencies range is $0-5.4$ THz, $0-5.0$ THz and $0-5.2$ THz for bulk, bilayer and monolayer, respectively. Figure 4.48(a-c) show the total and partial density of states, and explain the atomic contribution to the total phonon density, to the acoustic and optical mode for bulk, bilayer and monolayer. All the phonon frequencies are positive, which is suggest that the bulk, bilayer and monolayer of $PtTe_2$ are dynamically stable. Also, we observed the same phonon band structure dense of the bilayer $PtTe_2$ as in bilayer for PtO_2, PtS_2 and $PtSe_2$. From the plots, we can confirm that the most contribution of (Pt) atoms are in acoustic mode and (Te) atoms are in optical mode.

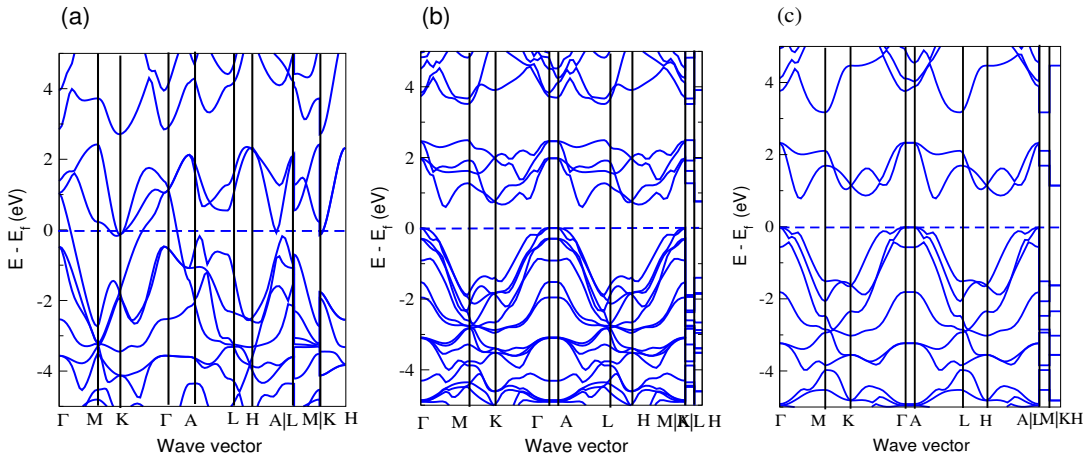


Figure 4.49: Calculated band structure of $PtTe_2$. (a) Bulk (b) Bilayer (c) Monolayer.

4.4.4 Electronic structure properties

In Figure 4.49(a-c) and Figure 4.50(a-c), we show the electronic band structure, total and partial density of states of the bulk, bilayer and monolayer $PtTe_2$, respectively. The electronic structure investigations proved that the bulk phase of both compounds have a semi-metal behavior, hence the bilayer and monolayer are semiconducting with an indirect band gap in both compounds. The minima of the conduction are located at Γ, while the maxima of the valance band between A and L points, almost the same of PtO_2, of the Brillouin zone. The obtained density of states (total and partial) was done to know the orbital contributions to the gap edge. We found that a semi-metal behaviour for bulk through the density of states plot, but the bilayer and monolayer are semiconductors with gap edge determine by Te(p) in top of the valence band and hybridization of Pt(d) and Te(p) in the minimum conduction band. The bilayer band structure exhibits the same behavior of a bilayer for other compounds. In Table 4.16, we listed the band gap values for bulk, bilayer and monolayer for $PtTe_2$. Our calculated results agreed with some of the previous studies [26, 50, 48]. We find that the band gaps decrease with the increasing number of layers as it was previously reported by Xu M *et al.* [140]. The obtained results of band gap for bilayer and monolayer were consistent to photovoltaic solar cell applications.

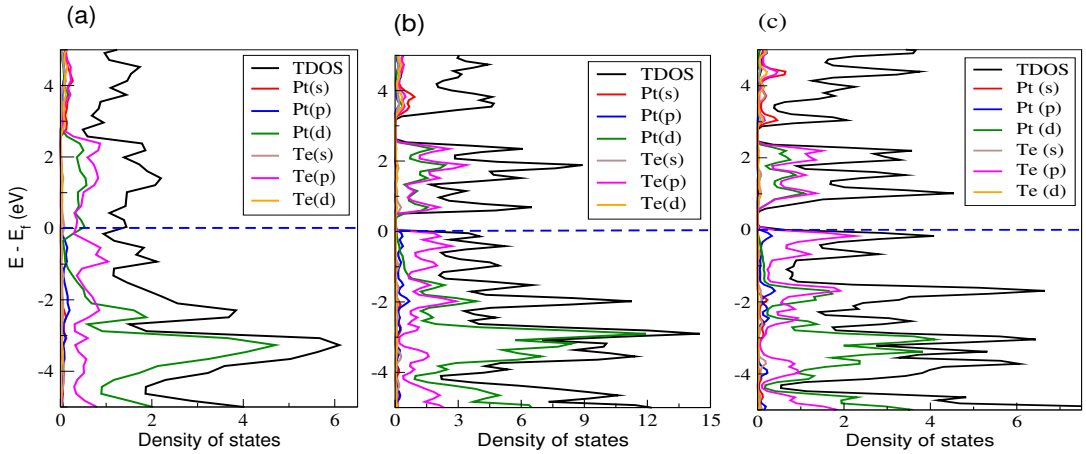


Figure 4.50: Calculated total and partial DOS of $PtTe_2$. (a) Bulk (b) Bilayer (c) Monolayer.

Table 4.16: The calculated band gaps values compared to the experimental and theoretical (in eV) of $PtTe_2$.

	optB86-vdW	PBE	GW_0	Exp.	Other calculations
Bulk	semimetal	semimetal	–	semimetal[29]	–
Bilayer	0.33	0.43	—	—	—
Monolayer	0.63	0.80	3.90, 2.03[123]	—	0.75[123],0.61[42],0.38[52], 0.70[135],0.79[130]

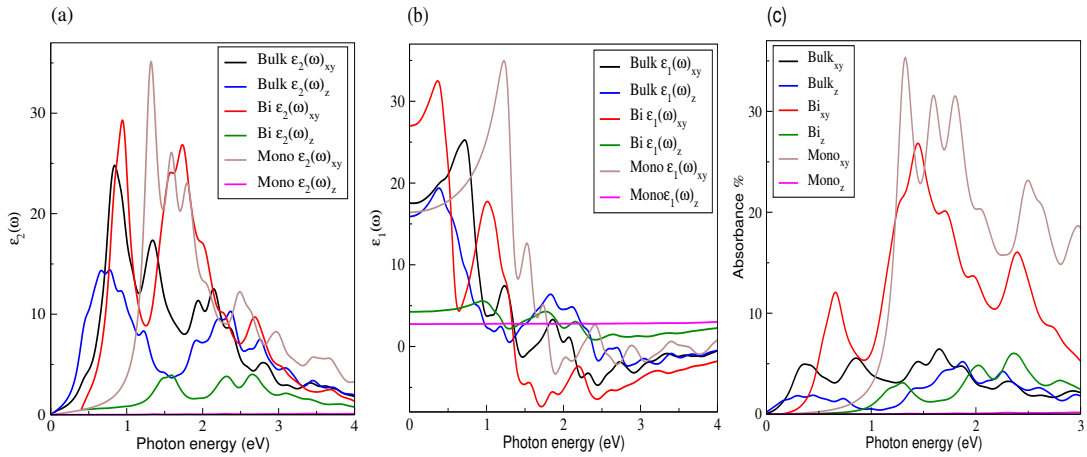


Figure 4.51: GW_0 BSE results (a) imaginary part $\varepsilon_2(\omega)$, (b) real part $\varepsilon_1(\omega)$ of dielectric function and (c) absorbance for bulk, bilayer and monolayer of $PtTe_2$.

4.4.5 Optical properties

The imaginary and real parts of the dielectric functions, and the absorbance of bulk, a single layer of the bilayer and a monolayer $PtTe_2$, were calculated and plotted in Figure 4.51(a-c). The maximum absorbance in in-plane polarization for monolayer is ≈ 35.27% at 1.33 eV and for bilayer is ≈ 26.75% at 1.45 eV and 6.32% at 1.65 eV for bulk. The absorbance of a monolayer is considerably greater than the absorbance for a bilayer and bulk. This agrees with MoS_2, $MoSe_2$ and WS_2 results (5−10%) [115, 116], where the single layer absorbance is high in monolayer than bilayer and bulk. Moreover, the out-of-plane polarisation, the maximum absorbance is ≈ 0.15% at 2.30 eV for monolayer and ≈ 6.04% at 2.36 eV for bilayer and 5.20% at 1.88 eV for bulk. The Tauc plot [117], was used to obtain the optical band gap. For the bulk $PtTe_2$, the in-plane and out-of-plane optical band gap polarizations are 0.03 and 0.00 eV, respectively, which is confirmed the experimental measurements. The calculated optical band gaps of the in-plane and out-of-plane polarization, for the monolayer, are 1.00 and 1.50 eV, and for bilayer are 0.37 and 0.92 eV, respectively. Therefore, the obtained values of the monolayer and bilayer can be use for photovoltaic solar cells applications [142, 143, 144].

4.4.6 Lattice thermal conductivity

In Figure 4.52(a) and (b), we illustrate the lattice thermal conductivity vs temperature and frequency, respectively, for a single layer of bulk, bilayer and monolayer $PtTe_2$ structure. The average lattice thermal conductivity at 300 K for single layer in bulk, bilayer and monolayer is 0.33×10^{-8}, 0.12×10^{-8} and 0.07×10^{-8} $Wm^{-1}K^{-1}$ in-plane direction for a single layer in bulk, bilayer and monolayer respectively, and 0.08×10^{-8} $Wm^{-1}K^{-1}$ out-of-plane for bulk while the out-of-plane for bilayer and monolayer are zero. The lattice thermal conductivity value for bulk decreases by about ∼64% of the bilayer and ∼79% of the monolayer, in the in-plane. Further, the high in-plane value of lattice thermal conductivity per single layer was found to be in the low-temperature range is 2.58×10^{-8} $Wm^{-1}K^{-1}$ at 20 K for bulk, and 0.95×10^{-8} $Wm^{-1}K^{-1}$ at 20 K for bilayer and 0.52×10^{-8} $Wm^{-1}K^{-1}$ at 30 K for monolayer. The high out-of-plane is 0.60×10^{-8} $Wm^{-1}K^{-1}$ at 20 K for single layer bulk. The lattice thermal conductivity against frequency at 300 K is presented in Figure 4.52(b), and its cumulative lattice thermal conductivity as a function of the frequency of single layer for bulk, bilayer and monolayer. We observed that the lattice thermal conductivity is highly anisotropic,

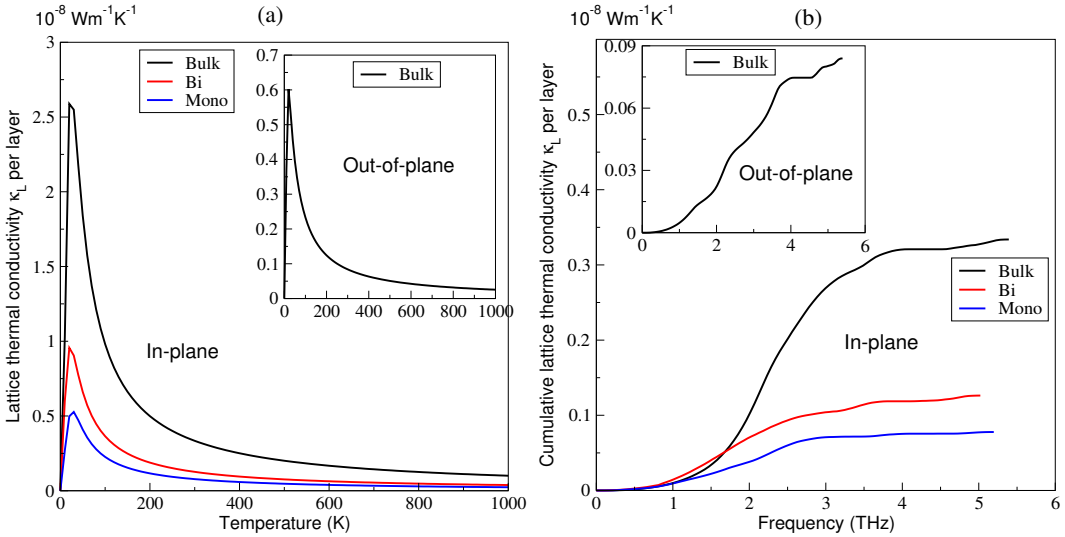


Figure 4.52: Lattice thermal conductivity per layer for $PtTe_2$, (a) lattice thermal conductivity against temperature, (b) cumulative lattice thermal conductivity against frequency.

with the thermal conductivity in-plane of the layers being much higher than in the out-of-plane direction for two cases bulk, bilayer and monolayer. The all lattice thermal conductivity values for a single layer in bulk, bilayer and monolayer $PtTe_2$, are suits for thermoelectric application

Furthermore, we computed the directional projected density of states for each atom as a function of frequency. The in-plane and out-of-plane contributions are shown in Figure 4.53 left and right, respectively, which are along [100] and [001]. The results appears the similarity of directional projected density of states for other compounds. To perceive the contribution ratio of phonon to lattice thermal conductivity for bulk, bilayer and monolayer $PtTe_2$, we compute the contribution of acoustic and optical phonons modes. The contribution estimated to the thermal conductivity from the acoustic modes at 300 K. We obtained that the in-plane acoustic mode total contribution is 86.22%, 83.33% and 92.30% for bulk, bilayer and monolayer $PtTe_2$ respectively. While the out-of-plane 64.29% for bulk, and 0% for bilayer and monolayer. The contributions of phonon to lattice thermal conductivity per atoms are illustrated in Figure 4.54 (left and right), for bulk, bilayer and monolayer. Through Figure 4.54, we can note that the ratio of contribution is almost the same in in-plane, for bulk, bilayer and monolayer. Also in the right, we have out-of-plane, which is for bulk. This is in clear contrast to the conventional understanding, especially in the out-of-plane direction, that the acoustic

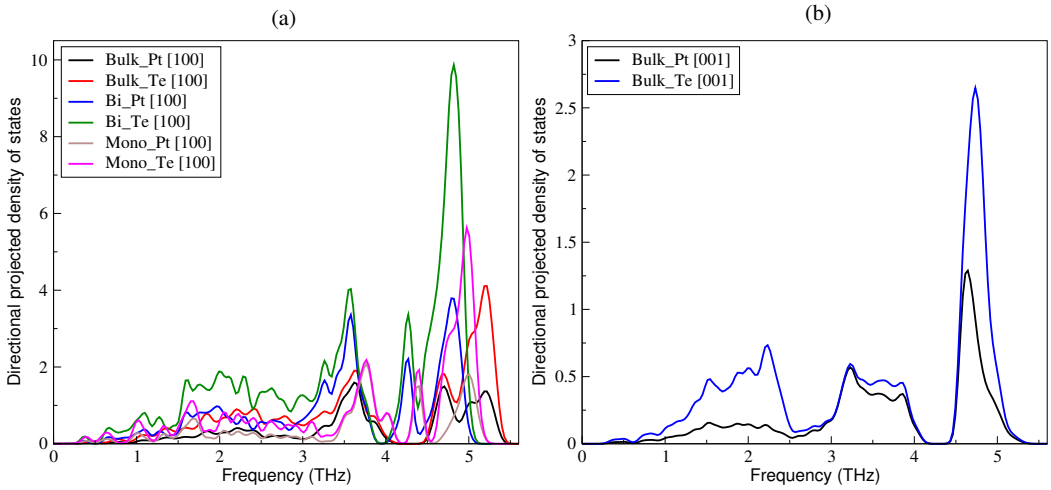


Figure 4.53: Directional projected density of states, left is in-plane and right is out-of-plane for bulk, bilayer and monolayer $PtTe_2$ as function of frequency.

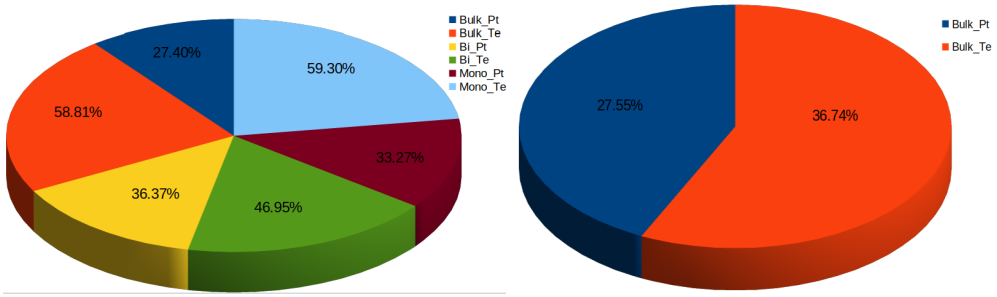


Figure 4.54: Contribution ratio of phonon to lattice thermal conductivity, left is in-plane and right is out-of-plane for bulk and monolayer $PtTe_2$ as function of frequency. (Recall there is no contribution in out-of-plane for monolayer).

modes control thermal conductivity [127].

Phonon lifetime

The third-order force constants [90, 95], were used to obtain the phonon lifetime. The phonon lifetime at 300 K for bulk, bilayer and monolayer $PtTe_2$, as a function of frequency, as depicted in Figure 4.55(a-c). The highest peak for phonon lifetime is located in acoustic mode, and while the lowest peak for phonon lifetime is located in optical mode for all structures. This is in accordance with a slightly strong scattering in the high frequency optical phonon modes. The phonon lifetime distribution of acoustic and optical phonon mode can be used to differentiate the phonon lifetime contributions to the total lattice thermal conductivity [128].

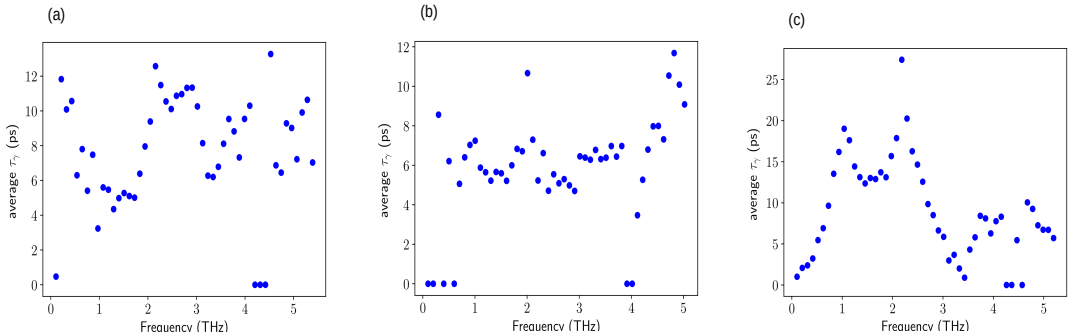


Figure 4.55: Phonon lifetime against frequency at 300 K for $PtTe_2$. (a) Bulk, (b) bilayer and (c) monolayer.

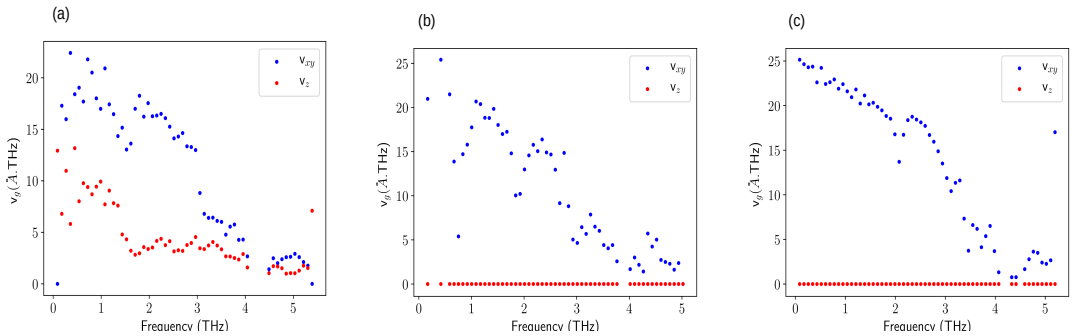


Figure 4.56: Average directional phonon group velocities against frequency for $PtTe_2$. (a) Bulk, (b) bilayer and (c) monolayer.

Group velocity

The investigations of group velocity was described according to Equation (2.5.10). In Figure 4.56(a-c) we plot the average of group velocity. The in-plane group velocity is higher than out-of-plane in the low frequency range, while at high frequency the in-plane and out-of-plane are small compared to the low frequency values. The anisotropy in group velocity has a big impact on the lattice thermal conductivity [129]. The similarity of the distribution for in-plane group velocities of bulk and monolayer. In contrast, the out-of-plane group velocities is 13 Å.THz for bulk, while it is 0 Å.THz for bilayer and monolayer. The combined effect of the frequency dependence of the phonon lifetimes and group velocities are consistent with the anisotropy in the thermal conductivity as well as the large contribution to the total thermal conductivity form the low frequency phonons.

4.4.7 Transport properties of $PtTe_2$

Figure 4.57 shows the calculated Seebeck coefficients for a single layer in bulk, bilayer and monolayer $PtTe_2$, between 200 K and 800 K temperature range. The Seebeck coefficient for the bulk have negative values for all charge carriers concentration, which explain that the bulk can be a good n-type material. Possibly because the bulk have metallic behaviour so the majority of carriers should be electrons. From the plot, we can observe that the Seebeck coefficients are increases according to increase of the temperature.

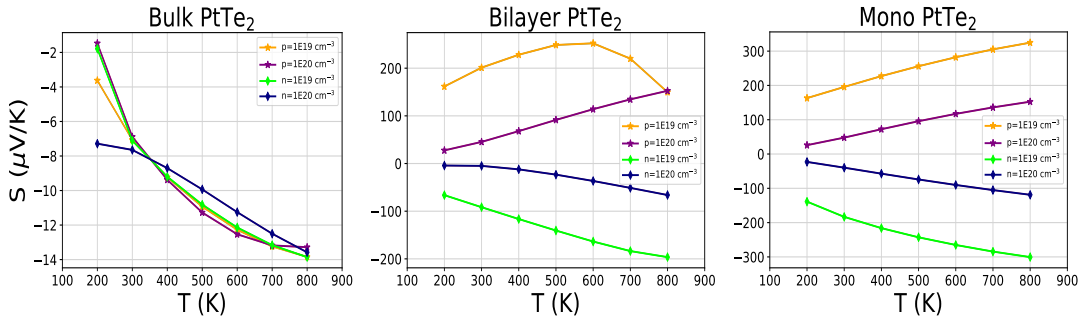


Figure 4.57: Seebeck coefficients of bulk, bilayer and monolayer $PtTe_2$.

Figure 4.58, presents the electrical conductivity for a single layer in bulk, bilayer and monolayer $PtTe_2$ in the temperature range of 200 K to 800 K. The highest values were found to be at 200 K for all structures, which are 7.9×10^{-4} S/m for bulk, 4.4×10^{-4} S/m for bilayer and 1.5×10^{-4} S/m for monolayer, which are associated with by electron carriers whose concentration is 10^{20} cm^{-3} for a single layer in bulk, bilayer and monolayer. For all concentration of carriers, the electrical conductivity decreases with an increase in temperature. This indicates that an increase in temperature results in a decrease in electrical conductivity, due to their inverse relationship, and it is converse to what was noted in Figure 4.57 for the case of Seebeck coefficient. This is also observed in the preceding binary compounds.

The obtained electronic contribution to thermal conductivity for a single layer in bulk, bilayer and monolayer $PtTe_2$ in the temperature range of 200 K to 800 K is provided in Figure 4.58. To understand how the total thermal conductivity is affected by electronic contribution. Figure 4.59 shows the maximum values, at a low temperature of 200 K for bulk, bilayer and monolayer, while, the lowest values are found to be at high temperature range. Also, the behavior of bilayer and monolayer kook the same, since

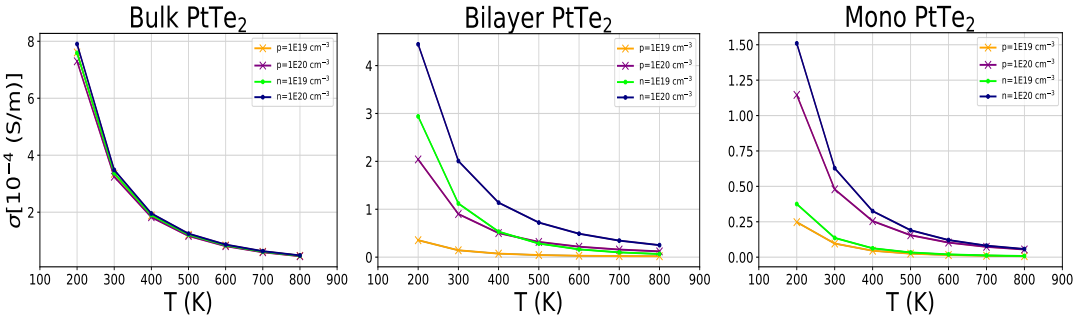


Figure 4.58: Electrical conductivity for a single layer in bulk, bilayer and monolayer $PtTe_2$.

the high concentration for each of electrons and holes has a high value of the electronic contribution, reverse to the low concentration. However, the highest values are determined when the majority are electrons whose carrier concentrations is 10^{20}cm^{-3}. The obtained results show the lowest electronic contribution is provided by the monolayer structure, whereas the highest is by bulk structure.

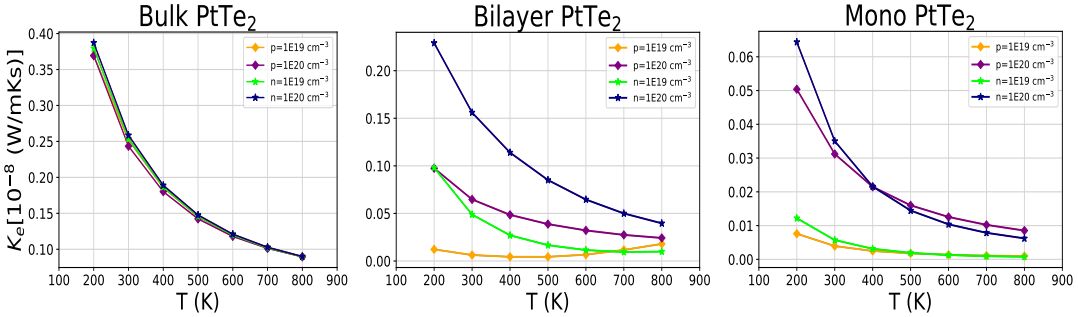


Figure 4.59: Electronic contribution to thermal conductivity for a single layer in bulk, bilayer and monolayer $PtTe_2$.

The calculated power factor for a single layer in bulk, bilayer, and monolayer $PtTe_2$ in the temperature range of 200 K to 800 K, were plotted in Figure 4.60. The highest and lowest values of power factor was found at low temperature of 200 K. The behavior of power factor curvature for bilayer and monolayer looks the same since the charge carriers concentration of 10^{19}cm^{-3} for each of electrons and holes have given high values at low temperature, while the low values were reported for charge carrier concentration of 10^{20}cm^{-3} for each of them. Contrarily, the behavior of the bulk system seemed different.

The dimensionless figure of merit (ZT) was calculated from 200 K to 800 K, and the greatest values for a single layer in the bulk, bilayer and monolayer $PtTe_2$ are attained

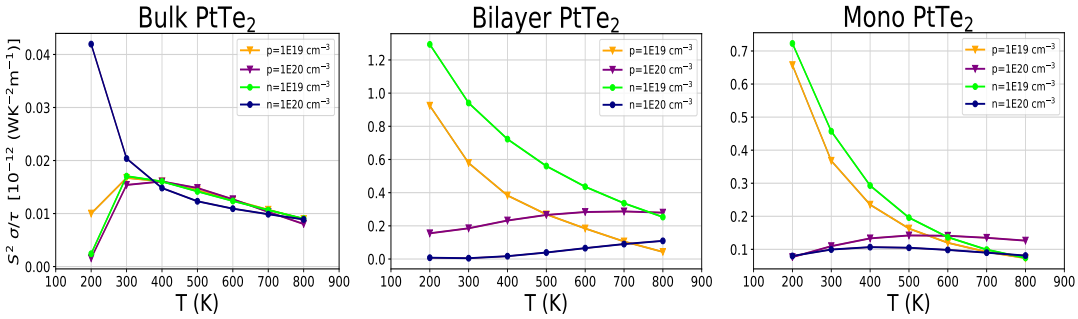


Figure 4.60: Power factor for a single layer in bulk, bilayer and monolayer $PtTe_2$.

at 800 K. The obtained ZT values are, 0.08 at 600 K for bulk, 0.37 at 700 K for bilayer and 0.51 at 600 K for monolayer, as depicted in Figure 4.61. The high values of ZT were dominated by holes carrier of 10^{20}cm^{-3} for bulk and by electrons carriers of 10^{19}cm^{-3} for bilayer and monolayer. The results indicates that a monolayer have higher ZT than bilayer and bulk. Also, the figure of merit values for all the structures increases with increasing temperature, since, the lowest values are at low temperature.

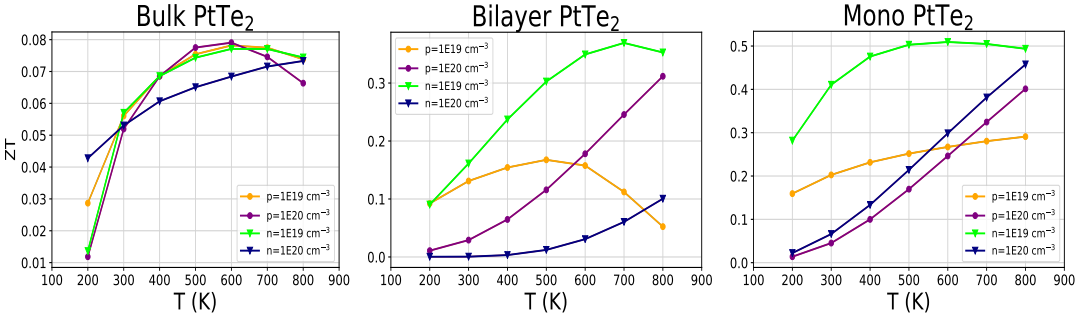


Figure 4.61: Figure of merit for bulk, bilayer and monolayer $PtTe_2$.

5

Summary and Conclusion

5.1 Summary

In this section we summarize the results of our calculations for the PtX_2 (α-PtO_2, PtS_2, $PtSe_2$ and $PtTe_2$) compounds examined in this thesis. All compounds were structurally relaxed to configurations that are mechanically and dynamically stable. Table 5.1, presents the calculated DFT and BSE-optical (in-plane and out-of-plane) band gap values for the PtX_2 compounds. We note that α-PtO_2 has the widest band gap (DFT and optical) compared to other compounds. Also, the band gap values increases from bulk to bilayer to monolayer, which suggests that a degree of band gap engineering is possible for these compounds. The obtained optical band gap values in the 0.3 - 2.75 eV range for PtX_2 structures, so the values between 1.0 to 1.7 eV are suitable for photovoltaics cell applications, while the values less than 1.0 and high than 1.7 are suitable for lower and top layers of the tandem solar cell, respectively [142, 143, 144].

Table 5.1: Our calculated, DFT and BSE-optical gap (in-plane (in) and out-of-plane (out)) band gaps (in eV) for the bulk, bilayer and monolayer of PtX_2.

Compound	Bulk				Bilayer				Monolayer			
	optB	PBE	BSE		optB	PBE	BSE		optB	PBE	BSE	
			in	out			in	out			in	out
α-PtO_2	1.61	1.63	1.66	1.77	1.63	1.74	1.89	2.34	1.72	1.86	2.32	2.75
PtS_2	0.81	1.06	1.09	1.36	1.13	1.26	1.61	1.73	1.67	1.80	1.95	2.30
$PtSe_2$	semimetal	semimetal	0.10	0.3	0.93	0.93	1.10	1.25	1.38	1.38	1.43	1.64
$PtTe_2$	semimetal	semimetal	0.03	0.00	0.33	0.43	0.37	0.92	0.63	0.80	1.00	1.50

In Table 5.2, we listed the results for the maximum absorbance in the range from $1-3$ eV. The PtX_2 structures exhibited values ranging from 0.9 for bulk α-PtO_2 up to 35 for monolayer $PtTe_2$. Hence, the monolayers absorbance has the highest values among the others, also it increases from α-PtO_2 to $PtTe_2$ compound. Moreover, the absorbance is dependent on the thickness of the material, which is the reason for the high values for monolayer, since it is thickness is a single layer thick. The monolayer $PtTe_2$ show the highest absorbance compared to others.

Table 5.2: The calculated maximum absorbance of in-plane, in the visible photon energy range for bulk, and a single layer of bilayer and monolayer PtX_2.

Compound	Bulk		Bilayer		Monolayer	
	absorbance %	Energy (eV)	absorbance %	Energy (eV)	absorbance %	Energy (eV)
α-PtO_2	0.91	2.12	5.64	2.51	8.06	2.92
PtS_2	2.00	2.90	7.64	1.83	13.15	2.51
$PtSe_2$	25.04	1.95	26.89	1.51	31.05	2.06
$PtTe_2$	6.32	1.65	26.75	1.45	35.27	1.33

The in-plane average lattice thermal conductivity per layer for PtX_2 compounds are shown in Table 5.3. Hence, our calculated values of the in-plane average lattice thermal conductivity for PtX_2 compounds per layer are in range from 0.07×10^{-8} for monolayer $PtTe_2$ to 8.47×10^{-8} $Wm^{-1}K^{-1}$ for bulk α-PtO_2 at room temperature. The results are given per layer for ease of comparison, see Section (3.6) for details. The low values of the lattice thermal conductivity is considered to be promising for the thermoelectric figures of merit. In our results, the lowest lattice thermal were found for the monolayers, $PtTe_2$ monolayer has lowest value of all the compounds investigated.

Table 5.3: Lattice thermal conductivity (in $Wm^{-1}K^{-1}$) for a single PtX_2 layer.

Compound	$\kappa_L \times 10^{-8}$ (Bulk)	$\kappa_L \times 10^{-8}$ (Bilayer)	$\kappa_L \times 10^{-8}$ (Monolayer)
α-PtO_2	8.47	4.59	1.06
PtS_2	2.30	1.16	0.15
$PtSe_2$	0.47	0.24	0.11
$PtTe_2$	0.33	0.12	0.07

Thermoelectric figures of merit (ZT) for the PtX_2 compounds are shown in Table 5.4. For comparison, we stated the highest values of ZT at a certain temperature, besides that, we observed how the ZT appears in various temperature. Our obtained ZT is between 0.04 at 200 K for bulk PtS_2 to 0.74 at 300 K for monolayer α-PtO_2, which it looks small ZT values for the bulk system. It is clear, that the monolayer for each compound possesses a high ZT value. Besides that, also the highest monolayer ZT

value at 300 K, was found to be that of monolayer α-PtO_2, which is close to unity. Even though the thermal conductivity has a low value, unfortunately, the power factor was small for all PtX_2 compounds. Since the ZT of monolayer α-PtO_2 has a value that is close to unity. Hence, it can be suitable for thermoelectric applications as n-type since it is due to the electrons charge carrier, as compared to the bulk system. The ZT of others system are low, for thermoelectric applications as it is unless strategies to improve ZT via reduction of lattice component i.e through straining or nanostructuring are implemented.

Table 5.4: The in-plane highest figure of merit (ZT) at a various temperature regimes of bulk, bilayer and monolayer PtX_2.

Compound	Bulk		Bilayer		Monolayer	
	ZT	Temperature (K)	ZT	Temperature (K)	ZT	Temperature(K)
α-PtO_2	0.11	700	0.62	400	0.74	300
PtS_2	0.04	200	0.12	500	0.18	500
$PtSe_2$	0.16	500	0.35	600	0.46	500
$PtTe_2$	0.08	600	0.37	700	0.51	600

5.2 Conclusion

First-principles calculations were used to investigate the structural, mechanical, dynamical stabilities, optical and thermoelectric properties of the trigonal PtX_2 (X=O, S, Se and Te), to get some insights about their applications as a thermoelectric or photovoltaic materials. This was carried out using density functional theory and many-body perturbation theory. All calculations were performed using the Vienna *ab-initio* Simulation Package (VASP) in conjunction with the PHONOPY, PHONO3PY and BoltzTraP2 packages. Mostly, the results are in agreement with available experimental and theoretical data. Since these PtX_2 compounds have potential device applications, we opted to summarise our results and discuss potential applications separately as provided below. We hope that our predicted results will provide a better theoretical understanding of the rich properties of these materials, as extensively captured in this work.

The study of structural properties shows that the compounds, at their minimum energy configurations, are mechanically and dynamically stable. While, through the DFT and optical band gap, the monolayer of PtX_2 compounds show that the values of band gap are good for photovoltaic and tandem solar cell application [142, 143, 144]. However,

the absorbance results depict that the monolayer $PtTe_2$ possesses a high percentage of radiation absorption. Furthermore, we investigated the in-plane average lattice thermal conductivity for PtX_2 compounds per layer, in order to calculate the transport coefficients, which was encourage by the low values average lattice thermal conductivity. Unfortunately, the calculation of the in-plane transport show low values for the power factor for all PtX_2 structures. That was the main reason for the low values of the obtained thermoelectric figure of merit ZT.

References

[1] Hamza AH Mohammed, GM Dongho-Nguimdo, and Daniel P Joubert. Structural stability, electronic, optical and lattice thermal conductivity properties of bulk and monolayer PtS_2. *Materials Today Communications*, 21:100661, 2019.

[2] Terry Tritt. *Recent trends in thermoelectric materials research, part two*. Academic Press, 2000.

[3] Mercouri G Kanatzidis. Nanostructured thermoelectrics: the new paradigm? *Chemistry of materials*, 22(3):648–659, 2010.

[4] Mildred S Dresselhaus, Gang Chen, Ming Y Tang, RG Yang, Hohyun Lee, DZ Wang, ZF Ren, J-P Fleurial, and Pawan Gogna. New directions for low-dimensional thermoelectric materials. *Advanced materials*, 19(8):1043–1053, 2007.

[5] Jian He and Terry M Tritt. Thermal-to-electrical energy conversion from the nanotechnology perspective. *Nanotechnology for the Energy Challenge*, pages 47–77, 2010.

[6] Yucheng Lan, Austin Jerome Minnich, Gang Chen, and Zhifeng Ren. Enhancement of thermoelectric figure-of-merit by a bulk nanostructuring approach. *Advanced Functional Materials*, 20(3):357–376, 2010.

[7] Terry M Tritt, Harald Böttner, and Lidong Chen. Thermoelectrics: Direct solar thermal energy conversion. *MRS bulletin*, 33(4):366–368, 2008.

[8] Jihui Yang and Thierry Caillat. Thermoelectric materials for space and automotive power generation. *MRS bulletin*, 31(3):224–229, 2006.

[9] AW Allen. Thermoelectrically cooled ir detectors beat the heat: Annual detector handbooook. *Laser focus world*, 33(3):S15–S19, 1997.

[10] Paul Hersch and Kenneth Zweibel. Basic photovoltaic principles and methods. Technical report, Solar Energy Research Inst., Golden, CO (USA), 1982.

[11] Edmond Becquerel. On electric effects under the influence of solar radiation. *Compt. rend.*, 9:561, 1839.

[12] Adolf Goetzberger, Joachim Knobloch, and Bernhard Voss. *Crystalline silicon solar cells*. Wiley Online Library, 1998.

[13] Martin A Green. *Silicon solar cells: advanced principles & practice*. Centre for photovoltaic devices and systems, University of New South Wales, 1995.

[14] Adolf Goetzberger and Volker Uwe Hoffmann. *Photovoltaic solar energy generation*, volume 112. Springer Science & Business Media, 2005.

[15] Huijun Kong. *Thermoelectric Property Studies on Lead Chalcogenides, Double-filled Cobalt Tri-Antimonide and Rare Earth-Ruthenium-Germanium*. PhD thesis, 2008.

[16] HoSung Lee. Thermoelectric generators. *homepages. wmich. edu leehs/ ME539/ Thermoelectric % 20Contact% 20Resistances. pdf.[Accessed 15 february 2017]*, 2014.

[17] Daniel D Pollock. *Thermoelectricity: theory, thermometry, tool*. Number 852. ASTM International, 1985.

[18] Edmund Altenkirch. Elektrothermische kälteerzeugung und reversible elektrische heizung. *Physikalische Zeitschrift*, 12:920–924, 1911.

[19] TC Harman, PJ Taylor, MP Walsh, and BE LaForge. Quantum dot superlattice thermoelectric materials and devices. *science*, 297(5590):2229–2232, 2002.

[20] J Heremans and CM Thrush. Thermoelectric power of bismuth nanowires. *Physical Review B*, 59(19):12579, 1999.

[21] William B Jensen. A note on the term" chalcogen". *J. Chem. Educ.*, 74(9):1063, 1997.

[22] Wolfram Koch, Max C Holthausen, and M Kaupp. Bucher-a chemist's guide to density functional theory. *Angewandte Chemie-German Edition*, 113(5):989–989, 2001.

[23] Mohammad Nazmul Hasan, Md Nafiujjaman, and Yong-Kyu Lee. 2d nanomaterials for gene delivery. In *Biomedical Applications of Graphene and 2D Nanomaterials*, pages 87–104. Elsevier, 2019.

[24] Sajedeh Manzeli, Dmitry Ovchinnikov, Diego Pasquier, Oleg V Yazyev, and Andras Kis. 2d transition metal dichalcogenides. *Nature Reviews Materials*, 2(8):17033, 2017.

[25] Xinyi Chia, Ambrosi Adriano, Petr Lazar, Zdeněk Sofer, Jan Luxa, and Martin Pumera. Layered platinum dichalcogenides PtS_2, $PtSe_2$, and $PtTe_2$ electrocatalysis: monotonic dependence on the chalcogen size. *Advanced Functional Materials*, 26(24):4306–4318, 2016.

[26] GY Guo and WY Liang. The electronic structures of platinum dichalcogenides: PtS_2, $PtSe_2$ and $PtTe_2$. *Journal of Physics C: Solid State Physics*, 19(7):995, 1986.

[27] S Furuseth. Selte k and kjeckshus a 1965. *Acta. Chem. Scand*, 19:259.

[28] Manish Chhowalla, Hyeon Suk Shin, Goki Eda, Lain-Jong Li, Kian Ping Loh, and Hua Zhang. The chemistry of two-dimensional layered transition metal dichalcogenide nanosheets. *Nature chemistry*, 5(4):263, 2013.

[29] D Dai, H-J Koo, M-H Whangbo, C Soulard, X Rocquefelte, and S Jobic. Trends in the structure and bonding in the layered platinum dioxide and dichalcogenides $PtQ_2(Q = O, S, Se \text{ and } Te)$. *Journal of Solid State Chemistry*, 173(1):114–121, 2003.

[30] S Soled, A Wold, and O Gorochov. Crystal growth and characterization of several platinum sulfoselenides. *Materials Research Bulletin*, 11(8):927–932, 1976.

[31] C Ellinger, A Stierle, IK Robinson, A Nefedov, and H Dosch. Atmospheric pressure oxidation of pt (111). *Journal of Physics: Condensed Matter*, 20(18):184013, 2008.

[32] Marcel David Ackermann et al. *Operando SXRD: a new view on catalysis*. Leiden Institute of Physics, Faculty of Science, Leiden University, 2007.

[33] Olaf Muller and Rustum Roy. Formation and stability of the platinum and rhodium oxides at high oxygen pressures and the structures of pt_3o_4, β-pto_2 and rho_2. *Journal of the Less Common Metals*, 16(2):129–146, 1968.

[34] Carolyn Rubin Aita. Optical behavior of sputter-deposited platinum-oxide films. *Journal of applied physics*, 58(8):3169–3173, 1985.

[35] H Neff, S Henkel, E Hartmannsgruber, E Steinbeiss, W Michalke, K Steenbeck, and HG Schmidt. Structural, optical, and electronic properties of magnetron-sputtered platinum oxide films. *Journal of applied physics*, 79(10):7672–7675, 1996.

[36] Jin Zhensheng, Xi Chanjuan, Zeng Qingmei, Yin Feng, Zhao Jiazheng, and Xue Jinzhen. Catalytic behavior of nanoparticle α-pto_2 for ethanol oxidation. *Journal of Molecular Catalysis A: Chemical*, 191(1):61–66, 2003.

[37] JJ Blackstock, DR Stewart, and Z Li. Plasma-produced ultra-thin platinum-oxide films for nanoelectronics: physical characterization. *Applied Physics A*, 80(6):1343–1353, 2005.

[38] ARNE KJEKSHUS and FREDRIK GRQNVOLD. High temperature x-ray study of the thermal expansion. *Acta Chemica Scandinavica*, 13(9):1767–1774, 1959.

[39] G Kliche. Far-infrared and x-ray investigations of the mixed platinum dichalcogenides $PtS_{2-x}Se_x, PtSe_{2-x}Te_x,$ and$PtS_{2-x}Te_x$. *Journal of Solid State Chemistry*, 56(1):26–31, 1985.

[40] Sohail Ahmad. Strained noble metal di chalcogenides $PtX_2(X = S, Se)$ monolayer: Ab initio study of electronic and lattice dynamic properties. *Physica E: Low-dimensional Systems and Nanostructures*, 95:139–143, 2018.

[41] Juan Du, Peng Song, Lizhen Fang, Tianxing Wang, Zhongming Wei, Jingbo Li, and Congxin Xia. Elastic, electronic and optical properties of the two-dimensional ptx_2 (x= s, se, and te) monolayer. *Applied Surface Science*, 435:476–482, 2018.

[42] Zhishuo Huang, Wenxu Zhang, and Wanli Zhang. Computational search for two-dimensional mx_2 semiconductors with possible high electron mobility at room temperature. *Materials*, 9(9):716, 2016.

[43] C Mankai, G Martinez, and O Gorochov. Optical properties at the absorption edge of $Pt_{0.97}S_2$. *Physical Review B*, 16(10):4666, 1977.

[44] F Parsapour, DF Kelley, and RS Williams. Spectroscopy of eu^{3+}-doped pts_2 nanoclusters. *The Journal of Physical Chemistry B*, 102(41):7971–7977, 1998.

[45] S Furuseth, K Selte, and A Kjekshus. Redetermined crystal structures of nite2 pdte2 pts2 ptse2 and ptte2, 1965.

[46] Kenan Zhang, Mingzhe Yan, Haoxiong Zhang, Huaqing Huang, Masashi Arita, Zhe Sun, Wenhui Duan, Yang Wu, and Shuyun Zhou. Experimental evidence for type-ii dirac semimetal in $ptse_2$. *Physical Review B*, 96(12):125102, 2017.

[47] Yeliang Wang, Linfei Li, Wei Yao, Shiru Song, JT Sun, Jinbo Pan, Xiao Ren, Chen Li, Eiji Okunishi, Yu-Qi Wang, et al. Monolayer $ptse_2$, a new semiconducting transition-metal-dichalcogenide, epitaxially grown by direct selenization of pt. *Nano letters*, 15(6):4013–4018, 2015.

[48] Maria OBrien, Niall McEvoy, Carlo Motta, Jian-Yao Zheng, Nina C Berner, Jani Kotakoski, Kenan Elibol, Timothy J Pennycook, Jannik C Meyer, Chanyoung Yim, et al. Raman characterization of platinum diselenide thin films. *2D Materials*, 3(2):021004, 2016.

[49] Chanyoung Yim, Kangho Lee, Niall McEvoy, Maria OBrien, Sarah Riazimehr, Nina C Berner, Conor P Cullen, Jani Kotakoski, Jannik C Meyer, Max C Lemme, et al. High-performance hybrid electronic devices from layered $ptse_2$ films grown at low temperature. *ACS nano*, 10(10):9550–9558, 2016.

[50] Pengfei Li, Lei Li, and Xiao Cheng Zeng. Tuning the electronic properties of monolayer and bilayer $ptse_2$ via strain engineering. *Journal of Materials Chemistry C*, 4(15):3106–3112, 2016.

[51] San-Dong Guo. Biaxial strain tuned thermoelectric properties in monolayer $ptse_2$. *Journal of Materials Chemistry C*, 4(39):9366–9374, 2016.

[52] San-Dong Guo and Yan Wang. Small compressive strain-induced semiconductor–metal transition and tensile strain-enhanced thermoelectric properties in monolayer $ptte_2$. *Semiconductor Science and Technology*, 32(5):055004, 2017.

[53] Mingzhe Yan, Huaqing Huang, Kenan Zhang, Eryin Wang, Wei Yao, Ke Deng, Guoliang Wan, Hongyun Zhang, Masashi Arita, Haitao Yang, et al. Lorentz-violating type-ii dirac fermions in transition metal dichalcogenide $ptte_2$. *Nature communications*, 8(1):257, 2017.

[54] San-Dong Guo. Spin-orbit and strain effect on power factor in monolayer mos_2. *Computational Materials Science*, 123:8–13, 2016.

[55] San-Dong Guo and Jian-Li Wang. Spin–orbital coupling effect on the power factor in semiconducting transition-metal dichalcogenide monolayers. *Semiconductor Science and Technology*, 31(9):095011, 2016.

[56] Max Born and Kun Huang. *Dynamical theory of crystal lattices*. Clarendon press, 1954.

[57] P Hohenberg and W Kohn. Physical review 136. *B864*, 1964.

[58] Walter Kohn and Lu Jeu Sham. Self-consistent equations including exchange and correlation effects. *Physical review*, 140(4A):A1133, 1965.

[59] David J Griffiths. *Introduction to quantum mechanics*. Pearson international edition (Pearson Prentice Hall, 2005), 2010.

[60] Richard M Martin and Richard Milton Martin. *Electronic structure: basic theory and practical methods*. Cambridge university press, 2004.

[61] Jorge Kohanoff. *Electronic structure calculations for solids and molecules: theory and computational methods*. Cambridge University Press, 2006.

[62] Wolfram Koch and Max C Holthausen. *A chemist's guide to density functional theory*. John Wiley & Sons, 2015.

[63] James D Patterson. Density-functional theory of atoms and molecules: Robert g. parr and weitao yang. oxford university press, new york, and clarendon press, oxford (1989). us 55. 333 pages, 1989.

[64] Mohammed SH Suleiman and Daniel P Joubert. Quantum mechanical ab initio calculations of the structural, electronic and optical properties of bulk gold nitrides. *The European Physical Journal B*, 88(11):305, 2015.

[65] Dongho Nguimdo and Guy Moise. *Computational study of chalcogenide based solar energy materials*. PhD thesis, 2016.

[66] Axel D Becke. Density-functional thermochemistry. v. systematic optimization of exchange-correlation functionals. *The Journal of chemical physics*, 107(20):8554–8560, 1997.

[67] Frank Herman, John P Van Dyke, and Irene B Ortenburger. Improved statistical exchange approximation for inhomogeneous many-electron systems. *Physical Review Letters*, 22(16):807, 1969.

[68] Mahmud Abdulsalam. *A theoretical investigation of the structural, electronic and optical properties of transition metal chalcogenides*. PhD thesis, 2015.

[69] John P Perdew, Kieron Burke, and Matthias Ernzerhof. Generalized gradient approximation made simple. *Physical review letters*, 77(18):3865, 1996.

[70] Jiří Klimeš, David R Bowler, and Angelos Michaelides. Chemical accuracy for the van der waals density functional. *Journal of Physics: Condensed Matter*, 22(2):022201, 2009.

[71] NW Ashcroft and ND Mermin. Solid state physics (brooks cole, 1976). *Cited on*, 45, 1993.

[72] Charles Kittel et al. *Introduction to solid state physics*, volume 8. Wiley New York, 1976.

[73] Mike C Payne, Michael P Teter, Douglas C Allan, TA Arias, and ad JD Joannopoulos. Iterative minimization techniques for ab initio total-energy calculations: molecular dynamics and conjugate gradients. *Reviews of modern physics*, 64(4):1045, 1992.

[74] Hendrik J Monkhorst and James D Pack. Special points for brillouin-zone integrations. *Physical review B*, 13(12):5188, 1976.

[75] DJ Chadi and Marvin L Cohen. Special points in the brillouin zone. *Physical Review B*, 8(12):5747, 1973.

[76] Fernando Nogueira, Alberto Castro, and Miguel AL Marques. A tutorial on density functional theory. In *A Primer in Density Functional Theory*, pages 218–256. Springer, 2003.

[77] James C Phillips and Leonard Kleinman. New method for calculating wave functions in crystals and molecules. *Physical Review*, 116(2):287, 1959.

[78] David Vanderbilt. Soft self-consistent pseudopotentials in a generalized eigenvalue formalism. *Physical review B*, 41(11):7892, 1990.

[79] Peter E Blöchl. Projector augmented-wave method. *Physical review B*, 50(24):17953, 1994.

[80] Norman Troullier and José Luís Martins. Efficient pseudopotentials for plane-wave calculations. *Physical review B*, 43(3):1993, 1991.

[81] Carlos Fiolhais, Fernando Nogueira, and Miguel AL Marques. *A primer in density functional theory*, volume 620. Springer Science & Business Media, 2003.

[82] Wilfried G Aulbur, Lars Jönsson, and John W Wilkins. Quasiparticle calculations in solids. *Solid State Physics*, 54:1–218, 2000.

[83] AL Fetter. Jd walecka quantum theory of many-particles systems, 1971.

[84] Lars Hedin. New method for calculating the one-particle green's function with application to the electron-gas problem. *Physical Review*, 139(3A):A796, 1965.

[85] Giovanni Onida, Lucia Reining, and Angel Rubio. Electronic excitations: density-functional versus many-body greens-function approaches. *Reviews of modern physics*, 74(2):601, 2002.

[86] Lucia Reining. 10 linear response and more: the bethe-salpeter equation. *Quantum Materials: Experiments and Theory*.

[87] MJ Van Setten, R Gremaud, G Brocks, B Dam, G Kresse, and GA De Wijs. Optical response of the sodium alanate system: Gw_0-bse calculations and thin film measurements. *Physical Review B*, 83(3):035422, 2011.

[88] Amelia Carolina Sparavigna. The boltzmann equation of phonon thermal transport solved in the relaxation time approximation–i–theory. 2016.

[89] Keiyu Mizokami, Atsushi Togo, and Isao Tanaka. Lattice thermal conductivities of two sio_2 polymorphs by first-principles calculations and the phonon boltzmann transport equation. *Physical Review B*, 97(22):224306, 2018.

[90] DT Morelli, JP Heremans, and GA Slack. Estimation of the isotope effect on the lattice thermal conductivity of group iv and group iii-v semiconductors. *Physical Review B*, 66(19):195304, 2002.

[91] Isaak Mikhailovich TSIDIL'KOVSKY and A TYBULEWICZ. . *Thermomagnetic Effects in Semiconductors. Translated by A. Tybulewicz, Etc.* Infosearch, 1962.

[92] George S Nolas, Jeffrey Sharp, and Julian Goldsmid. *Thermoelectrics: basic principles and new materials developments*, volume 45. Springer Science & Business Media, 2013.

[93] Neil W Ashcroft. Nd mermin solid state physics. *Saunders College, Philadelphia*, 120, 1976.

[94] Donald T Morelli and Glen A Slack. High lattice thermal conductivity solids. In *High Thermal Conductivity Materials*, pages 37–68. Springer, 2006.

[95] Atsushi Togo and Isao Tanaka. First principles phonon calculations in materials science. *Scripta Materialia*, 108:1–5, 2015.

[96] Georg Kresse and D Joubert. From ultrasoft pseudopotentials to the projector augmented-wave method. *Physical Review B*, 59(3):1758, 1999.

[97] Georg Kresse and Jürgen Furthmüller. Efficient iterative schemes for ab initio total-energy calculations using a plane-wave basis set. *Physical review B*, 54(16):11169, 1996.

[98] Georg Kresse and J Hafner. Ab initio molecular dynamics for open-shell transition metals. *Physical Review B*, 48(17):13115, 1993.

[99] Jiří Klimeš, David R Bowler, and Angelos Michaelides. Van der waals density functionals applied to solids. *Physical Review B*, 83(19):195131, 2011.

[100] Francis Birch. Finite elastic strain of cubic crystals. *Physical review*, 71(11):809, 1947.

[101] Paul Heyliger, Hassel Ledbetter, and Sudook Kim. Elastic constants of natural quartz. *The Journal of the Acoustical Society of America*, 114(2):644–650, 2003.

[102] Félix Mouhat and François-Xavier Coudert. Necessary and sufficient elastic stability conditions in various crystal systems. *Physical review B*, 90(22):224104, 2014.

[103] A Bouhemadou, R Khenata, M Kharoubi, T Seddik, Ali H Reshak, and Y Al-Douri. Fp-apw+ lo calculations of the elastic properties in zinc-blende iii-p compounds under pressure effects. *Computational Materials Science*, 45(2):474–479, 2009.

[104] Richard Hill. The elastic behaviour of a crystalline aggregate. *Proceedings of the Physical Society. Section A*, 65(5):349, 1952.

[105] Qing Peng and Suvranu De. Outstanding mechanical properties of monolayer mos_2 and its application in elastic energy storage. *Physical Chemistry Chemical Physics*, 15(44):19427–19437, 2013.

[106] Kai Liu, Qimin Yan, Michelle Chen, Wen Fan, Yinghui Sun, Joonki Suh, Deyi Fu, Sangwook Lee, Jian Zhou, Sefaattin Tongay, et al. Elastic properties of chemical-vapor-deposited monolayer mos_2, ws_2, and their bilayer heterostructures. *Nano letters*, 14(9):5097–5103, 2014.

[107] Kamal Choudhary, Gowoon Cheon, Evan Reed, and Francesca Tavazza. Elastic properties of bulk and low-dimensional materials using van der waals density functional. *Physical Review B*, 98(1):014107, 2018.

[108] Mehmet Topsakal, Seymur Cahangirov, and Salim Ciraci. The response of mechanical and electronic properties of graphane to the elastic strain. *Applied Physics Letters*, 96(9):091912, 2010.

[109] Atsushi Togo, Laurent Chaput, and Isao Tanaka. Distributions of phonon lifetimes in brillouin zones. *Physical Review B*, 91(9):094306, 2015.

[110] Prasanta Misra. *Physics of condensed matter*. Academic Press, 2011.

[111] K. Schwarz. International tables for crystallography. *Physical Properties of Crystals*, D:294–313, 2006.

[112] David Sholl and Janice A Steckel. *Density functional theory: a practical introduction*. John Wiley & Sons, 2011.

[113] M Gajdoš, K Hummer, G Kresse, J Furthmüller, and F Bechstedt. Linear optical properties in the projector-augmented wave methodology. *Physical Review B*, 73(4):045112, 2006.

[114] Nurettin Korozlu, K Colakoglu, and E Deligoz. Structural, electronic, elastic and optical properties of $cd_xzn_{1-x}te$ mixed crystals. *Journal of Physics: Condensed Matter*, 21(17):175406, 2009.

[115] Li Yang, Jack Deslippe, Cheol-Hwan Park, Marvin L Cohen, and Steven G Louie. Excitonic effects on the optical response of graphene and bilayer graphene. *Physical review letters*, 103(18):186802, 2009.

[116] Marco Bernardi, Maurizia Palummo, and Jeffrey C Grossman. Extraordinary sunlight absorption and one nanometer thick photovoltaics using two-dimensional monolayer materials. *Nano letters*, 13(8):3664–3670, 2013.

[117] O Stenzel. The physics of thin film optical spectra, surface sciences, 2005.

[118] J Bardeen and W Shockley. Deformation potentials and mobilities in non-polar crystals. *Physical review*, 80(1):72, 1950.

[119] Georg KH Madsen, Jesús Carrete, and Matthieu J Verstraete. Boltztrap2, a program for interpolating band structures and calculating semi-classical transport coefficients. *Computer Physics Communications*, 231:140–145, 2018.

[120] JR McBride, GW Graham, CR Peters, and WH Weber. Growth and characterization of reactively sputtered thin-film platinum oxides. *Journal of applied physics*, 69(3):1596–1604, 1991.

[121] HR Hoekstra, S Siegel, and GALLAGHE. FX. Reactions of platinum dioxide with some metal oxides. In *ABSTRACTS OF PAPERS OF THE AMERICAN CHEMICAL SOCIETY*, number SEP, page IN5. AMER CHEMICAL SOC 1155 16TH ST, NW, WASHINGTON, DC 20036, 1969.

[122] E. E. Galloni R. H. Busch, A. Cairo and J. Raskovan. Preparacion y estructura cristallina del pto_2. *Rev. Un. Mat. Argentina.*, 15:16–17, 1951.

[123] Filip A Rasmussen and Kristian S Thygesen. Computational 2d materials database: electronic structure of transition-metal dichalcogenides and oxides. *The Journal of Physical Chemistry C*, 119(23):13169–13183, 2015.

[124] Qu Yue, Jun Kang, Zhengzheng Shao, Xueao Zhang, Shengli Chang, Guang Wang, Shiqiao Qin, and Jingbo Li. Mechanical and electronic properties of monolayer mos_2 under elastic strain. *Physics Letters A*, 376(12-13):1166–1170, 2012.

[125] Atsushi Togo. Phonopy v. 1.8. 5. *Avaliable: http://phonopy. sourceforge. net*, 2009.

[126] Adolf Goetzberger, Joachim Luther, and Gerhard Willeke. Solar cells: past, present, future. *Solar energy materials and solar cells*, 74(1):1–11, 2002.

[127] Charles Kittel, Paul McEuen, and Paul McEuen. *Introduction to solid state physics*, volume 8. Wiley New York, 1996.

[128] San-Dong Guo and Ai-Xia Zhang. Phonon transport in na2he at high pressure from a first-principles study. *Applied Physics Letters*, 110(17):172104, 2017.

[129] Eric S Toberer, Alex Zevalkink, and G Jeffrey Snyder. Phonon engineering through crystal chemistry. *Journal of Materials Chemistry*, 21(40):15843–15852, 2011.

[130] Houlong L Zhuang and Richard G Hennig. Computational search for single-layer transition-metal dichalcogenide photocatalysts. *The Journal of Physical Chemistry C*, 117(40):20440–20445, 2013.

[131] H Tributsch and O Gorochov. Photoelectrochemical reaction behaviour of platinum disulphide with water and reducing agents. *Electrochimica Acta*, 27(2):215–221, 1982.

[132] F Hulliger. Electrical properties of some nickel-group chalcogenides. *Journal of Physics and Chemistry of Solids*, 26(3):639–645, 1965.

[133] Yuda Zhao, Jingsi Qiao, Peng Yu, Zhixin Hu, Ziyuan Lin, Shu Ping Lau, Zheng Liu, Wei Ji, and Yang Chai. Extraordinarily strong interlayer interaction in 2d layered pts_2. *Advanced Materials*, 28(12):2399–2407, 2016.

[134] Pere Miró, Martha Audiffred, and Thomas Heine. An atlas of two-dimensional materials. *Chemical Society Reviews*, 43(18):6537–6554, 2014.

[135] P Manchanda, Axel Enders, David J Sellmyer, and Ralph Skomski. Hydrogen-induced ferromagnetism in two-dimensional pt dichalcogenides. *Physical Review B*, 94(10):104426, 2016.

[136] Agnieszka Kuc, Nourdine Zibouche, and Thomas Heine. Influence of quantum confinement on the electronic structure of the transition metal sulfide ts_2. *Physical Review B*, 83(24):245213, 2011.

[137] John P Perdew and Adrienn Ruzsinszky. Density-functional energy gaps of solids demystified. *The European Physical Journal B*, 91(6):108, 2018.

[138] O Krogh Andersen. Linear methods in band theory. *Physical Review B*, 12(8):3060, 1975.

[139] Seymour H Vosko, Leslie Wilk, and Marwan Nusair. Accurate spin-dependent electron liquid correlation energies for local spin density calculations: a critical analysis. *Canadian Journal of physics*, 58(8):1200–1211, 1980.

[140] Mingsheng Xu, Tao Liang, Minmin Shi, and Hongzheng Chen. Graphene-like two-dimensional materials. *Chemical reviews*, 113(5):3766–3798, 2013.

[141] Muhammad Zulfiqar, Yinchang Zhao, Geng Li, Safdar Nazir, and Jun Ni. Tunable conductivity and half metallic ferromagnetism in monolayer platinum diselenide: A first-principles study. *The Journal of Physical Chemistry C*, 120(43):25030–25036, 2016.

[142] Tomas Leijtens, Kevin A Bush, Rohit Prasanna, and Michael D McGehee. Opportunities and challenges for tandem solar cells using metal halide perovskite semiconductors. *Nature Energy*, page 1, 2018.

[143] Jess Kaneshiro, Nicolas Gaillard, Richard Rocheleau, and Eric Miller. Advances in copper-chalcopyrite thin films for solar energy conversion. *Solar Energy Materials and Solar Cells*, 94(1):12–16, 2010.

[144] Teodor K Todorov, Douglas M Bishop, and Yun Seog Lee. Materials perspectives for next-generation low-cost tandem solar cells. *Solar Energy Materials and Solar Cells*, 180:350–357, 2018.

[145] L Thomassen. Über kristallstrukturen einiger binärer verbindungen der platinmetalle. *Zeitschrift für Physikalische Chemie*, 2(1):349–379, 1929.

[146] H-J Lamfers, A Meetsma, GA Wiegers, and JL De Boer. The crystal structure of some rhenium and technetium dichalcogenides. *Journal of alloys and compounds*, 241(1-2):34–39, 1996.

[147] Joseph Heremans. Nanometer-scale thermoelectric materials. *Springer Handbook of Nanotechnology, ISBN 978-3-540-29855-7. Springer-Verlag Berlin Heidelberg, 2007, p. 345*, page 345, 2007.

[148] Thomas Johann Seebeck. *Magnetische polarisation der metalle und erze durch temperatur-differenz*. Number 70. W. Engelmann, 1895.

[149] E Altenkirch. Uber den nortzeffkt der thermosaule. *Phys. Z*, 10:560, 1909.

[150] Abraham Fedorovich Ioffe. Semiconductor thermoelements and thermoelectric cooling. 1957.

[151] H Julian Goldsmid. *Electronic refrigeration*. Pion, 1986.

[152] AD Mcnaught and A Wilkinson. Compendium of chemical terminology. *IUPAC: Cambridge*, 1997.

[153] Ralph H Petrucci, William S Harwood, and F Geoffrey Herring. General chemistry. 1993.

[154] Charles E Carraher Jr, William J Scott, Jack A Schroeder, and David J Giron. Poly (cis-dihaiodiamine platinum (ii)) compounds: synthesis and biological activity. *Journal of Macromolecular ScienceChemistry*, 15(4):625–631, 1981.

[155] William B Jensen. The place of zinc, cadmium, and mercury in the periodic table. *Journal of Chemical Education*, 80(8):952, 2003.

[156] Yong Yang, Osamu Sugino, and Takahisa Ohno. Possible magnetic behavior in oxygen-deficient β-pto$_2$. *Physical Review B*, 85(3):035204, 2012.

[157] Alexander V Vorontsov, Evgueni N Savinov, and Jin Zhensheng. Influence of the form of photodeposited platinum on titania upon its photocatalytic activity in co and acetone oxidation. *Journal of Photochemistry and Photobiology A: Chemistry*, 125(1-3):113–117, 1999.

[158] Timo Jacob. Theoretical investigations on the potential-induced formation of pt-oxide surfaces. *Journal of Electroanalytical Chemistry*, 607(1-2):158–166, 2007.

[159] Branimir Radisavljevic, Aleksandra Radenovic, Jacopo Brivio, Valentina Giacometti, and Andras Kis. Single-layer mos$_2$ transistors. *Nature nanotechnology*, 6(3):147, 2011.

[160] RF Service. Beyond graphene. *Science (New York, NY)*, 348(6234):490, 2015.

[161] Haotian Wang, Hongtao Yuan, Seung Sae Hong, Yanbin Li, and Yi Cui. Physical and chemical tuning of two-dimensional transition metal dichalcogenides. *Chemical Society Reviews*, 44(9):2664–2680, 2015.

[162] Branimir Radisavljevic and Andras Kis. Mobility engineering and a metal–insulator transition in monolayer mos$_2$. *Nature materials*, 12(9):815, 2013.

[163] Kin Fai Mak, Changgu Lee, James Hone, Jie Shan, and Tony F Heinz. Atomically thin mos_2: a new direct-gap semiconductor. *Physical review letters*, 105(13):136805, 2010.

[164] Max Born and Robert Oppenheimer. Zur quantentheorie der molekeln. *Annalen der physik*, 389(20):457–484, 1927.

[165] JP Perdew, K Burke, and M Ernzerhof. Perdew, burke, and ernzerhof reply. *Physical Review Letters*, 80(4):891, 1998.

[166] Michael Rohlfing and Steven G Louie. Electron-hole excitations in semiconductors and insulators. *Physical review letters*, 81(11):2312, 1998.

[167] Stefan Albrecht, Lucia Reining, Rodolfo Del Sole, and Giovanni Onida. Ab initio calculation of excitonic effects in the optical spectra of semiconductors. *Physical review letters*, 80(20):4510, 1998.

[168] W Hanke and LJ Sham. Many-particle effects in the optical spectrum of a semiconductor. *Physical Review B*, 21(10):4656, 1980.

[169] Edwin E Salpeter and Hans Albrecht Bethe. A relativistic equation for bound-state problems. *Physical Review*, 84(6):1232, 1951.

[170] LJ Sham and TM Rice. Many-particle derivation of the effective-mass equation for the wannier exciton. *Physical Review*, 144(2):708, 1966.

[171] Orson L Anderson. A simplified method for calculating the debye temperature from elastic constants. *Journal of Physics and Chemistry of Solids*, 24(7):909–917, 1963.

[172] J Tauc, Radu Grigorovici, and Anina Vancu. Optical properties and electronic structure of amorphous germanium. *physica status solidi (b)*, 15(2):627–637, 1966.